THERMOMECHANICAL PROCESSING OF BLENDED ELEMENTAL POWDER Ti-6Al-4V ALLOY

Centre for Materials Engineering

Masters Dissertation

Student: Nicholas Clinning

Supervisor: Prof. R. D. Knutsen

October 2012

Abstract

Titanium and its alloys are extremely attractive structural metals due to their excellent specific strength and corrosion resistance. The high cost of producing titanium and manufacturing products from titanium have however limited it's use to very high-end applications in which their high performance is demanded, principally within the aerospace industry. Of particular industrial importance is the alloy Ti-6Al-4V which accounts for more than 50% of the titanium produced worldwide.

Powder metallurgy (PM) has been identified as a possible route to the manufacturing of cost efficient titanium alloys, which could extend their use to areas such as the automotive industry. The blended elemental (BE) route to producing titanium alloys has been identified as the cheapest process by which the PM process can be utilised. Products produced by the BE approach are however characterised by high impurity levels - in particular the interstitial elements of oxygen and chlorine. This high impurity content results in PM products which typically have a low density and therefore degraded mechanical properties.

This research investigates the feasibility of producing Ti-6Al-4V products by creating low cost BE sintered preforms and then subjecting these preforms to thermomechanical processing (TMP) in an attempt to both improve the relative density and refine the microstructure. The powders used were direct reduction titanium powder and elemental aluminium and vanadium powders. A simple press (375 MPa) and sinter (2hrs at 1200 $^\circ$C) approach was used for the manufacturing of the sintered preforms. The measured relative density of the as-sintered material was 88% and contained pores as large as 100μm.

The microstructural evolution of these preforms was investigated by hot deforming cylindrical specimens by uniaxial deformation at deformation temperatures of 600 $^\circ$C, 700 $^\circ$C, 800 $^\circ$C, 900 $^\circ$C, 1000 $^\circ$C and 1100 $^\circ$C. Deformation was carried out using a Gleeble 3800 TMP simulating system to a strain of 0.69 at a strain rate of $1s^{-1}$ and an annealing treatment of 1hr at 870 $^\circ$C was subsequently imposed upon the deformed specimens. Following the annealing treatment, those specimens deformed at temperatures of 600 $^\circ$C, 700 $^\circ$C, 800 $^\circ$C and 900 $^\circ$C obtained a fully recrystallised equiaxed microstructure. The specimen deformed at 1100 $^\circ$C achieved a fully Widmanstätten lamellar colony microstructure and that deformed at a temperature of 1000 $^\circ$C achieved a bi-modal microstructure consisting of equal parts Widmanstätten and primary α grains. Evaluation of the relative densities of

the deformed specimens revealed that there was no relationship between the deformation temperature and the resultant density.

Specimens deformed at 800 ˚C and 1000 ˚C were subjected to mechanical testing after recrystallisation. Mechanical testing was carried out by three-point-bend tests in accordance with the MPIF standard for the measurement of the transverse rupture strength of PM materials. Mechanical test specimens were obtained from as-sintered specimens that were deformed by plane strain compression (PSC) in the exact same manner as those specimens subjected to uniaxial deformation had been.

Three specimens in each of the conditions: as-sintered, deformed at 800 ˚C and deformed at 1000 ˚C were tested by three-point-bending and density measurements showed each of the six TMP specimens to have a relative density in excess of 98% (compared to the 88% in the as-sintered condition). Despite this significant improvement in density, each of the six TMP specimens suffered brittle rupture at stresses far beneath what all three of the as-sintered material specimens were capable of withstanding. The as-sintered material also fractured in a brittle manner.

It was concluded that the BE material created in this work was inherently brittle due to the high oxygen content characteristic of BE powders. This is thought to be as a result of utilising individual elemental powders of aluminium and vanadium for the blending process, as other researchers using Al-V master alloy powder and very similar press and sinter operations have produced a ductile material. The TMP of this porous, brittle BE material, although capable of markedly improving the density, had detrimental effects on the mechanical properties of the material. This is thought possibly to be as a result of the collapse of large pores during TMP, effectively, introducing the equivalent of cracks into the microstructure which were more detrimental to the mechanical performance of the material than the large pores themselves had been in the as-sintered material.

Acknowledgments

I would like to thanks the following people for their assistance:

- Prof. Knutsen for his much appreciated help and guidance.
- Glen Newins and the mechanical workshop for their ready assistance.
- Dr. Debbie Blaine and Mr. Werner van Zyl from the University of Stellenbosch for their generous help.
- All the staff, students and others involved at the Centre for Materials Engineering (CME) for making it such a pleasant working environment.
- Thank the Department of Science and Technology (DST) in acknowledgment for financial support through the Titanium Centre of Competence as well as the National Research Foundation (NRF).

Declaration

I, Nicholas Clinning, know the meaning of plagiarism and declare that all the work in this document, save for that which is properly acknowledged, is my own.

Signature:_____

Date:_____

Contents

List of Acronyms and Abbreviations

BE - Blended Elemental

TMP - Thermomechanical Processing

PM - Powder Metallurgy

PA - Pre-Alloyed

IM - Ingot Metallurgy

NNS - Near-Net-Shape

CP - Commercially Pure

HCP - Hexagonal Close Packed

BCC - Body Centered Cubic

TTT - Temperature-Time-Transformation

EBSD - Electron Backscatter Diffraction

TEM - Transmission Electron Microscopy

SEM - Scanning Electron Microscope

BSE - Backscattered Electron

CIP - Cold Isostatic Pressing

HIP - Hot Isostatic Pressing

DRC - Dynamic Recovery

DRX - Dynamic Recrystallisation

IHF - Isothermal Hot Forging

LM - Light Microscopy

EDS - Energy Dispersive Spectroscopy

TRB - Transverse Rupture Bar

Chapter 1

Introduction

1.1 Subject of Thesis

The subject of this thesis is to research the possibility of increasing the density and manipulating the microstructure of porous blended elemental (BE) Ti-6Al-4V material by subjecting it to thermomechanical processing (TMP) and thus improving the material's mechanical properties.

1.2 Background to Thesis

Titanium and titanium alloys are very attractive structural metals due to their extremely high strength to weight ratio and corrosion resistance. Of particular industrial importance is the alloy Ti-6Al-4V which accounts for over 50% of the titanium produced worldwide. The high cost of titanium (at least 3 times that of steel for equivalent quantities) has however seen its use restricted to only a few high-end applications primarily within the aerospace industry [1].

The reason for the high cost of titanium alloys is the expensive and energy intensive process of extracting titanium from its mineral form. In addition to this expense of production, titanium is also 10 times as costly to machine compared to aluminium [2].

Powder metallurgy (PM) has been identified as a promising manufacturing technique by which the cost of titanium and titanium alloy products can be reduced. Two distinct types of titanium alloy PM exist based on the powder used: pre-alloyed (PA) PM is conducted using powder that has been created from an ingot of the desired alloy produced by conventional techniques; BE PM makes use of a powder stock which has been created by blending either individual elemental alloying powders or a master alloy powder with elemental titanium powder. The PA approach has been shown to produce components of exceptional quality whose mechanical properties can even surpass those achieved by conventional ingot metallurgy (IM). These powders are however very expensive and the

technique is used mostly for its ease of manufacturing and near-net-shape (NNS) capabilities than as a cheaper alternative to IM, although cost savings can be achieved due to reducing the machining required and the material wastage as a result of NNS production. The BE approach is the cheapest process by which to produce PM titanium alloys, as the titanium powder used can be direct reduction powder as opposed to the PA powder which has gone through the energy intensive (and thus expensive) melting and casting operation. These BE powders are however characterised by high impurity content, specifically oxygen and chlorine, which inhibit very high densities being achieved and thus result in products of inferior mechanical properties [3].

The achievement of cost effective titanium alloys would allow their use to spread out from their limited application in the aerospace industry, and into industries such as the automotive industry, where with increasing fuel prices, low weight vehicles will become a priority.

This research intends to investigate the possibility of creating such a low cost technique for producing Ti-6Al-4V through the thermomechanical processing (TMP) of low cost porous BE preforms in an attempt to increase the density of the material, manipulate the microstructure and improve the mechanical properties.

1.3 Objectives of Thesis

This research aims to achieve the following:

- Create BE material of the alloy Ti-6Al-4V from elemental aluminium and vanadium powders and direct reduction titanium powder.
- Analyse the microstructural evolution of the material when subjected to TMP at various elevated temperatures.
- Measure the changes in density of the BE material as a result of this TMP.
- Evaluate the mechanical properties of the BE material both before and after undergoing TMP in order to measure any improvement in mechanical properties resulting from the TMP.

1.4 Scope and Limitations

No parameters regarding the manufacturing of the BE preforms to be tested as part of this research were altered during the study. The press and sinter operations were kept constant throughout and therefore the influence of these parameters (and therefore the density of the as-sintered material) was not evaluated.

The strain and strain rate of the TMP was also kept constant throughout with only the effect of different deformation temperatures being evaluated in the study of the microstructural evolution resulting from the TMP.

The relative densities calculated and presented in this thesis were calculated as a percentage of the theoretical full density of Ti-6Al-4V (4.43 g/cm^3); however EDS analysis has shown that the BE material created for this research does not perfectly achieve the 6 wt.% aluminum and 4 wt.% vanadium composition of Ti-6Al-4V. Importantly it is seen to be lean in the light element of aluminium. The result of this is that the full density of the material created in this research will be greater than that for Ti-6Al-4V and therefore the relative densities reported in this work are likely to be slightly inflated.

The ideal ratios of specimen thickness to platen width (from 2 to 4) and specimen width to platen width (>6) to ensure plane strain deformation during plane strain compression was not able to be achieved in this research due to the limited size of the sintered preforms that was able to be created.

Due to material size limitations, mechanical testing was not able to be carried out using standard tensile specimens as would be desirable, and was conducted by three-point-bending.

1.5 Plan of Development

This thesis will continue from here with a review of the relevant literature in Chapter 2, after which the experimental methodology observed in the research will be presented in chapter 3. The results and discussion of the uniaxial TMP performed on cylindrical specimens to evaluate the microstructural evolution of the material during hot deformation and subsequent annealing is then presented. In chapter 4 the results of the plane strain compression and mechanical testing of the material is presented and discussed, followed by an evaluation of the fractured three-point-bend specimens by light microscopy. In chapter 7, the conclusions of this research are given, followed by recommendations for future work, a list of references and lastly the appendix.

Chapter 2

Literature Review

2.1 Titanium

2.1.1 Introduction

Despite being discovered well over 100 years previously, it was only in 1910 that titanium was isolated by Matthew Albert Hunter by heating titanium tetrachloride ($TiCl_4$) with sodium. Later, in 1932, Wilhelm Justin Kroll was the first to produce significant quantities of titanium by combining $TiCl_4$ with calcium. The beginning of WWII saw Kroll flee Luxemburg for the United States, and after the war he demonstrated that titanium could be commercially extracted from $TiCl_4$ by changing the reducing agent from calcium to magnesium. This process was dubbed the "Kroll Process" and to this day is the most widely used process for the commercial production of titanium [4].

The DuPont Company, in 1948, was the first to commercially produce titanium and titanium alloys, which were quickly identified as key materials in aircraft engine design [4]. This was because titanium is an attractive structural metal due to its unique combination of low density, corrosion resistance and high specific strength [1]. It is this exceptional specific strength that makes titanium so attractive to the aerospace industry where it is most widely used [5]. Titanium has a density of only 60% of that of steels or nickel-based superalloys [1].

Titanium's corrosion resistance often exceeds that of stainless steels in many environments. Titanium in either pure form or in an alloy has the ability to passivate and thereby exhibits a high degree of immunity against attack by most mineral acids and chlorides. In addition, titanium is non-toxic and is biologically compatible with human tissues and bones. This resistance to corrosion has made titanium and its alloys ideal materials for use in the chemical and petrochemical industries as well as being excellently suited to marine and biomedical engineering applications [1, 6].

As a structural light metal, titanium and its alloys must be compared to the classic light metal, aluminium. At a density of 4.51g/cm^3, pure titanium is twice as dense as alu-

minium, however it has a far greater specific strength than aluminium and as such, a weight saving can still be achieved through a decrease in required volume when replacing aluminium with titanium [2]. Titanium's advantage over aluminium is even greater once temperature is taking into account. 130 ° C is given as the normal maximum operating temperature for conventional aluminium, whereas titanium alloys are used even at temperatures exceeding 500 ° C (figure 2.1) [1, 4].

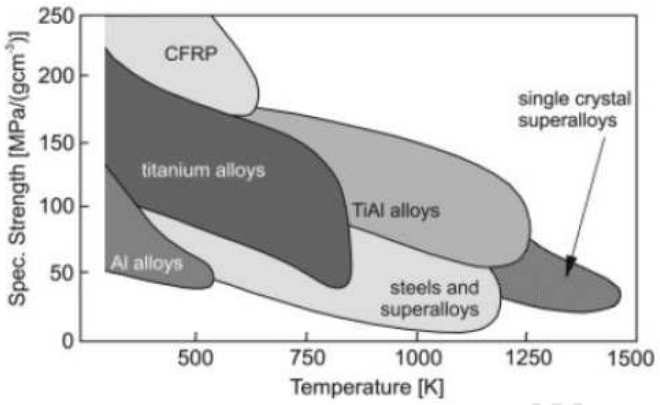

Figure 2.1 – Specific strength of various structural materials as a function of operating temperature [1].

Despite the numerous favourable properties of titanium and its alloys, due to their high cost, the use of titanium materials has been restricted to limited applications, often used only when very high performance is demanded. As such titanium has found little use in non-aerospace fields [7, 8].

As Leyens and Peters [4] explain: it is not because titanium is scarce that it is so expensive - in fact it is the fourth most abundant structural metal in the earth's crust, behind only aluminium, iron and magnesium - but rather the difficulty in processing the metal that inflates its price. These difficulties stem from the fact that, despite its abundance, titanium is seldom found in high concentrations and never in a pure state as well as the high tendency of the metal to react with oxygen and nitrogen at elevated temperatures. The consequence of this reactivity is that still today, in contrast to other structural metals, no continuous process has been developed for the production of titanium and it is only produced by way of a batch process in an inert gas atmosphere [4,5]. As a result, the world production of titanium is very small in comparison to steel, and 80% of that produced is used in the aerospace industry [9].

Not only is titanium, as a raw material, as much as 3 times more expensive than steel or aluminium but it is also far more expensive to machine than other metals (at least 10 times that to machine aluminium) [2].

2.1.2 Alpha and Beta Titanium

Titanium is an allotropic material, and as such can exist in various crystal structures which are stable at different temperatures. Commercially pure (CP) titanium, as well as the majority of titanium alloys exist in a hexagonal close-packed (HCP) crystal structure (α phase) at low temperatures, transforming to a body centred cubic (BCC) structure (β phase) at elevated temperatures. α phase is therefore stable at low temperatures, while the β phase is thermodynamically stable at high temperatures. The temperature at which pure titanium or a titanium alloy no longer has any α phase present and the microstructure has fully transformed to β phase is known as the transus or β-transus temperature. It is quoted as 882 ˚C for CP titanium, but is strongly influenced by both interstitial elements (purity) and alloying elements. The two unit cells for α and β phases can be seen in figure 2.2 with their most densely packed planes and directions shown [4, 5]. The ease of plastic deformation is greater for BCC than for HCP structures, as described by Leyens and Peters [4] and as such, α titanium has limited plastic deformability and ductility compared to β titanium.

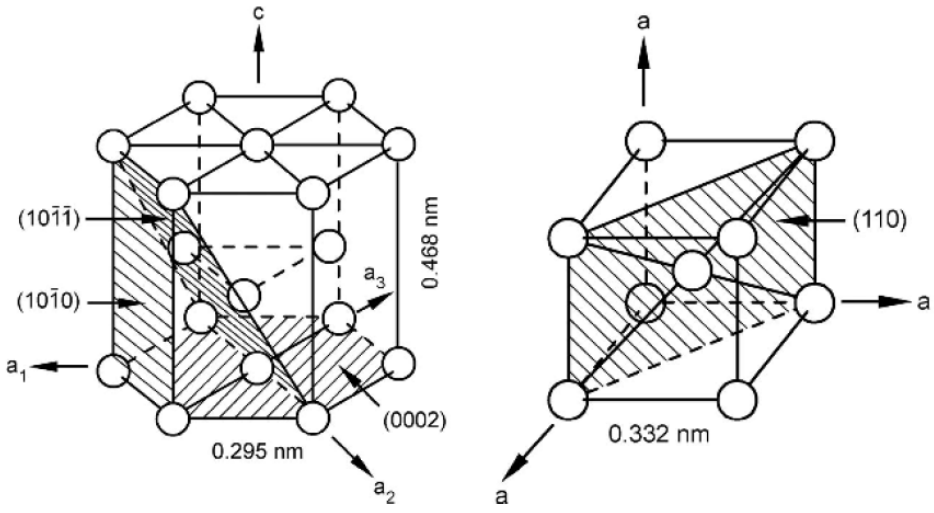

Figure 2.2 – Atomic structure of HCP α (left) and BCC β (right) titanium [1].

2.1.3 Titanium Alloys

Elements to be alloyed with titanium can be categorised as either an α-stabiliser, a β-stabiliser or as neutral. The distinction between an α or β-stabiliser depends on which phase the element is most soluble in. An α-stabiliser will have increased solubility in the α phase as compared to the β phase and as a result has the effect of raising the β-transus temperature, and vice versa for a β-stabiliser. The interstitial elements, O, N and C are strong α-stabilisers as is the alloying element Al. Commonly used β-stabilising alloying elements are: V, Mo, Nb, Ta, Mn, Fe, Cr and Ni. Neutral alloying elements have negligible influence on the transus temperature [5]. These influences are shown graphically in figure

2.3. In addition to their affect on the transus temperature, the development of an α + β region with the addition of either an α or β-stabiliser can be seen.

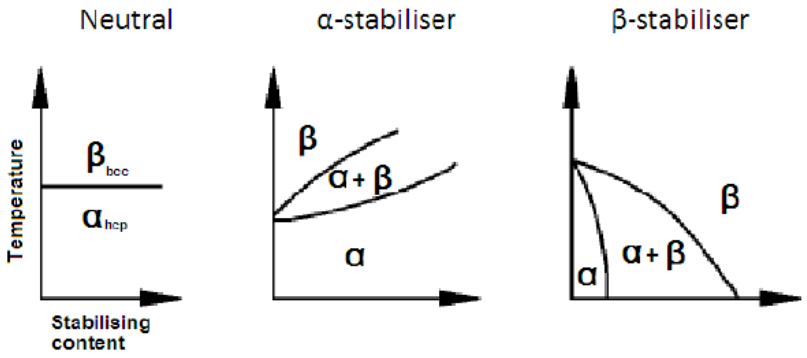

Figure 2.3 – The effect of alloying elements on the phase diagram of titanium. Adapted from [4].

In accordance with their composition, titanium alloys are conventionally classified into one of three different categories: α, α + β and β alloys. α alloys comprise CP titanium (which will have present the impurities O, N and C) and alloys exclusively alloyed with α-stabilisers and/or neutral alloying elements. Most commercial titanium alloys belong to the α + β group. These alloys contain one or more β-stabilising elements (usually V, Mo, Nb or Cr) in addition to the α-stabiliser Al. The β-stabilising content of a titanium alloy can be increased to such a point that the β phase is stable at room temperature, the alloys with these compositions are the β alloys. In addition to the three main alloy classifications explained above, further subdivision into near-α and metastable β alloys is possible. Near-α alloys being α alloys with minor fractions of β-stabilisers added. Metastable β alloys contain enough β-stabilisers such that the β phase no longer forms martensite upon fast quenching to room temperature, however unlike the fully stable β alloys, these alloys are still in the α + β range at room temperature and can contain above 50% volume fraction of α phase [4, 5].

By far the most popular and widely used titanium alloy is the α + β alloy, Ti-6Al-4V which consists of 6% (by weight) aluminium, 4% vanadium and the balance titanium. This alloy alone accounts for more than 50% of all the titanium usage worldwide [4]. A pseudo-binary phase diagram for Ti-6Al and V is shown in figure 2.4 on the facing page. The martensite-start temperature is given in this figure as MS and the Ti-6Al-4V composition is shown with the dashed line on the 4 wt. % V composition. Note that as Ti-6Al-4V is an α + β alloy, at temperatures below the β-transus temperature, the alloy exists as a mixture of both α and β phases. Because vanadium has a greater solubility in the BCC β phase of titanium while aluminium is more soluble in the HCP α phase, elemental partitioning exists between equilibrium α and β phases in Ti-6Al-4V, meaning that the β phase will be vanadium rich, while the α phase will be depleted in vanadium as compared to the bulk composition of the alloy. The inverse is true for aluminium [9].

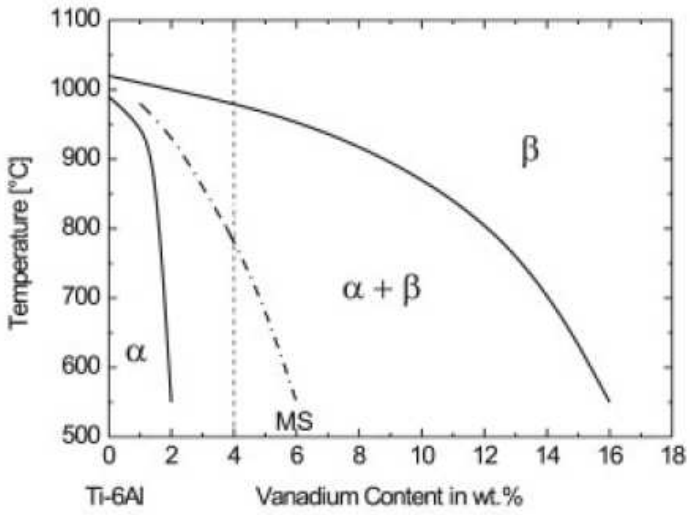

Figure 2.4 – Psedo-binary phase diagram for Ti-6Al and V. MS shows the martensite-start temperature and Ti-6Al-4V composition is shown by the vertical dashed line. Adapted from [4].

2.1.4 Phase Transformations in Ti-6Al-4V

The β-transus temperature of commercial Ti-6Al-4V is normally quoted as being 1000 ° C or just below [10]. When heating from room temperature to above the β-transus temperature, Ti-6Al-4V will go through the α + β region and once above the β-transus temperature, will exist entirely as β phase. If then cooled under equilibrium conditions from this high temperature, the reverse transformation of β→α will occur. If cooling from elevated temperatures at a rate too rapid to allow equilibrium conditions to prevail, non-equilibrium phases can be formed [11]. The details of these transformations are discussed here.

Phase Transformations Upon Heating of Ti-6Al-4V

The transformation from α to β phase upon heating of Ti-6Al-4V is a diffusional transformation and as such is dependent on time, this transformation from α to β phase upon heating can be considered as diffusion controlled growth of the β phase [12, 13]. Elmer et al. [12] conducted research which involved heating Ti-6Al-4V at different rates and taking in situ measurements of the volume fraction of the BCC β phase by means of x-ray diffraction. The experimental findings of this work are given in figure 2.5 on the next page which shows results for 3 different heating rates (2 ° C/s, 10 ° C/s and 30 ° C/s) as well as a thermodynamic prediction based on the equilibrium conditions for Ti-6Al-4V.

As can be seen in figure 2.5 on the following page for temperatures lower than about 925 ° C the measured volume fraction of β phase in the specimen heated at the lowest rate of 2 ° C/s leads that of the faster heating rates and that of the sample heated at 10 ° C/s in turn leads that of the fastest heating rate of of 30 ° C/s. This leads to the conclusion that

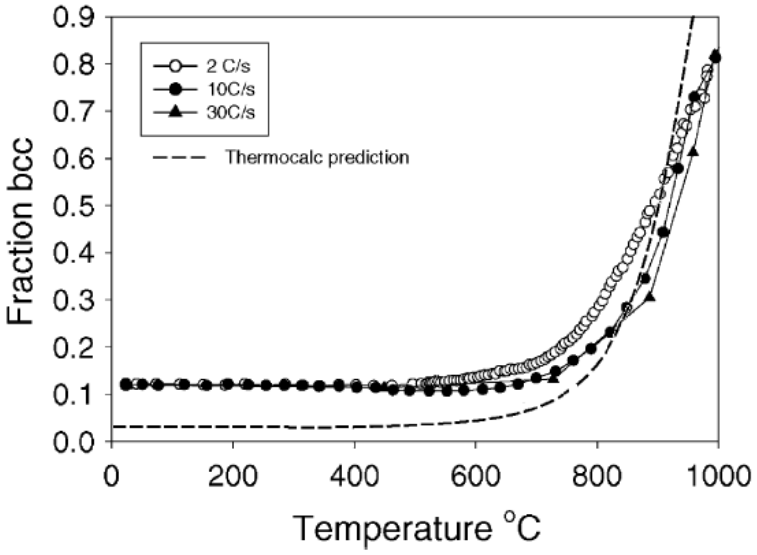

Figure 2.5 – Experimentally measured volume fraction of β phase (BCC) of Ti-6Al-4V heated at 2 ˚C/s, 10 ˚C/s and 30 ˚C/s and a thermodynamic prediction (dashed line) based on equilibrium conditions for the alloy. Adapted from [12].

at temperatures below 925 ˚C the transformation kinetics are limiting the transformation for the sample heated at a rate of 10 ˚C/s and that for the sample heated at 30 ˚C/s, a temperature of 1000 ˚C was required before the diffusional rate caught up to that of the sample heated at 2 ˚C/s [12].

The experimental results in figure 2.5 show significant differences to the thermodynamic prediction. At low temperatures the measured volume fraction of β phase was far higher than predicted. This was due to the manufacturing and processing of the T-6Al-4V, which during cooling was not allowed sufficient time to form the equilibrium amount of α phase from the high temperature β phase by diffusion. At 1000 ˚C, the experimental results did not show the full transformation to β phase as is predicted. This was attributed to either: the possibility of the pickup of oxygen (an α-stabiliser) which would increase the β-transus temperature; or the effects of this high temperature on the x-ray diffraction used to measure the β phase resulting in the underestimation of β phase present at high temperatures [12]. The effect that oxygen content in Ti-6Al-4V has on the β-transus temperature and therefore on the amount of β phase that is present at a given temperature within the α+β region is shown in figure 2.6 on the facing page. As is seen, at a given temperature, the amount of β phase present decreases with increasing oxygen content as a result of the increasing β-transus temperature temperature [14].

Phase Transformations Upon Cooling of Ti-6Al-4V

The transformation of the β phase – present at elevated temperatures – upon cooling is of great importance to the microstructural evolution of titanium alloys during thermomechanical processing (TMP). Of primary importance when cooling Ti-6Al-4V from within

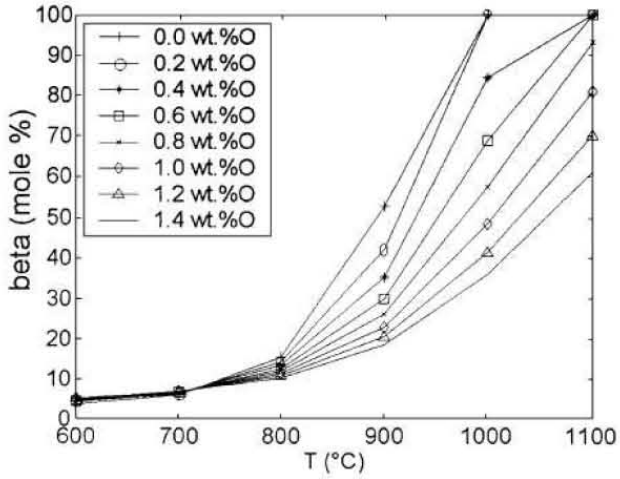

Figure 2.6 – Amount of β phase present at given temperatures for Ti-6Al-4V of different oxygen content. The amount of β phase present at a given temperature decreases with increasing oxygen content as a result of the increasing β-transus temperature [14].

the β region or from high temperatures within the α + β region is the rate at which it is cooled. Slow cooling will result in a diffusional transformation, whereas rapid cooling will result in the β phase undergoing a martensitic transformation [15].

The critical cooling rate below which the β→α transformation will take place by diffusional nucleation and growth of the α phase has been most intensely studied by Ahmed and Rack [15] whose research involved heating Ti-6Al-4V to 1050 ° C for 30 minutes before cooling at different rates to room temperature. The results of this research are shown in figure 2.7 on the next page. A cooling rate of 20 ° C/s was identified as that critical rate below which the transformation takes place by diffusion into an equilibrium structure of α and β phases. A cooling rate in excess of 410 ° C/s was required to create a fully acicular martensite structure and at intermediate cooling rates, the microstructure consisted mostly of acicular α' martensite but some massive α' martensite was also identified, the prevalence of which increased with decreasing cooling rates within that intermediate cooling rate region as shown by the red arrows in figure 2.7.

Malinov et al. modeled a TTT (temperature-time-transformation) curve for Ti-6Al-4V using an artificial neural network approach, which made extensive use of published literature of experimental results to "train" the model. The modeled TTT curve that was produced for Ti-6Al-4V alloys with varying oxygen content is shown in figure 2.8 on the following page. The figure shows "C-curves", which represent the onset of the diffusional β→α transformation, for alloys containing 0.05 wt. % Oxygen, as well as 0.10 wt. % and 0.20% wt. % Oxygen and an experimentally obtained curve is also shown. What these curves predict is that oxygen content has a profound affect on the kinetics of the diffusional transformation and that with increasing oxygen content, the time required for the diffusional transformation to occur is greatly reduced (significant increase in the critical cooling rate) and the temperature at which the transformation most readily occurs is increased. It was noted that this affect of oxygen on the transformation kinetics has

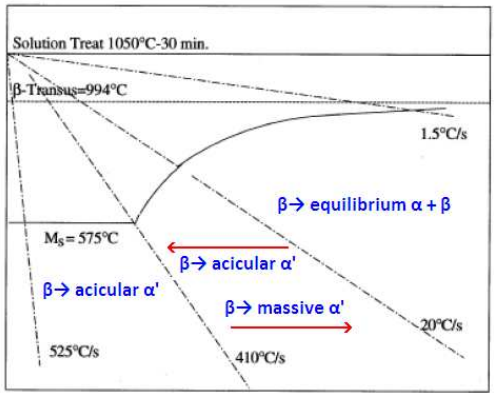

Figure 2.7 – Schematic cooling diagram for Ti-6Al-4V heated to 1050 ˚C for 30 minutes prior to cooling. The different transformations of the β phase that were identified at different cooling rates are given. 20 ˚C/s was identified as the critical cooling rate, below which diffusional transformation took place and 410 ˚C/s was identified as the minimum cooling rate required for a fully acicular martensite microstructure. At intermediate cooling rates, the microstructure consisted mostly of acicular martensite and some massive martensite, the prevalence of which increased with decreasing cooling rates within that intermediate cooling rate region as shown by the red arrows [15].

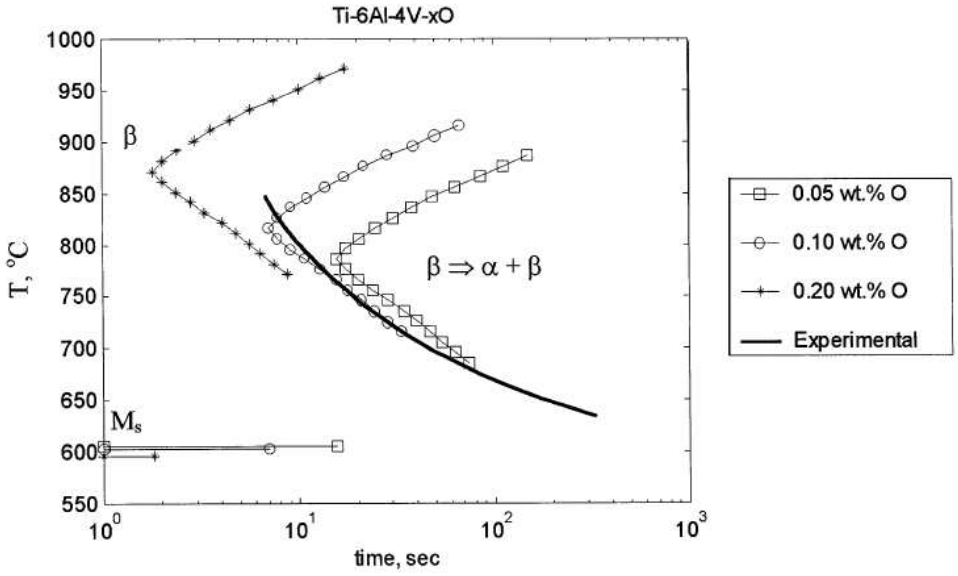

Figure 2.8 – Modeled TTT curves for Ti-6Al-4V alloy containing different amounts of oxygen as well as an experimentally obtained curve [16]

been experimentally observed in Ti–Mo [17] and in VT15 [18] alloys. No explanation for this is offered in the work by Malinov et al. [16] but it is proposed by the authors of this work that it is as a result of oxygen's strong α-stabilising property which results in an increased β-transus temperature, meaning that the driving force for β→α transformation will initiate at a higher temperature (when diffusional kinetics will be accelerated) when cooling from the β phase region. Similarly, for a given temperature within the α+β region, an increased driving force will exist for β→α transformation for an alloy with a higher β-transus temperature.

A further discussion of both diffusional and martensitic transformations occurring within

Ti-6Al-4V follows.

Diffusional β→α Transformation: When the cooling rate from within the β region is slow enough the transformation of β→α will occur by the nucleation and growth of α grains by way of diffusion. The α phase is initially nucleated along the boundary of the β grain as this is energetically favourable. As this α precipitate grows upon cooling, vanadium is required to diffuse out of the newly forming α phase and into the remaining β phase. The diffusion of vanadium in the β phase is slower than that of aluminium and as such it is the elemental partitioning of the vanadium between the two phases by diffusion that controls the rate of the β→α diffusional transformation. As a result of the sluggish diffusion of vanadium into the β phase, the interface between the β and α phases becomes enriched with vanadium, such that the concentration of vanadium at this interface ($C_{V,\alpha/\beta}$) is greater than the vanadium concentration in the bulk β phase ($C_{V,\beta}$) and this interface becomes stabilised and the growth of the α precipitate continues by high aspect ratio lamellae which grow out from the grain boundary α precipitate into the β grain of vanadium concentration $C_{V,\beta}$. This vanadium diffusion and partitioning is shown schematically in figure 2.9. The α phase that is nucleated has a crystallographic orientation related to the parent β grain by the Burgers orientation relationship which gives rise to a limited number of 12 orientation variants that the newly formed α phase can assume. The growth of a product phase into high aspect ratio lamellae that take their orientation from a relationship with the parent grain is knows as a Widmanstätten structure [13].

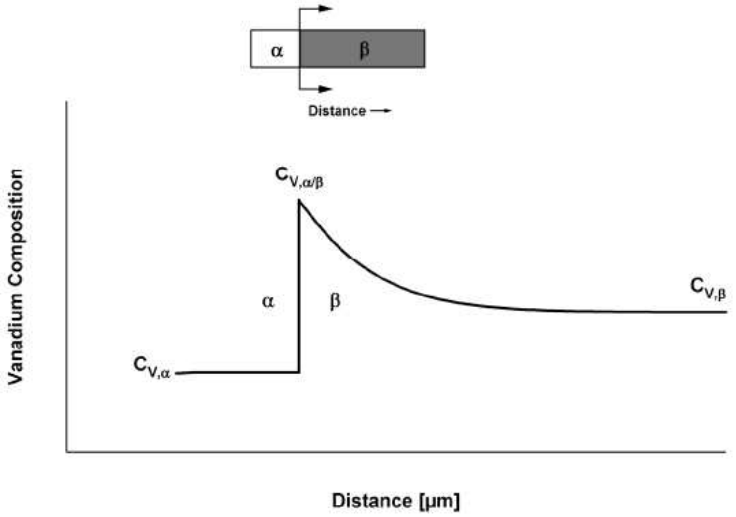

Figure 2.9 – Schematic illustration of the enriched concentration of vanadium at the interface between the β/α phases during the diffusion controlled growth of α phase within a parent β grain which occurs as a result of the sluggish diffusion of vanadium in the β phase as compared to that of aluminium. Note the different equilibrium vanadium concentration of the α and β phases, $C_{V,\alpha}$ and $C_{V,\beta}$ respectively [13].

The growth of these α lamellae which grow from the β-grain-boundary nucleated α precipitate (allotriomorph) gives rise to multiple lamellae of α phase that have some retained

β phase present between them and all share the same crystal orientation. These lamellar packets of shared orientation are known as colonies. Once these colonies have grown upon cooling through the β-transus temperature, further under-cooling will drive the nucleation and growth of further high aspect ratio α lamellae within the interior of the β grain. These α lamellae growing within the prior β grain also take their orientation from the parent β grain by the Burgers orientation relationship in the same manner as those colonies originating from the allotriomorphs. It is possible for these lamellae nucleating in the interior of the prior β grain to form as a colony or to exist as a single lamellae (or a colony of only a few lamellae). In the case of the latter morphology a particular Widmanstätten structure prevails which is termed a basketweave structure. Because the basketweave morphology occurs in the interior of the parent β grain it is most prevalent when cooling from above the β-transus temperature is fast (but still beneath the critical cooling rate) and/or when very large β grains exist prior to cooling as a result of soaking in the β phase region for extended times [13]. The rapid cooling will result in the nucleation of further α lamellae before the grain-boundary colonies have been allowed sufficient time to grow into the interior of the prior-β grain and a large β grain size will ensure that the grain-boundary colonies do not consume the interior of the prior-β grain. The process of nucleation and diffusional growth of an α/β lamellar Widmanstätten microstructure is shown schematically in figure 2.10 on the facing page and light micrographs of Widmanstätten colony and basketweave microstructures are shown in figure 2.11 on the next page.

The thickness of individual lamellae is determined by the cooling rate and a slower cooling rate will result in wider (lower aspect-ratio) lamellae and a higher cooling rate will result in finer (higher aspect-ratio) lamellae [4, 5, 15].

Martensitic Transformations: When Ti-6Al-4V is cooled from above the M_s temperature and the cooling rate is too rapid to allow a diffusional transformation, a martensitic transformation takes place [11].

Ti-6Al-4V has been observed to transform into two different martensites, namely α' having an HCP crystal structure and α" having an orthorhombic crystal structure. The orthorhombic α" martensite is more common in alloys of higher β-stabiliser content and is observed in Ti-6Al-4V to a far lesser degree than α', which can further be split into acicular martensite and massive martensite - also known as packet or lath martensite [5, 11].

As stated earlier, Ahmed et al. [15] found that at very high cooling rates ($> 410\,^{\circ}$C/s) only the acicular α' was observed and that at intermediate cooling rates down to $20\,^{\circ}$C/s the lath martensite was observed as a competitive mechanism. The products of the martensitic transformation obey the Burgers orientation relationship in the same way that the diffusional transformation product does. The acicular martensite is described as consisting of an intimate mixture of needle like plates each having different variation of Burgers relationship. The lath martensite is described as being present in packets of small laths belonging to the same variant of the Burgers relationship, however none of

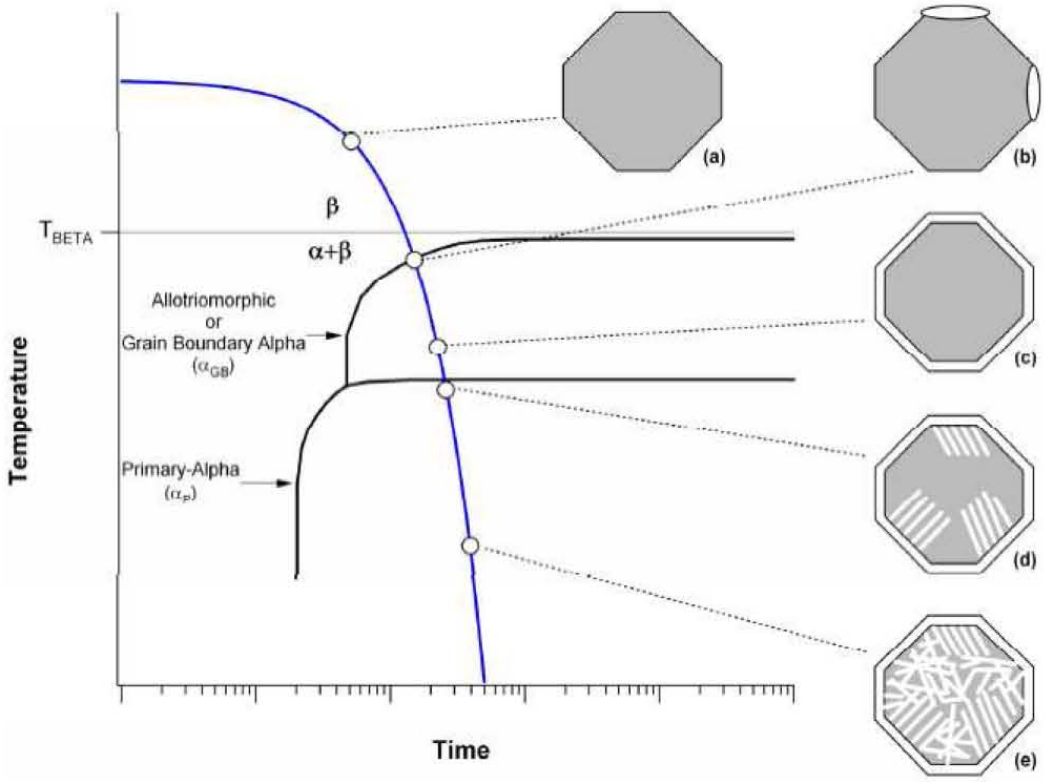

Figure 2.10 – Schematic illustration showing the process of nucleation and growth of a to form an equilibrium a/β microstructure when cooling slowly from above the β-transus temperature. a) shows a single β grain that exists above the β-transus temperature, b) shows the nucleation of grain-boundary a allotriomorphs at temperatures just beneath the β-transus, c) shows the completion of this grain-boundary a, d) shows the growth of a lamellae colonies into the parent β grain from the a allotriomorphs, and finally e) shows the nucleation and growth of basketweave a lamellae in the interior of the parent β grain as cooling continues [13].

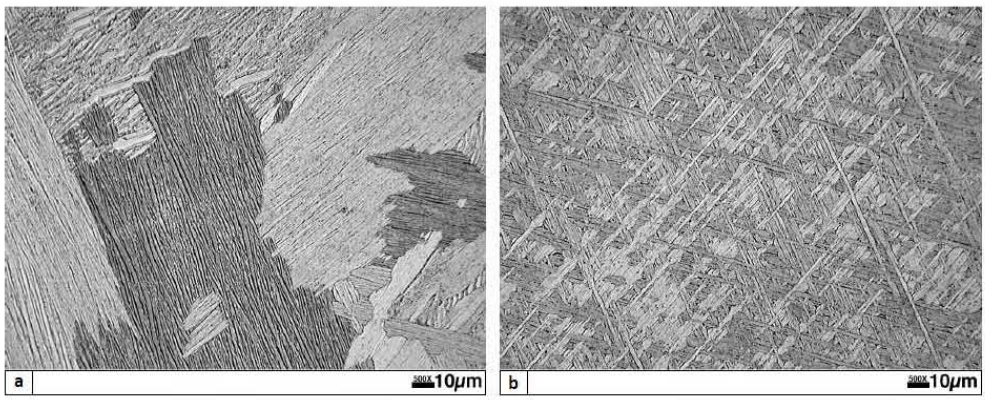

Figure 2.11 – Light micrographs showing a typical Widmanstätten microstructure of a) colony and b) basketweave morphologies in Ti-6Al-4V slow cooled from above the β-transus temperature [13].

the internal features of these packets are visible by light microscopy [9]. Figure 2.12 on the following page shows a light micrograph of acicular a' martensite formed by water quenching Ti-6Al-4V from above the β-transus temperature.

It is worth noting that in many journal papers α' is used to denote only the acicular

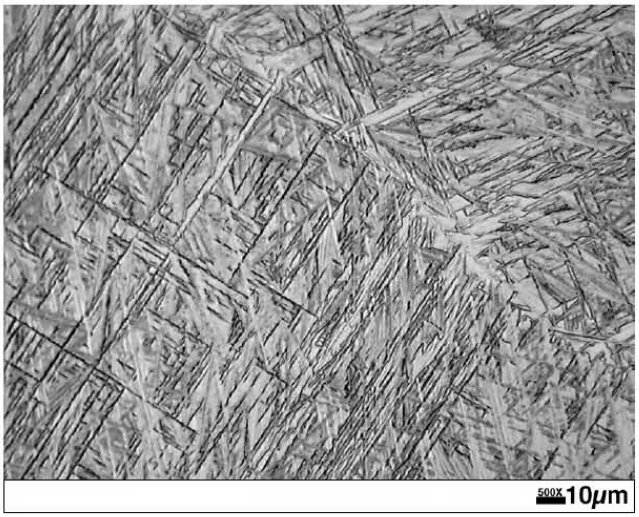

Figure 2.12 – Light micrograph showing acicular martensite microstructure in Ti-6Al-4V water quenched from above the β-transus temperature [13].

HCP martensite and the massive HCP martensite is referred to as massive α, as is the case in [15]. In the current work, as explained above, the α' is used to denote both HCP titanium martensites as per the convention explained in the books [9, 11].

When cooling from within the α+β region, it is possible for martensite to form from the β phase existing at that temperature, provided the peak temperature was above the martensite start temperature (M_s) and that a sufficiently high cooling rate is achieved. What must be considered when cooling from the α+β region is the effect of elemental partitioning between the two phases. Vanadium concentration within the β phase will be very high when little β phase is present and will decrease with increasing β content, until, once passed the β-transus temperature where the vanadium content must obviously be the same as the bulk alloy composition. This means that compositional changes of the β phase present at different temperatures within the α+β region should be taken into account. Lee and Welsch [19] noted an increased prevalence in orthorhombic α" martensite when quenching from temperatures between 800 °C and 900 °C due to the increased vanadium content of the β phase present at this temperature. At temperatures low in the α+β region, the vanadium content is high enough to result in the β phase present being retained to room temperature upon cooling without undergoing any transformation [11, 13, 20].

2.1.5 Differentiating Between the Different Transformation Products

Because equilibrium titanium α created by a diffusional transformation, lath martensite and acicular martensite all have an HCP crystal structure and are all produced by transformation from the β phase whilst obeying the Burgers orientation relationship, it can be very difficult to distinguish between them [15]. Due to their similar crystal structure, electron backscatter diffraction (EBSD) will index all of these structures as being of titanium

α (HCP) phase.

Many researchers have made use of transmission electron microscopy (TEM) to positively identify the different structures [13, 15, 21, 22].

The products of the martensitic transformations are compositionally invariant from their parent structure and as such should show little atomic number variation when viewed by a scanning electron microscope (SEM) using a backscattered electron (BSE) detector [13]. Kelly [13] analysed the microstructures of Ti-6Al-4V cooled at different temperatures using an SEM equipped with a BSE detector. The BSE micrographs from samples that were observed by TEM to be of equilibrium α/β structure and acicular α' martensite and are shown in parts a and b of figure 2.13 respectively. As can be seen from figure 2.13a the

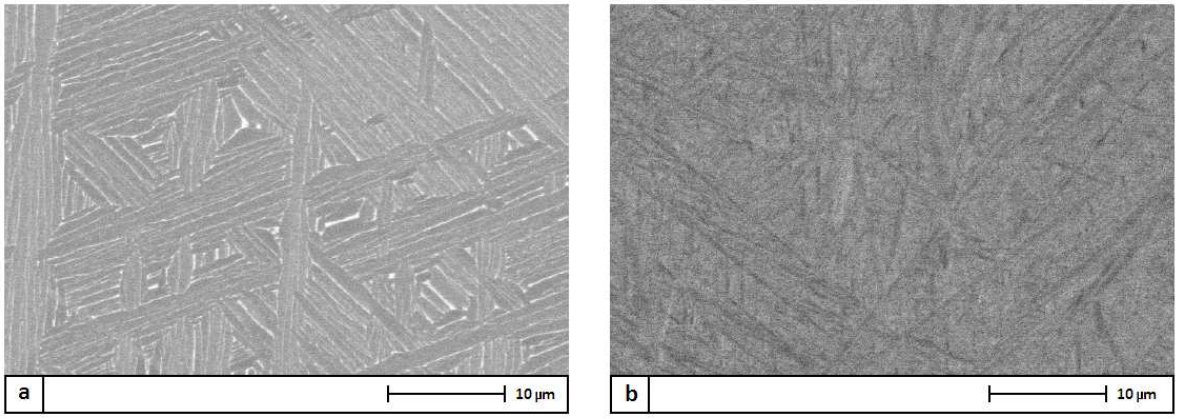

Figure 2.13 – Backscattered electron micrographs of Ti-6Al-4V that has been shown by TEM to be of: a) an equilibrium α/β structure created by slow cooling from above he β-transus temperature and b) a martensitic structure created by water quenching from above the β-transus temperature. Adapted from [13].

elemental partitioning that results from the diffusion controlled creation of an equilibrium α/β structure is clearly evident. The α lamellae appear as dark on the BSE micrograph and the β phase present between the individual lamellae appears far brighter in colour. This is as a result of the β phase being rich in vanadium and as such having a higher atomic number whereas the α lamellae will be depleted of vanadium and therefore show as having a lower atomic number. The micrograph of figure 2.13b showing the martensitic structure shows no such coherent elemental partitioning within the microstructure. That slight contrast that is evident in the BSE micrograph of the martensitic structure was attributed to "electron channeling or preferred orientation contrast and perhaps minute variations in the surface profile" [13].

These findings suggest that even in the absence of TEM, the careful consideration of EBSD, light and BSE microscopy can be used to identify the more common microstructures that exist in the Ti-6Al-4V alloy.

2.1.6 Commercial Processes and Microstructures of Ti-6Al-4V

Typically, Ti-6Al-4V is commercially available in three different microstructures: lamellar, bi-modal, and equiaxed [5,23] and as with other structural metals, the microstructure has a substantial influence on the properties of the alloy [4,22,24].

Lamellar Microstructure

A lamellar structure is formed by the mechanisms shown schematically in figure 2.10 on page 17 and will look similar to that shown in figure 2.11 on page 17. Figure 2.14 shows the processing steps required to manufacture a lamellar structure. As is shown, it can be created by a thermal treatment in which the alloy is heated into the β phase region and allowed to cool. The rate at which this cooling is carried out will determine the thickness of the individual lamellar plates. An aging treatment is commonly used to strengthen the alloy [22].

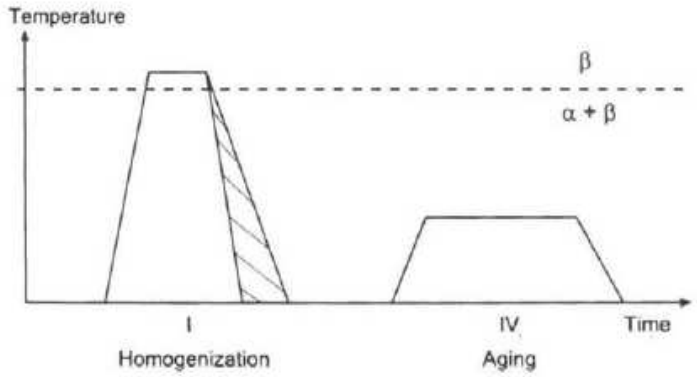

Figure 2.14 – Processing route for creating a fully lamellar microstructure [22].

Bi-modal Microstructure

A bi-modal microstructure comprises both equiaxed and lamellar morphologies and appears (figure 2.15 on the next page) as equiaxed α grains in a matrix of transformed β (lamellar structure). Unlike a fully lamellar structure, a deformation step is required to create a bi-modal microstructure. This is because the equiaxed α grains in the structure are created by a recrystallisation process, which requires strain energy as a driving force to be imparted on the metal by way of plastic deformation [23]. The industrial process for creating a bi-modal microstructure is shown in figure 2.16 on the facing page and begins with a homogenisation step in the β phase, which upon cooling creates a lamellar structure. It is then deformed at an elevated temperature (but below that temperature creating new β phase) followed by a recrystallisation process at a temperature in the α+β region at which the structure comprises of equiaxed α grains as a result of the recrystallisation, and a portion of β grains in accordance with the temperature. Upon cooling, the equiaxed α is retained and the β decomposes into a lamellar structure [22].

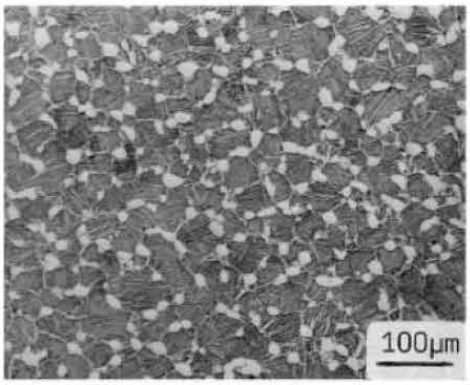

Figure 2.15 – Bi-modal microstructure showing equiaxed α grains and decomposed β grains which form a lamellar matrix [22].

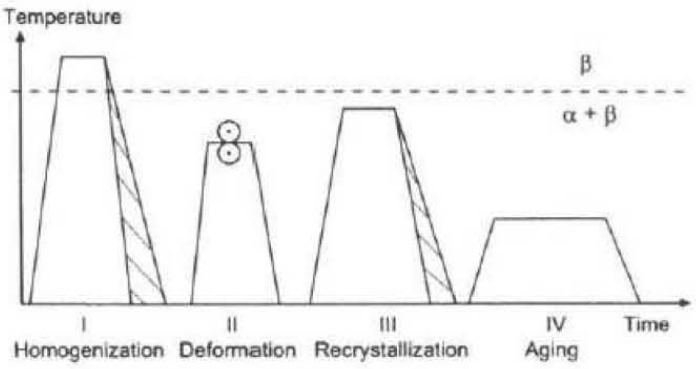

Figure 2.16 – Processing route for creating a bi-modal microstructure in Ti-6Al-4V [22].

Equiaxed Microstructure

An equiaxed structure primarily consists of globular α grains, but does have some retained β phase (around 8%) present at either the grain boundaries or "triple points" (figure 2.17 on the next page). The process for creating an equiaxed structure is very similar to that shown in figure 2.16 for creating bi-modal structures, the only difference being the temperature of the recrystallisation step which, for an equiaxed microstructure, is lower to ensure that no β grains are formed [22].

The temperature of the deformation step when creating either a bi-modal or fully equiaxed microstructure is important. Peters et al. [23], working on controlling microstructure formation, found that with increasing temperature, a greater amount of deformation was required to result in recrystallisation into equiaxed grains. This was attributed to recovery processes being more effective at higher temperatures and therefore limiting the amount of strain energy stored in the material after the deformation step. It was found that at room temperature, a strain of 0.15 was required to cause subsequent recrystallisation, whereas at 1050 ˚C, a strain of 1.2 was required.

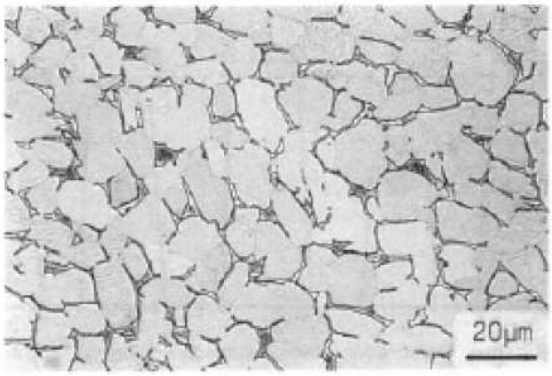

Figure 2.17 – Equiaxed microstructure of a titanium alloy showing globular α grains (light) with β phase (dark) present at grain boundaries and triple points [5].

Effects of Microstructure on Properties

Detailed studies have been conducted into the microstructural parameters existing within the three distinct microstructures and the effect they have on properties of the alloy [22, 23, 25, 26]. A brief comparison of the properties of lamellar and equiaxed microstructures is given by Leyens and Peters [4] and states that while an equiaxed structure has superior strength and ductility, a lamellar structure enjoys better fracture toughness and resistance to fatigue crack propagation (although fatigue cracks do initiate more readily in lamellar structures).

Aging treatment

As shown in figures 1.8 and 1.9, an aging step is used as the final step in the production of Ti-6Al-4V with both lamellar and bi-modal microstructures (and indeed equiaxed microstructures). The reason for this is that Ti-6Al-4V can age harden by the precipitation of Ti_3Al particles. The temperature of this step is important as a Ti_3Al solvus temperature (550 °C for Ti-6Al-4V) exists above which aging will serve only as a stress relieving process and no hardening will occur [22]. Fujii [27] showed that an aging treatment at 500 °C for 4-8 hours resulted in a strength increase of 50 MPa for 0.2% proof stress and 100 MPa for tensile strength and that aging for longer than 8 hours resulted in over-aging and a decrease in strength levels.

2.2 Powder Metallurgy

2.2.1 Introduction

Upandhyay and Agarwal [28] describe PM as the manufacturing of commercial articles from powdered metals and alloys and describe the process, at its simplest, to comprise of four stages:

1. Powder Manufacture
2. Mixing or blending of powders
3. Compacting
4. Sintering

Once the metal powder(s) are manufactured, they are blended together if an alloy is to be used before being compacted into a desired shape. This compact is referred to as the "green compact" and will stay together as a result of mechanical bonding resulting from the compaction but will have no chemical bonds between individual powder particles. This green compact is then heated to some temperature below that of the melting temperature of the main constituent metal. This heating process is known as sintering and allows the individual powder particles to chemically bond together, improving the properties of the material [28].

This is the simplest application of PM, known as "press and sinter", and many different and more complicated processes exist. The process of a simple uniaxial pressing of a green compact is shown in figure 2.18. This process makes use of a die and upper and lower punches.

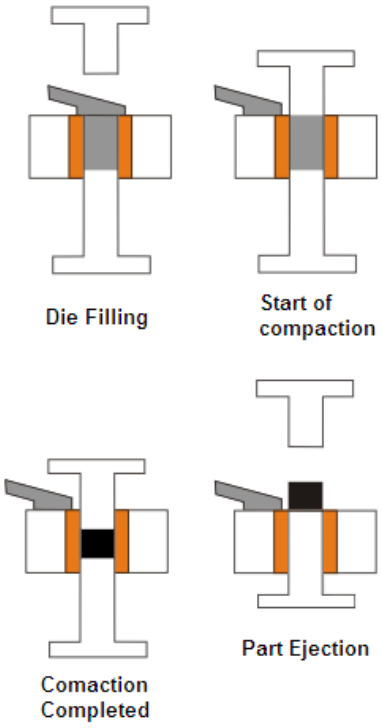

Figure 2.18 – Process of uniaxially pressing powder into a green compact. Adapted from [29].

2.2.2 Reasons for Using Powder Metallurgy

The PM approach was initially used (and still is) to manufacture materials which were difficult or impossible to do so by other means. These materials include cemented carbide

which is produced from powders of tungsten carbide and cobalt which once sintered, result in carbide particles in a tungsten carbide/cobalt alloy matrix. Other materials that were unable to be created by other means were those which made us of PM's ability to create materials with a high degree of porosity such as metal filters or bronze bearings, which made use of the porosity, to be impregnated with oil [30].

As advances were made in the PM industry, it became apparent that the process could be used to create structural parts and to challenge conventional production methods. Early structural parts still contained around 10% porosity and were thus only used when modest engineering specifications were required. The process, however, gained attention as a way of producing components to dimensional specifications at a relatively low cost and as a process that was neither energy nor labour intensive [30].

The level of mechanical properties attainable has since risen considerably due to increased densification and in many materials the mechanical properties attainable by PM are able to challenge those of conventionally produced products [30].

Another considerable advantage to the PM approach is its NNS ability. NNS refers to the production of parts that are very near to their final dimensions once fabricated, with a minimum of machining still required before the final part is complete. As a result of this, PM techniques are very material efficient, using only what material is required and reducing the expense associated with machining [31].

2.2.3 Importance of Density in Powder Metallurgy

Because of the nature of its production, materials produced by PM practices inherently have porosity present in their structure. These pores have detrimental effects on the mechanical properties of the material due to the stress concentration associated with them. As such, when the PM process is used for the fabrication of structural components, the relative density becomes of the utmost importance. Relative density is given as a percentage of the theoretical density of the material, a relative density of 100% being fully dense and a relative density of 90% containing 10% (by volume) porosity [30]. Studies on PM steel have shown that in the region of relative densities of 80 - 100%, static mechanical properties such as tensile strength (Rm in figure 2.19 on the facing page) vary linearly with relative density, but elongation and dynamic properties suffer far more detrimental effects with increasing porosity as shown in figure 2.19 on the next page. The fatigue endurance limit for steel has been shown to have a similar dependence on relative density to that shown by the elongation (A) and impact strength (a_k) in figure 2.19 . This has been accredited to the pores acting as initiation sites for fatigue cracks [30].

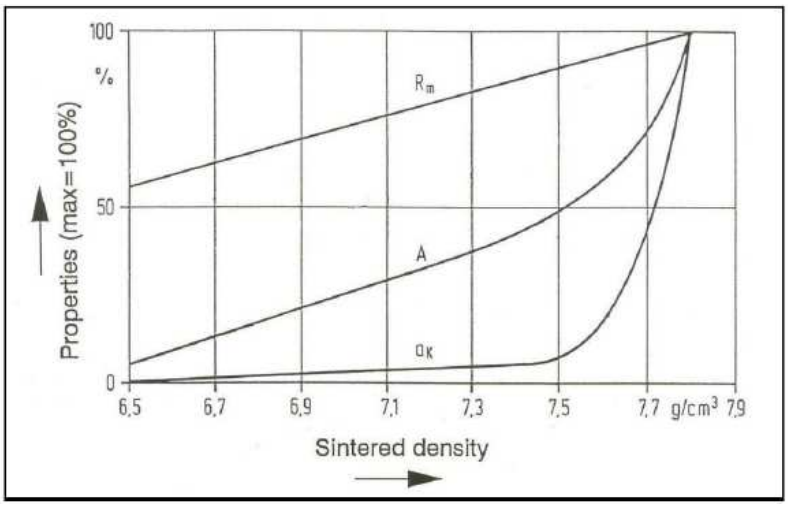

Figure 2.19 – Graph showing the mechanical properties of tensile strength (R_m), elongation at fracture (A) and impact strength (a_k) of sintered steel as a function of its sintered density. Adapted from [30].

2.2.4 Powder Production

Almost all metals can be made into a powder, but the approach used to create that powder depends on the specific material properties of the metal. There are four main categories of powder fabrication techniques, which are: mechanical comminution, chemical reactions, electrolytic deposition and liquid metal atomisation. In addition to these four main categories, there are several specialty techniques for selected materials [31].

The mechanical fabrication and atomisation techniques are described briefly here.

Mechanical Fabrication Techniques

There are four fundamental mechanical comminution processes: Impaction, attritioning, shearing and compression. All four of these make use of physically over-exerting the material until in breaks into finer and finer particles. In order to achieve fine powders, these four processes are often combined in a stirred ball mill or other intense attrition device. Powders produced by mechanical means are typically irregular in shape [31].

Atomisation Techniques

The majority of metal powders are created by atomisation techniques. Atomisation involves the formation of powder particles by rapidly cooling droplets of molten metal. It stands out from other powder production techniques due to its applicability to many alloys and pure metals and the ease of process control, which allows for full control over particle size and chemistry characteristics. Two similar types of atomisation which are widely used are gas atomisation and water atomisation. They both work on the principal of heating a pure metal or alloy beyond its melting point, and allowing a molten stream of this metal to be broken up into a fine spray by means of impacting it with either high

pressure gas or liquid and allowing this fine spray to cool and solidify into a powder which is collected. Various designs on this principle exist and an example of both a gas and water atomiser is given in figures 2.20 and 2.21 respectively [31].

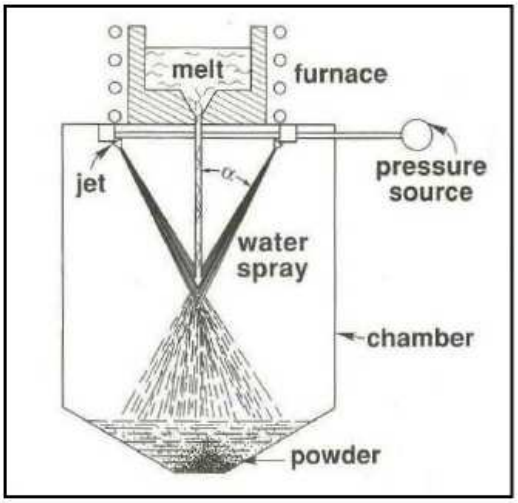

Figure 2.20 – The water atomisation process, where a molten metal stream is disintegrated by water jets [31].

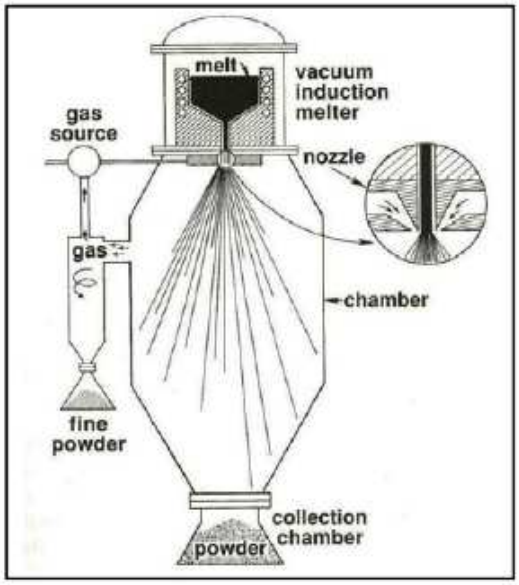

Figure 2.21 – The gas atomisation process, where a molten metal stream is disintegrated by a rapidly expanding gas stream [31].

Both gas and water atomisers can have various ways in which the fluid is directed onto the molten stream, for example it can be done via a single jet, multiple jets or an annular ring. This, together with the many process parameters which include fluid type, residual atmosphere, melt temperature, metal feed rate, fluid pressure, fluid rate and fluid temperature allow the resulting powder characteristics to be tailored for various uses [31].

Differences between the two processes include the degree of oxidation and the morphology of the powder. With gas atomisation, an inert atmosphere is able to be maintained and as such the degree of oxidation is far less than that powder created by water atomisation.

Water atomisation causes the droplets to cool at a far greater rate than those in a gas atomiser which result in the powder being irregular in shape and rough; whereas gas atomisation creates spherical particles [31].

A third atomisation technique is Centrifugal Atomisation. This technique again works by converting molten metal into a fine spray, but instead of doing so by means of impacting it with a high pressure fluid stream, the molten metal is spun and droplets are flung off due to the centrifugal force and cool to form powder. One such process is the Rotating Electrode Process (REP) which heats the metal by means of a stationary tungsten electrode while the desired material acts as the rotating and consumable anode. The anode will be heated to above the molten temperature and spun up to 50 000 revolutions per minute by an external motor. The resulting powder is spherical in shape similar to that resulting from gas atomisation. REP powder contains some contamination from the tungsten electrode which led to the development of Plasma Rotating Electrode Process (PREP) which differs in that the metal is heated by way of a plasma torch, thus avoiding the contamination from the tungsten electrode. The PREP process, like gas atomisation can be carried out in an inert atmosphere and thus it is used for creating powders from highly reactive metals such as titanium [31].

2.2.5 Powder Characterisation

The properties of the powder used in the PM process have a great influence on the properties of the final parts, and as such it is important to have a good understanding of various powder properties and the effect they have on the process [30]. Some important powder characteristics are described here .

Particle Shape and Size

Depending on the process route, individual powder particles can have very different shapes. Figure 2.22 on the following page shows a collection of possible particle shapes and their qualitative descriptors. The great variety of possible particle shapes makes it very difficult to compare sizes of particles of different shapes. The easiest particle shape to quantify the size of is spherical because it requires only a single dimension (diameter) to completely define the particle. As the particle shape becomes more irregular, defining its size becomes more difficult. Figure 2.23 on the next page shows how it is possible to describe the size of an irregular shape particle by a single parameter: an “equivalent” diameter of a sphere that would have the same projected area, surface area or volume of the irregular particle; however techniques making use of such parameters usually do not give equivalent determinations due to differences in measured parameters depending on particle orientation [31].

Screening is the most common technique for describing the particle size of a powder and works by passing the powder through a series of screens or sieves. The screens consist

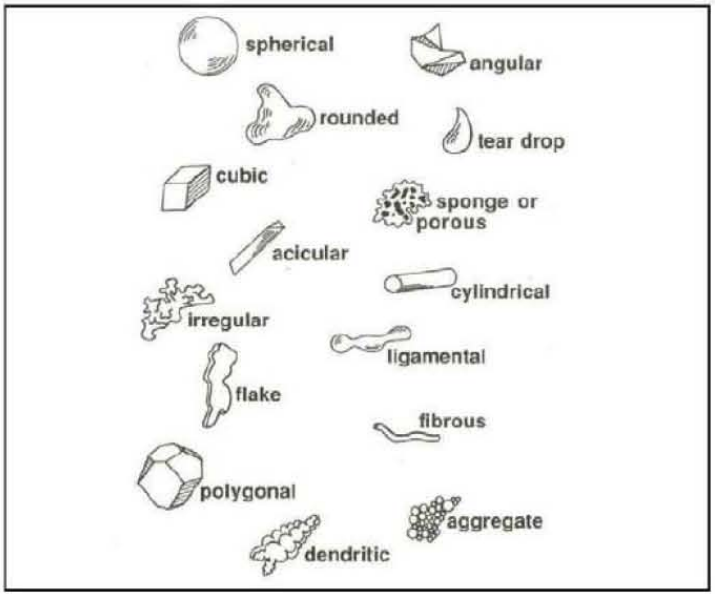

Figure 2.22 – Various particle shapes and the descriptors used to identify them [31].

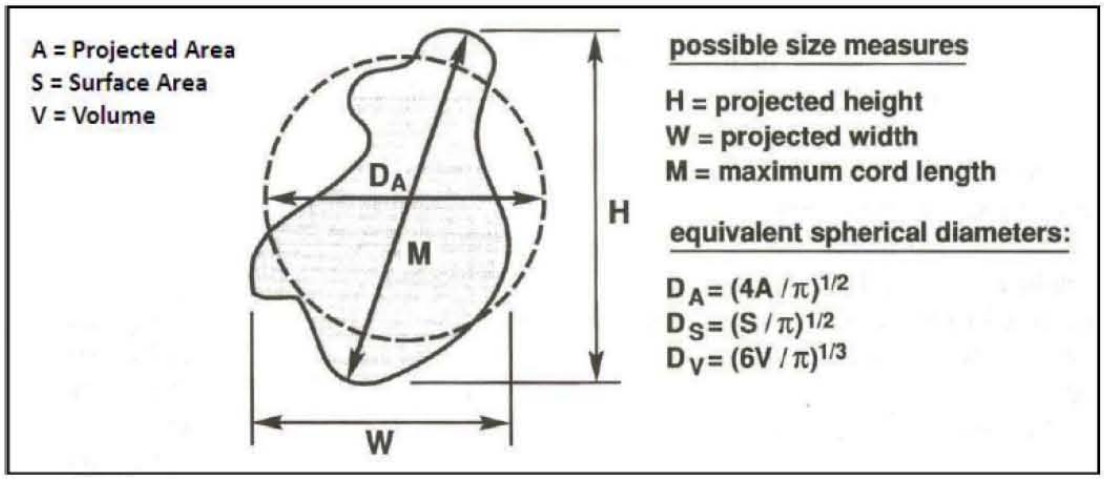

Figure 2.23 – 6 possible measurements for an irregular shape particle based on various projected dimensions of the particle [31].

of square openings created by orthogonal wires of a standard thickness (52μm) and are described by a "mesh" number, which is the number of wires in an inch perpendicular to the wire direction. As such, an increasing mesh number results in smaller openings. The powder that passes through a specific mesh is designated by a - sign and a powder that fails to pass through a mesh is designated by a + sign, for example a powder described as -200 mesh will pass through a 200 mesh screen, a powder described as +200 mesh will not pass through a 200 mesh screen and powder described as -100 +200 mesh will pass through a 100 mesh screen but not through a 200 mesh screen. This technique is carried out by stacking screens with increasing mesh numbers (from top to bottom) on top of one another and placing a sample of the powder in the top screen and then agitating the screen stack for 15 minutes; this is depicted in figure 2.24 on the facing page. It is possible to create conventional screens to a maximum of 325 mesh and as a result, powders of size -325 mesh are termed "subsieve powders". Figure 2.25 on the next page

shows the corresponding opening dimension to different mesh sizes [31].

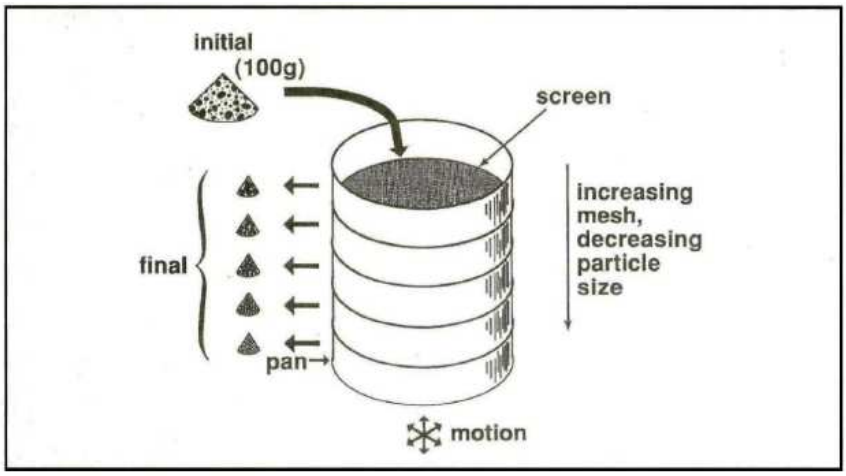

Figure 2.24 – Schematic representation of the screening process to categorise particle size by way of a stack of mesh screens of progressively smaller openings (from top to bottom) [31].

mesh size	opening, μm	mesh size	opening, μm
18	1000	100	150
20	850	120	125
25	710	140	106
30	600	170	90
35	500	200	75
40	425	230	63
45	355	270	53
50	300	325	45
60	250		
70	212		
80	180		

Figure 2.25 – The size of the square openings in the mesh screens for different standard mesh sizes [31].

Powder Impurities

Chemical impurities are problems in all industrial materials and material processes. Impurities are of particular importance in PM, because of the high specific surface area of the powder. A large amount of the material is exposed to the atmosphere and possible impurities during both production and processing. Impurities are very easily picked up through absorption, which concentrate on the surface of particles and thus become included in the final PM part and are detrimental to the achievement of very high density parts. Oxygen is the most important impurity to all metal and non-oxide ceramics [30].

Compressibility

The compaction behaviour of a powder is an important characteristic. A high compressibility is desirable as it will aid the formation of complex shapes and will limit the

dimensional change of the part during sintering, thus allowing for better tolerances on completed parts. The compressibility is measured by pressing powder into a simple cylindrical or rectangular die under a predetermined pressure (usually around 414 MPa) and then measuring the relative density of the resulting green compact [31].

2.2.6 Powder Compaction

Most PM techniques make use of an external pressure to compress the powder and create a green compact before sintering. The density of a powder that has not been agitated at all, is termed the "apparent density" and is controlled by the particle friction within the bulk powder. A compacting step will increase the density from that of apparent density up to the density of the green compact. This densification has been shown to comprise of different key stages as shown in figure 2.26. An initial increase in density is achieved purely by the rearrangement of the powder particles so that smaller pores exist. The next stage involves the plastic deformation at the localised contact points between powder particles. The area of these contact areas enlarges because of the plastic deformation and allows for new contact points to be made. Once these point contacts have plastically deformed, causing the points to work harden, and the contact area has enlarged, further pressure will cause a homogenous deformation within the powder particles. At very high pressures, exceeding 1 GPa, The powder compact starts to behave as a dense solid, and deforms as a bulk material. Continual pressurisation beyond this point will yield no further densification. A schematic representation of how this compaction occurs is given in figure 2.27 on the next page [31].

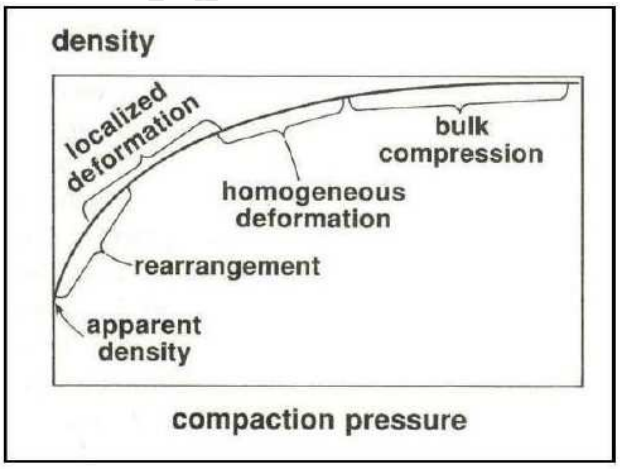

Figure 2.26 – Sketch showing the key stages and mechanisms for increasing the density of powder compacts with increasing compacting pressure [31].

2.2.7 Sintering

Sintering is the bonding together of particles under the influence of high temperature. It can be achieved at temperatures below the melting temperature of the powder. The

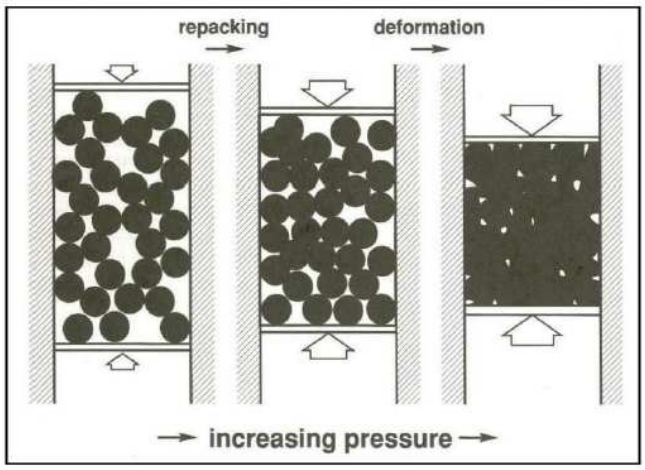

Figure 2.27 – A schematic representation showing the densification mechanisms introduced in figure 2.26 on the preceding page at work during uniaxial pressing [31].

primary driving force for sintering is the reduction of surface energy. Because of its nature, powder has a very high specific surface area and the surface area per unit volume is inversely proportional to the particle diameter. As such, smaller particles have a greater surface area per unit volume and sinter faster than larger particles. Another driving force for sintering is the reduction of any strain energy existing in the powder particles as a result of the compaction process [31].

The theory of sintering is shown for spherical particles in figure 2.28 on the following page. The first step is for contacting particles to bond together, forming a neck between them, this bond between the particles will enlarge as sintering progresses. If infinite time is allowed, the theory suggests that the two spheres will completely coalesce into a single sphere, having a diameter 1.26 times that of the original particles [31].

In a green compact, any individual powder particle has several contacts with neighbouring particles and bonds will develop between all of them. Grain boundaries will initially form along the particle boundaries, replacing the solid-vapour interface and during the latter stages of sintering, when porosity is less, it is common for these grains to grow. The rate of sintering varies greatly over the process. The initial rate of sintering is quick and involves rapid growth of the interparticle neck. Later, when grain growth is occurring, isolated porosity can hinder the grain growth and slow the sintering process. The final stage of sintering will feature isolated spherical pores which, if filled with gas, will limit the final attainable density; thus vacuum sintering can produce high final densities [31].

2.2.8 Full Density Techniques

The PM processes explained already in this literature review comprise the basics of the PM industry. There are many other processing techniques that are aimed at achieving very high density and high performance PM products. The control over material texture, segregation, grain size, inclusion population, microstructure and product homogeneity

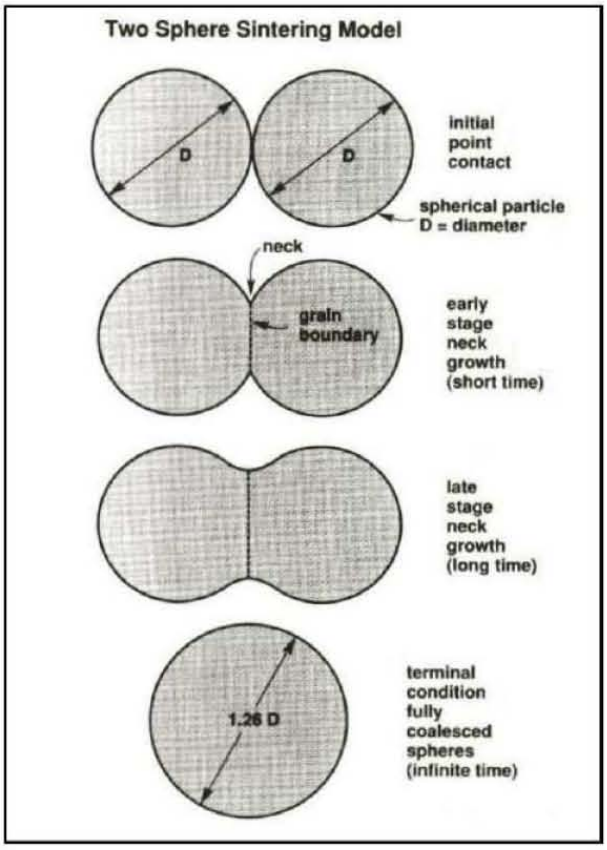

Figure 2.28 – Two sphere sintering model, showing how two particles develop a bond at the point contact, which grows into a neck and how in enough time the 2 spheres will eventually coalesce into a single large particle [31].

that PM offers means that when full density (100% relative density) is achieved, the performance levels may exceed those of wrought material. As a result of this, there has been considerable exploration of full density PM processing. Full density processing is costly, and should only be used when the application demands the high mechanical performance it offers. In applications when high mechanical performance is not demanded, a simple press and sinter approach will be far more cost effective and appropriate [31].

The full density approaches that are of most industrial importance are those of isostatic pressing. In these approaches the consolidating of the powder is by means of an isostatic pressure applied by a fluid. By applying the pressure isostatically, the compaction stress (and therefore density) gradients that are associated with uniaxial pressing are avoided. Isostatic pressing can be categorised as being either cold isostatic pressing (CIP) or hot isostatic pressing (HIP) [31].

The process of CIP consolidation is used to create a high density green compact and subsequent sintering will be required. The HIP process however, combines the powder consolidation and the sintering processes. The CIP process is achieved by placing the powder in a “flexible bag”, inside a pressure vessel which normally uses a liquid to transmit the pressure to the powder. The resulting green compact will then be removed from the bag to be sintered [30].

The HIP process is similar to that of CIP; however a gas is used to convey the pressure to the powder. HIP processes can be separated into “encapsulated HIP” and “containerless HIP”. Encapsulated HIP is analogous to the CIP process, in that a flexible bag or “can” is used to contain the powder during the process. This has the advantage of not letting the pressurising gas into contact with the powder, which could fill the pores and inhibit full density being achieved during the process. Unlike in the CIP process however, the flexible bag cannot be made of a simple polymer, as it will have to withstand the very high sintering temperatures and as a result the high cost of the required tooling becomes one of the limiting factors in the process. Containerless HIP gets around this problem of gas occupying the pores in the compact by sintering the powder without any pressure applied until a density of between 90 and 93%, at which point the pores are closed, gas cannot infiltrate the compact and the HIP process can continue without any flexible bag [30]. Figure 2.29 shows a schematic drawing of the encapsulated HIP process.

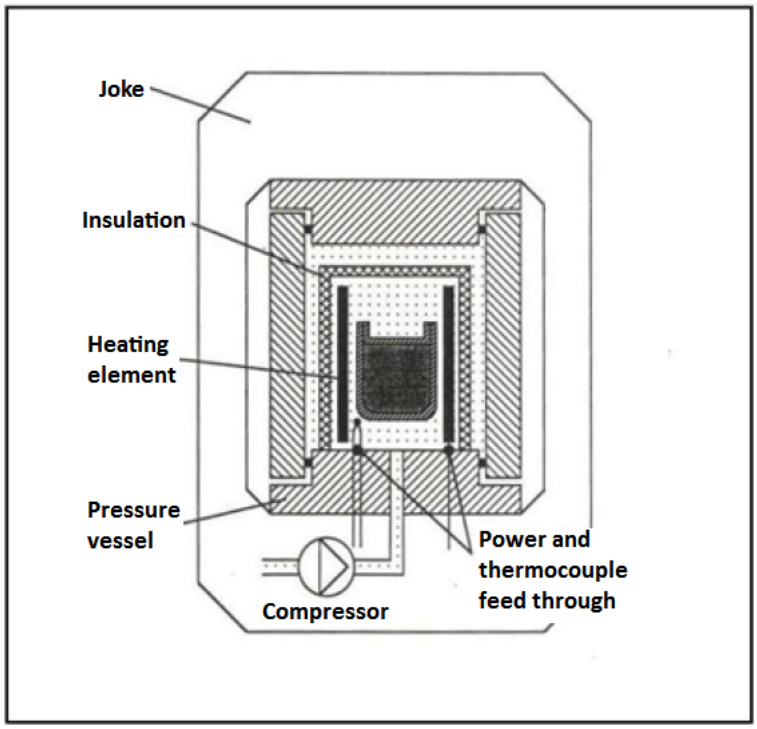

Figure 2.29 – A schematic representation of the components involved in the HIP process. The powder in the "can" can be seen inside the furnace [30].

2.2.9 Titanium Powder Metallurgy

Pre-Alloyed and Blended Elemental Powder

The production of titanium alloys via the PM route can be separated into two approaches, depending on the starting stock from which the powder is fabricated. The two approaches are pre-alloyed (PA) and blended-elemental (BE). PA powders are chemically alloyed prior to being fabricated into powders and each powder granule will comprise all of the

elemental constituents in their alloying compositions. As an example, a PA Ti-6Al-4V powder will be created from ingot Ti-6Al-4V stock. PA powders are almost always created by atomisation techniques such as the PREP technique described in 2.2.4 on page 25 [3].

BE powders are blended from separate elemental powders (or master alloy powders) according to alloy composition and therefore each individual powder particle will purely be one single element of the alloy [3]. Whereas PA powders are primarily produced by atomisation techniques, the titanium used in BE powders is usually made from sponge fines, the hydride de-hydride process (HDH) or an electrolytic process [8].

The Kroll process for producing titanium by traditional ingot technology extracts titanium from titanium-tetra-chloride as a "sponge-like" material which is easily subsequently milled into sponge fines. These sponge fines provide the main source of powder for the BE method. The HDH process can produce powder from ingot titanium by hydrogenating the ingot material which will embrittle it and allow it to be easily ground to a powder in a mill followed by a subsequent dehydrogenation process [8].

Current Titanium Powder Metallurgy Applications and Research

Much research has been conducted into creating high density, high performance PM titanium and titanium alloys to compete with conventional ingot IM products using PA powders and HIP or other full density techniques [2, 8, 32, 33]. Because PA powders are created from alloy ingots, the advantage to using the PA PM technology as opposed to conventional IM is due largely because of its NNS ability [6].

Within the aerospace industry, the term "buy-to-fly-ratio" is used to express the ratio of the mass of wrought material needed to manufacture a final part by way of machining to the mass of that final part. Many titanium parts have a very large buy-to-fly-ratio and because of the expense of that titanium waste as well as the high cost of machining titanium alloys, it proves costly to machine a part from wrought titanium [2]. The NNS and economy-of-material abilities of the PM process therefore make the creation of fully dense parts by PA methods very attractive.

It is well documented that fully dense titanium alloy parts can be fabricated from PA powders [32, 33] and indeed this approach has been implemented in the aerospace industry to manufacture aircraft components [1]. But all of these cases have required costly methods such as HIP or powder forging techniques.

BE powders have received attention as a possible route to low cost production of titanium alloy parts. Because of their production from titanium sponge, BE powders are considerably cheaper than PA powders, and therefore in addition to the NNS and economy-of-material attractions that it shares with the PA process, a BE production approach has the added advantage of using low cost starting feedstock [1].

The difficulty in producing parts by the BE method stems from the purity of the powders, which Heaney and German [34] describe as "the primary issue with fabrication of parts

directly from powder". Powders made directly from sponge fines have a high residual chloride content which prohibits the achievement of full density parts [8,35]. HDH powders have lower chloride levels but in the past have been considerably more expensive and tended to have a higher oxygen content; however, this is no longer the case and HDH powders are becoming a viable source for the BE approach [35].

To illustrate the difficulties of the BE approach, Duz et al. [36] report that in order to achieve the desired levels of mechanical properties, PM titanium parts should have a density exceeding 98% of that of theoretical, and that the BE approach normally does not exceed 95%.

Researchers have however managed to produce titanium alloys of over 99% theoretical density using the BE method: by means of direct powder rolling (DPR) [37]; by means of using a process of CIP, sintering, followed by HIP [8]; by a simple press and sinter approach [36]. Figure 2.30 , shows the process of DPR.

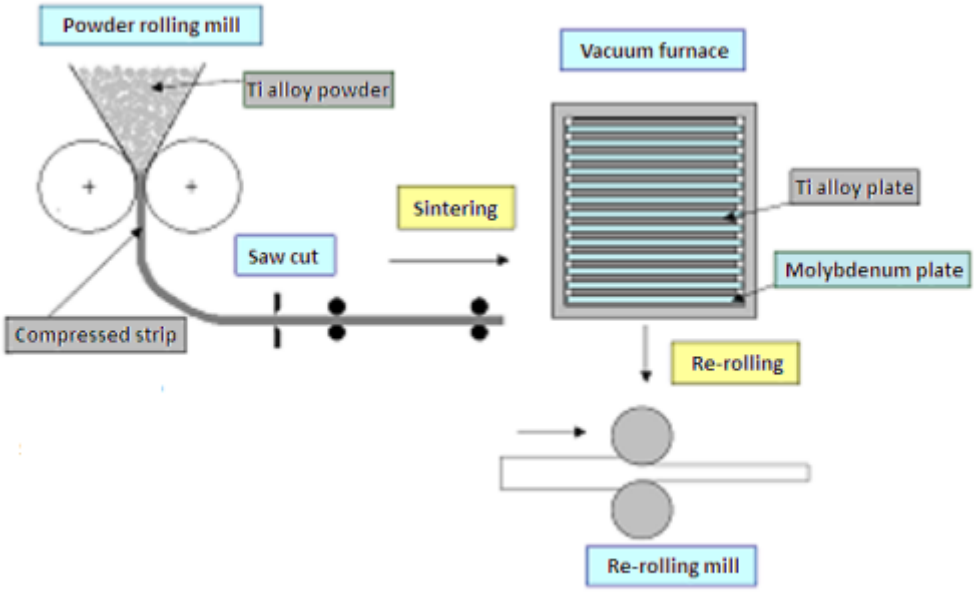

Figure 2.30 – Schematic representation of the direct powder rolling (DPR) process involving initial rolling of the loose powder, followed by sintering and a further rolling step. Adapted from [37].

Sintering Ti-6Al-4V

Heaney and German [34] conducted studies into sintering titanium in both an argon atmosphere and under high vacuum conditions and found that the vacuum produces better results than the argon atmosphere. Studies into the sintering of Ti-6Al-4V show that the process begins at a temperature of 1000 ° C and that temperatures exceeding 1200 ° C are required for complete sintering [35].

Research into the sintering of Ti-6Al-4V involving sintering trials at both 1290 ˚C and 1300 ˚C found that even at such high temperatures, a small improvement in as-sintered density was evident at the higher temperature [34]. Many other researchers have conducted pressureless sintering of Ti-6Al-4V at temperatures between 1238 ˚C and 1260 ˚C [38–40].

2.3 Uniaxial Compression

Uniaxial compression specimens are cylindrical in cross-section and have a height to diameter ratio of less than 2 to avoid buckling during compression. During uniaxial compression, the samples are loaded axially and plastically deform such that the height of the cylindrical specimens is reduced [41].

2.3.1 Friction and Barreling During Uniaxial Compression

The friction that exists between the specimen and the platens at their interface impedes the plastic flow of the specimen near to this interface and this results in "barreling" of the compressed sample. This barreling process is shown schematically in figure 2.31 [41].

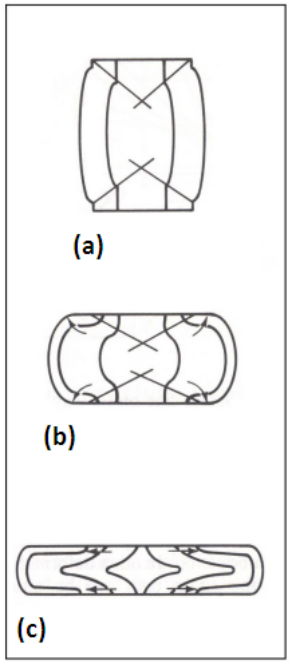

Figure 2.31 – Schematic drawing showing the barreling of a uniaxial compression specimen as deformation increases from a-c. Compression axis being vertical [41].

Efforts to reduce this friction can be taken by utilising lubricants between the specimen-platen interface but the friction cannot be completely eradicated.

The flow stress measured using uniaxial compression can be corrected for friction by means of the following equation:

$$\sigma = \frac{4F_i}{\prod d_i^2}\left(1 + \frac{\mu d_i}{3l_i}\right)^2$$

Where μ is the coefficient of friction at the specimen-platen interface and F, d and l are force, diameter and length (height) respectively and for all equations presented here the subscripts o, f and i denote original, final and instantaneous measurements respectively [41, 42].

It is not considered necessary to correct for friction when calculating the flow stress as long as the barreling coefficient (B) is not less than 0.9, where B is given by:

$$B = \frac{l_o d_o^2}{l_f d_f^2}$$

Where friction can be neglected, the stress is given by:

$$\sigma = \frac{4F_i l_i}{\prod l_o d_o^2}$$

And strain by:

$$\epsilon = \ln\left(\frac{l_o}{l_i}\right)$$

2.3.2 Characteristics of Deformation by Uniaxial Compression

Friction at the specimen-platen interface restricts the plastic flow of the material in this region. As such, very little strain is imparted onto the specimen in the region of the interface and the strain is concentrated near to the centre of the sample. Therefore, if a specimen is deformed to a nominal compressive strain, this strain will not be uniformly distributed throughout the specimen, with the regions near to each of the platen contacts having less strain than the nominal value, while the centre region experiences a strain greater than the nominal value [41].

This strain distribution is easily seen in the modeled simulation of a steel specimen deformed to 50% compression shown in figure 2.32 on the next page. In this figure, the grid pattern in the undeformed material was square and the compression axis was vertical.

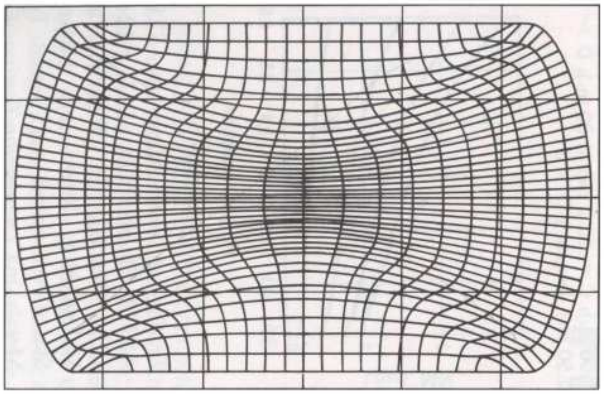

Figure 2.32 – A modeled simulation of a steel sample uniaxially compressed to 50% showing the strain distribution within the sample. Grid pattern was initially square and compression axis was vertical [41].

2.4 Plane Strain Compression

2.4.1 Plane Strain Compression Tests

Plane strain compression (PSC) tests are predominantly used to simulate deformation conditions experienced in industrial rolling operations, either at ambient or elevated temperatures, as the mode of deformation are very similar [43–45].

The basic PSC testing setup is shown in figure 2.33. Of great significance in a PSC test is the ratio of platen width to specimen thickness (w/h) ratio. The requirements for a PSC test as prescribed by the ASM handbook [41] requires that the width of the specimen be at least 6 times the breadth of the platens (i.e. $b/w > 6$) and that the w/h ratio should at all times be between 2 and 4.

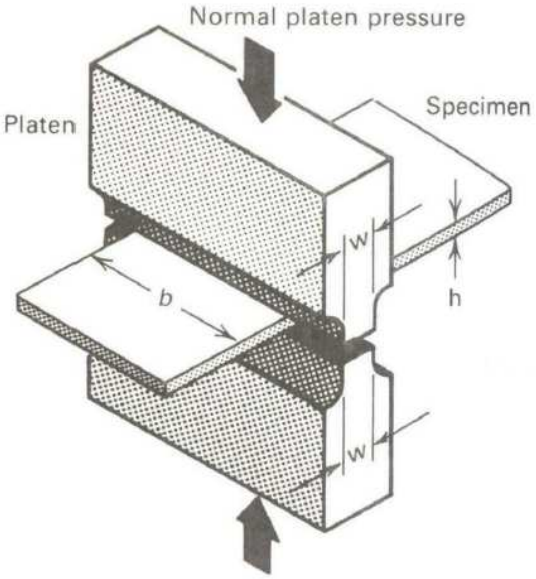

Figure 2.33 – PSC testing setup. Adapted from [41].

The true stress and true strain in a PSC test can be given by the following equations

respectively:

$$\sigma_{psc} = \frac{F_i}{wb}$$

$$\epsilon_{psc} = \ln\left(\frac{h_o}{h_i}\right)$$

Where F is the deformation force and the subscripts o and i represent original and instantaneous conditions respectively [41].

When comparing the true stress associated with PSC conditions to those occurring during uniaxial compression, the PSC conditions result in the mean pressure on the platens being 15.5% greater than those associated with uniaxial compression. Because of this, the true stress-strain curve in uniaxial compression can be obtained from the corresponding PSC compression curve through the following equations [41]:

$$\sigma = \frac{\sqrt{3}}{2}\frac{F_i}{wb}$$

$$\epsilon = \frac{2}{\sqrt{3}}\ln\left(\frac{h_o}{h_i}\right)$$

2.4.2 Characteristics of Deformation by PSC

For frictionless conditions the slip line field patterns for PSC typically appear as 45 ° lines originating from the platen-edge - specimen contact and the influence of the w/h ratio on these field patterns are shown in figure 2.34 [46].

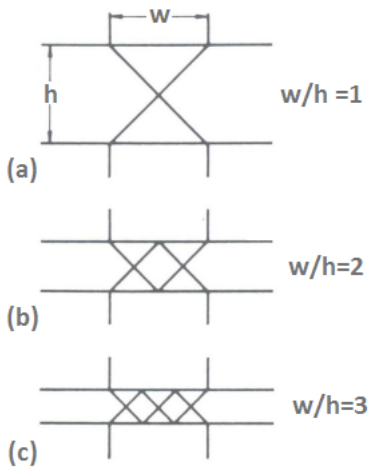

Figure 2.34 – Influence of w/h ratio on slip line field patterns during PSC testing [46].

Beynon and sellars [46], working on aluminium, showed that the field patterns shown in figure 2.34 on the preceding page were most clearly visible in the test specimen when the compression was carried out to low strain values. This is due to that fact that at high strain values, the ever changing w/h ratio - due the reducing of h as a result of the compression - distorts these field patterns. It was found that when high strain values were applied, a strain profile as shown in figure 2.35 resulted within the sample.

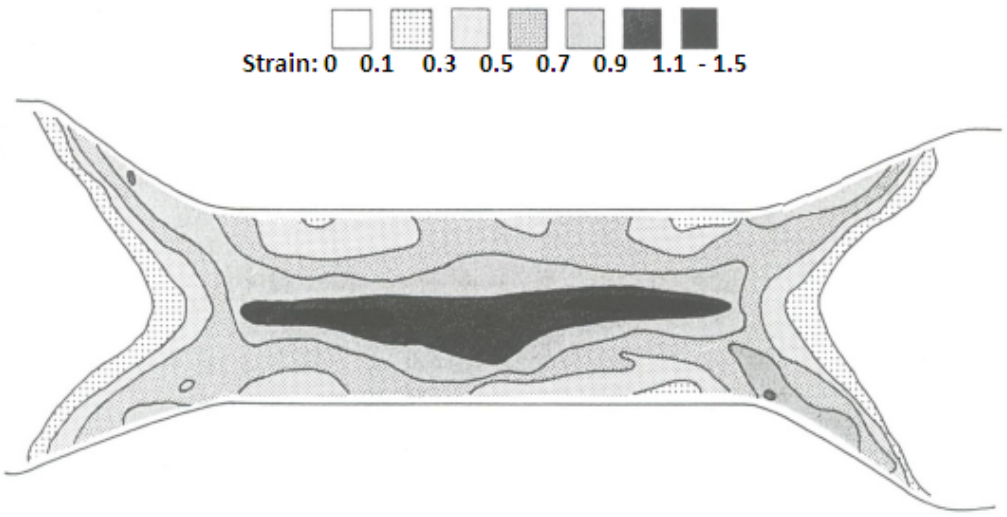

Figure 2.35 – Strain distribution in aluminium after undergoing PSC to a nominal strain of 0.742 [46].

2.4.3 Asymmetric Deformation During PSC

In addition to the strain inhomogeneity that exists within a specimen having undergone PSC, it is also possible for the specimen to deform asymmetrically under PSC test conditions. Work done by Duckham and Knutsen [43] in this regard, accredited the phenomenon of asymmetric deformation to lateral offset of the compression platens (measured to have a maximum of only 1.5% of the platen width). This lateral offset is thought to be exaggerated by inconsistent localised friction, resulting in a lateral force on the platen. A macroscopic representation of the in situ appearance of samples undergoing symmetric and asymmetric compression is given in figure 2.36 on the facing page with a typical micrograph of the resulting microstructure given adjacent.

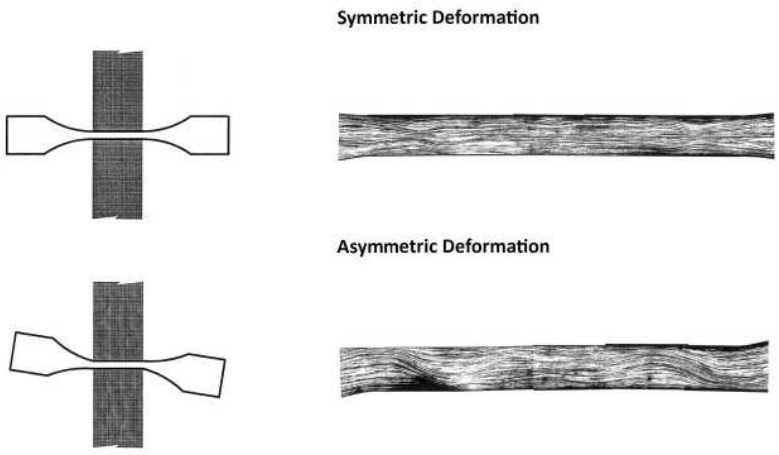

Figure 2.36 – Macroscopic view of the deformed specimens in situ and micrographs of the microstructure resulting from both symmetric (above) and asymmetric (below) deformation. Adapted from [43].

2.5 Thermomechanical Processing of Conventional Titanium Alloys

2.5.1 Recovery and Recrystallisation

The stacking fault energy (γ_{SFE}) of a material can be interpreted as a measure of the ability of dislocations within the material to undergo dislocation climb and cross-slip. A high γ_{SFE} value means that dislocation climb and cross-slip can readily occur so long as sufficient thermal energy is available to do so, whereas a low γ_{SFE} value means that dislocation climb and cross-slip will not readily occur [47].

The plastic deformation of polycrystalline metals will introduce dislocations into the microstructure of the metal and therefore increase the stored strain energy within the microstructure. As a result of this increased strain energy and due to the second law of thermodynamics, a driving force - the minimisation of stored energy - exists for reducing that strain energy. Two mechanisms by which which this strain energy can be reduced is by recovery or by recrystallisation. Both of these mechanisms require thermal energy to occur, and as such both are capable of occurring during the elevated temperature TMP of metals [47].

The process of recovery involves the re-arrangement of dislocations (introduced into the microstructure by plastic deformation) by dislocation climb and cross-slip into an arrangement that equates to the lowest possible energy state. This process is shown schematically in figure 2.37 on the next page and results in sub-grain boundaries ($< 15\,^{\circ}$C) being created as is shown in figure 2.37b [47].

Recrystallisation reduces the strain energy within the microstructure of a metal by the creation of new strain-free grains which nucleate and grow out of the deformed microstructure. These recrystallised grains will nucleate preferentially along the old-grain boundaries

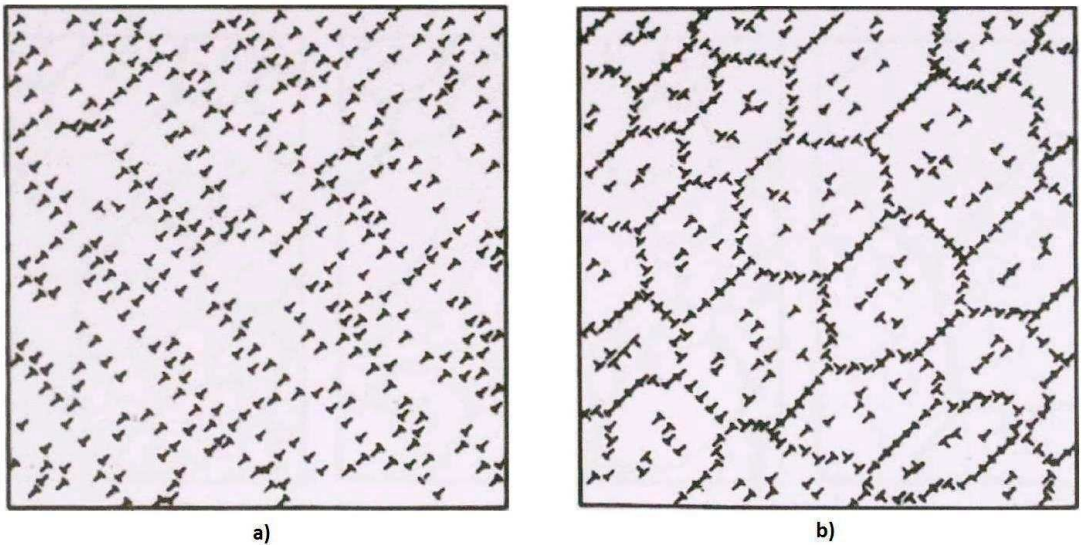

Figure 2.37 – Schematic illustration of the phenomenon of recovery whereby dislocations introduced into a grain by plastic deformation (figure a) are rearranged into a sub-grain structure of lower stored energy (figure b) than that of the randomly arranged dislocations [48].

as these boundaries represent the areas of highest energy. The process of recrystallisation is shown schematically in figure 2.38. The process will begin with the creation of new (strain-free) grains along the old-grain boundary (figure 2.38a) and once that process is complete (figure 2.38b), new grains will be created within the interior of the old-grain (figure 2.38c) until the microstructure consists entirely of these new recrystallised grains (figure 2.38d) [47].

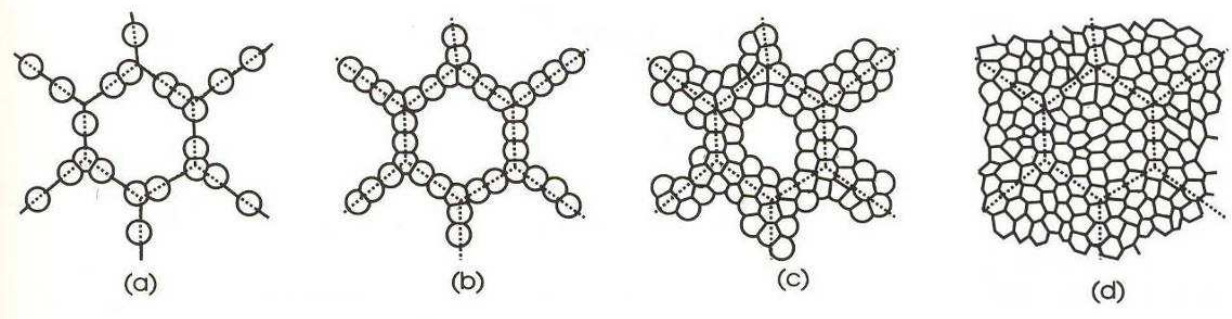

Figure 2.38 – Schematic illustration of the process of recrystallisation whereby new strain-free grains nucleate first along a deformed old-grain boundary (figure a and b), then later in the interior of the old-grain (figure c) until the old-grain has been entirely recrystallised into new strain-free grains (figure d). Adapted from [47].

Following this recrystallisation process, once stage d) from figure 2.38 has been reached and the structure consists entirely of newly nucleated small grains, grain growth will take place driven by the reduction of the energy associated with grain boundary area [47].

As both recovery and recrystallisation are driven by the reduction of strain energy, they can be seen as competing mechanisms, however they often occur concurrently, with recovery often seen as a necessary precursor to recrystallisation as it creates the embryo for

the strain-free recrystallised grains to nucleate from [47].

Because recovery occurs by way of dislocation climb and cross-slip, and a high γ_{SFE} means that dislocation climb and cross-slip can readily occur, a material with a high γ_{SFE} will have a high rate of recovery, whereas a material with a low γ_{SFE} will undergo sluggish recovery. As a result of this, recrystallisation is the dominant mechanism for alleviating strain energy in a deformed material with a low γ_{SFE} as recovery will be slow [47].

The explanation of recovery and recrystallisation given thus far is easily understood for a material that has been deformed and therefore had strain energy introduced into the microstructure and has subsequently been subjected to a heat treatment such as an annealing process. In this process, the thermal energy provided by the annealing treatment will provide the means by which the recovery and recrystallisation can occur. These processes are called static recovery and static recrystallisation. However, because TMP often involves plastic deformation at high temperatures, both the driving force of induced strain and the thermal energy required for recovery and recrystallisation to occur are present and therefore recovery and recrystallisation can occur during TMP when the temperatures and imposed strain are both sufficient. When occurring like this, the processes are called dynamic recovery (DRC) and dynamic recrystallisation (DRX) [47].

It is possible for the initial stages of recovery and recrystallisation to begin during hot deformation and be continued statically during any subsequent dwell or cooling processes and when this is the case the processes are termed metadynamic recovery and metadynamic recrystallisation [47].

As can be imagined, when recrystallisation has taken place during high temperature TMP, it is difficult to determine exactly when this recrystallisation took place i.e. was it dynamic or metadynamic recrystallisation and as such ambiguity exists within scientific literature as to the extent to which either of these phenomena take place.

Dynamic Recrystallisation in Ti-6Al-4V

When deformation of Ti-6Al-4V takes place within the $\alpha + \beta$ temperature region, their is no consensus within the published literature as to whether or not DRX occurs. Furuhara et al. [49] proposed that DRX does occur under these processing conditions, despite many researchers concluding that DRX does not take place in the $\alpha + \beta$ region [50–53].

Seshacharyulu et al. suggested that the globurisation (discussed later on page 47) occurring in the lamellar starting microstructure of Ti-6Al-4V undergoing hot deformation can be regarded as a type of dynamic recrystallisation, whereas the same phenomenon was termed "dynamic globurisation" by Park et al. [54]. This suggests that different understandings, interpretations and definitions of the phenomenon itself is at least somewhat responsible for the opposing views in the literature as to whether or not DRX occurs in Ti-6Al-4V when processed in the $\alpha + \beta$ temperature region and renders the process somewhat of an enigma.

In contrast to the lack of consensus regarding DRX when deformed $\alpha + \beta$ temperature, when Ti-6Al-4V is processed in the single β phase region, many researchers have concluded that DRX is in effect [51, 52, 55].

2.5.2 Hot Deformation of Ti-6Al-4V

The industrial importance of titanium alloys and in particular Ti-6Al-4V has lead to extensive research into the behaviour of this alloy under TMP [56]. Great attention in the scientific literature has been given to the deformation of Ti-6Al-4V under conditions similar to those encountered in industrial forging, rolling and other metal working operations. These include temperatures from below 400 $^\circ$ C [57] well into the β single phase region [51] and strain rates from 4.2 x $10^{-5}s^{-1}$ [49] up to 7000 s^{-1} using a Hopkinson bar [58].

In figure 2.39 on the next page, stress-strain curves can be seen at various relevant temperatures and strain rates. These curves are typical of a specimen with a lamellar starting microstructure and agree with similar work done by other researchers [52, 53, 55, 56].

Figure 2.39 shows that in the $\alpha + \beta$ region, the flow curves are characterised by continuous flow softening after a peak stress and it has furthermore been noted that this flow softening is accentuated by increasing strain rates [52, 55]. It too has been shown, and is evident in figure 2.39 d) and e), that when deformation is carried out at or above the β transus temperature, the flow stress remains almost constant, indicating steady state flow behaviour [51, 55].

It is also clearly seen from figure 2.39 that the flow stress decreases with increasing temperature and increases with increasing strain rate. As is discussed in the next section (2.5.3): it has been shown that the flow softening, evident in figure 2.39 is influenced by the starting microstructure of the alloy. However, Nemat-Nasser et al. [58] has shown that regardless of the starting microstructure, the dependence of flow stress on temperature and strain rate, as described above, remains valid.

2.5.3 Flow Softening Mechanisms

The scientific literature attributes flow softening during the deformation of Ti-6Al-4V in the $\alpha + \beta$ temperature region invariably to one or more of the following three mechanisms: softening by adiabatic heating; softening by localised shear (adiabatic shear bands); softening by globurisation.

The stress-strain curves shown in figure figure 2.39 are typical for material with a lamellar starting microstructure. These curves show pronounced flow softening, a characteristic of a lamellar starting microstructure [55]. This in part is due to the fact that that the flow softening caused by globurisation, described as the “major microstructural phenomenon” responsible for flow softening [52], is active only in materials of a lamellar starting structure

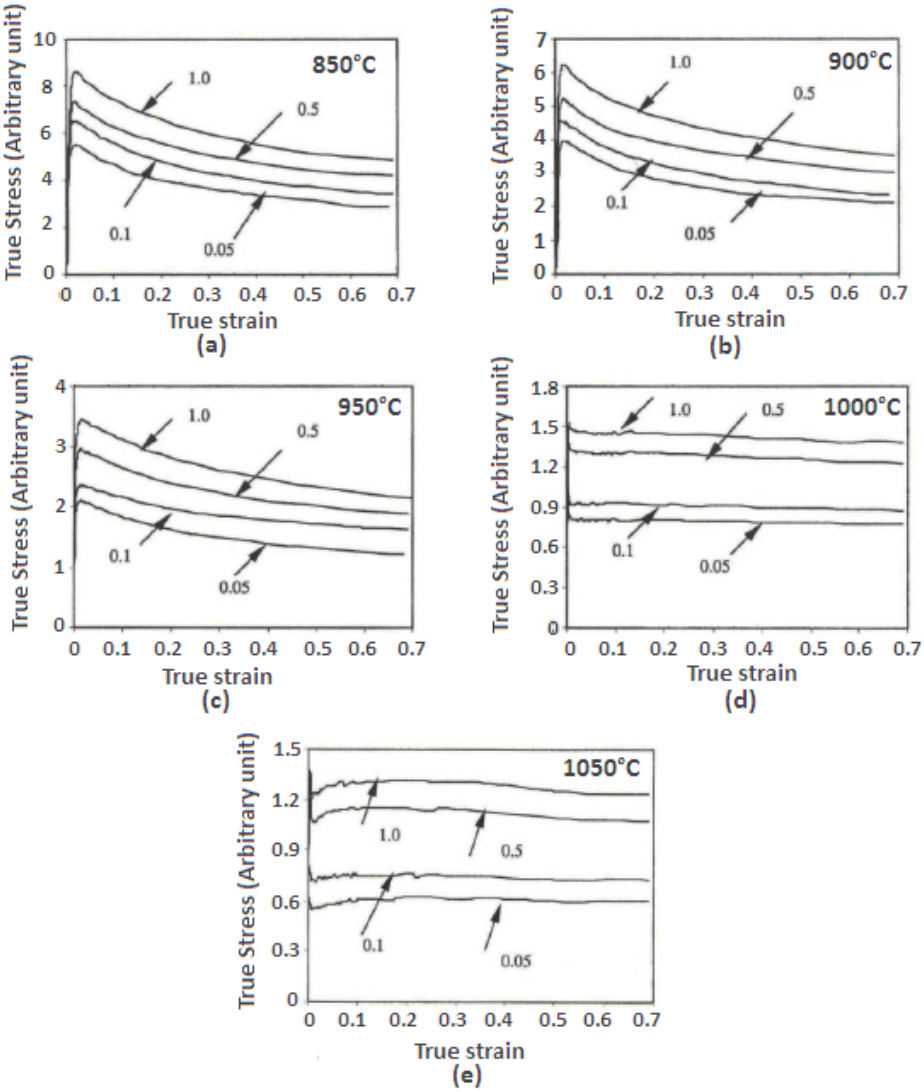

Figure 2.39 – Flow stress - true strain curves for the hot deformation of Ti-6Al-4V with a lamellae starting microstructure at various temperatures and strain rates: (a) 850 ˚C; (b) 900 ˚C; (c) 950 ˚C; (d) 1000 ˚C; (e) 1050 ˚C. Strain rates are shown on the graphs using arrows. Adapted from [51].

and hence is absent in other morphologies such as an equiaxed microstructure. As such, a Ti-6Al-4V specimen of equiaxed starting microstructure does not undergo the pronounced flow softening evident in figure 2.39 [53,55,59] and in fact has been shown to undergo slight work hardening during hot deformation [57,60]. The three flow softening mechanisms are briefly discussed here.

Softening by Adiabatic Heating

Many researchers [51, 53, 56] have suggested that the flow softening encountered when deforming Ti-6Al-4V in the $\alpha + \beta$ region is as a result of adiabatic heating. Nemat-Nasser et al. [58] explain that titanium alloys have a low (although increasing with temperature) thermal conductivity which results in the heat generated during deformation not being dispersed, which as a result increases the temperature of the material as well as promoting

$\alpha \rightarrow \beta$ transformation. Both of which will result in lowering the flow stress. The observation that the flow softening becomes more exaggerated at higher strain rates supports this theory, as at higher strain rates there is less time for the generated heat to be dispersed and conditions move towards being perfectly adiabatic. At an extreme, adiabatic heating can result in locally reducing the flow stress and the creation of localised shear (adiabatic shear bands) [50].

Adiabatic Shear Bands

Studies [55, 56, 58, 61] exploring the parameters for the TMP of Ti-6Al-4V have encountered failure or near failure because of adiabatic shear bands. When deformed at low temperatures (within the $\alpha + \beta$ region) and at high strain rates, Ti-6Al-4V undergoes highly localised shear (due to the effects of adiabatic heating) which manifests itself as shear bands [58]. This shearbanding will ultimately lead to failure and is considered very undesirable in the industrial processing of Ti-6Al-4V.

Seshacharyulu at el. [55] identified that at a strain rate of 10^{-1} s^{-1}, a deformation temperature of greater than 800 $^{\circ}$C must be used to avoid shearbanding, with the required temperature to avoid localised shear increasing with increasing strain rate. This localised shear has been proposed as contributing to flow softening during deformation in the $\alpha + \beta$ region [11].

Work done by da Silva and Ramesh [62] on the compression of both PM TI-6Al-4V (8% porosity) and conventional IM material at room temperature showed localized shear occurring within the IM material when deformed to 8-10%, whereas the porous material underwent homogenous deformation up to the maximum strain tested of 30% without any sign of localised shear. This stability is attributed to the hardening mechanism afforded the PM material by the progressive compaction of the pores with increasing compressive strain.

Figures 2.40, 2.41 and 2.42 on the facing page show: "lamellar kinking", which is a precursor to shearbanding; fully developed adiabatic shear bands; and the ultimate failure that can result from these shearbands respectively.

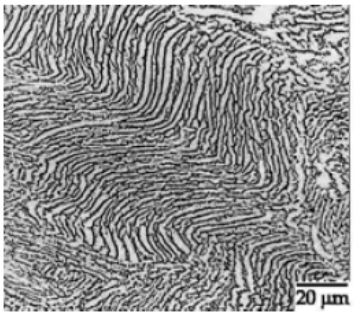

Figure 2.40 – Lamellar kinking shown in the microstructure of Ti-6Al-4V deformed at 950 $^{\circ}$C and a strain rate of 10^{-1} s^{-1}. The compression axis is vertical [55].

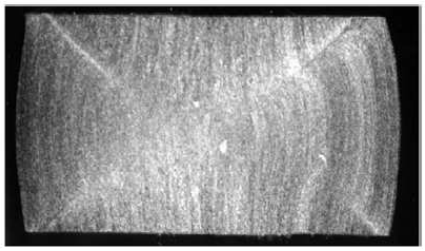

Figure 2.41 – Adiabatic shear bands developed within Ti-6Al-4V, deformed at 730 ˚C and a strain rate of 2000 s^{-1}. Compression axis is vertical [58].

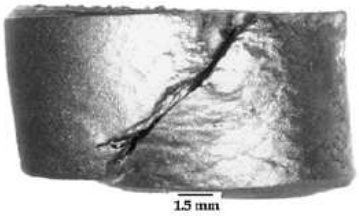

Figure 2.42 – Gross failure of Ti-6Al-4V deformed at 750 ˚C at a strain rate of 10 s^{-1}. The compression axis is vertical [55].

Softening by Globurisation

The process of α lamellae globurisation in a colony microstructure has been accredited with contributing towards flow softening during TMP within the α + β region [49, 52, 53]. With Momeni and Abbasi [52] describing it as the "major microstructural phenomenon" responsible for flow softening. The process of globurisation involves the decomposition of individual α lamellae into several smaller globular α grains and occurs increasingly with increasing deformation [49]. Ding et al. [51] proposed that the breakup of the large aspect ratio α lamellae is as a result of both low and high angle boundaries forming within the platelet, as a result of the deformation or even localised shear, with misorientation ranging from a couple degrees up to 30 degrees. It is proposed that the β phase can penetrate into the α lamellae along these misorientations, and the separation of the α platelet occurs readily, provided the lamellae are not too thick. This explanation for the mechanism of globurisation is the same as those offered in [63] and [54] and is shown schematically by the 4 steps in figure 2.43 on the next page. Step a in figure 2.43 shows shearing in an individual lamellae as a result of deformation. This step is said to occur initially in colonies which are favourably aligned with respect to the induced shear and will spread to other colonies with increasing strain. Step b shows the generation of dislocations of both signs along the shear lines. Step c shows the annihilation of opposite sign dislocations on intersecting slip lines to create an interface of same sign dislocations along a shear line. Step d finally shows the migration of interfaces by diffusion driven by the minimisation of surface energy to create equiaxed globules from the lamellae. The work done in [54] termed this mechanism "dynamic globurisation" and it is shown by way of an EBSD orientation map in figure 2.44 on the following page .

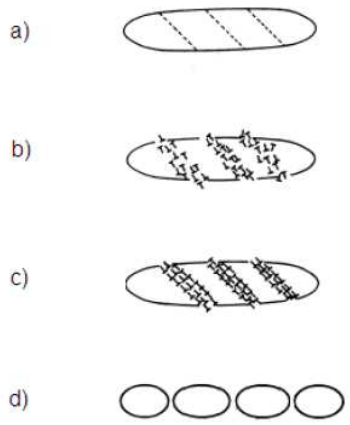

Figure 2.43 – Schematic illustration of the steps involved in globurisation of an individual a lamellae. Adapted from [63].

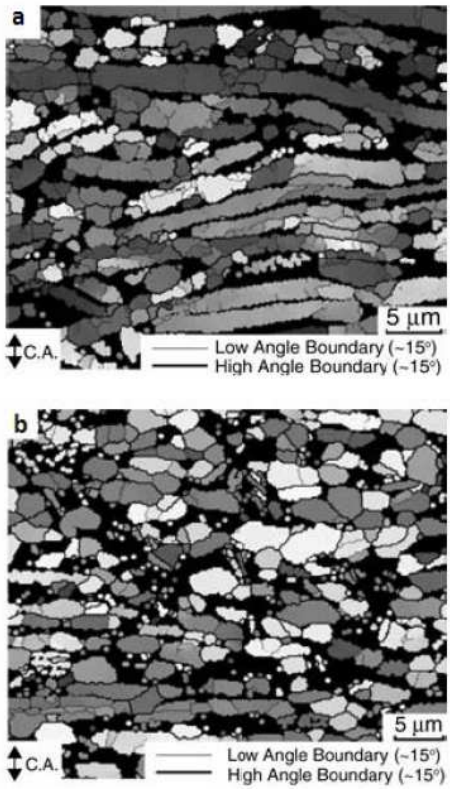

Figure 2.44 – EBSD orientation map showing the breakup of a platelets into globular grains when defored at 900 ° C to (a) 55% and (b) 75% at 4.2 x 10^{-3} s^{-1}. The direction of the compression axis, as shown by the arrows is vertical [49].

2.5.4 Deformation of Ti-6Al-4V in the β Single Phase Region

Majorell et al. [57], when comparing the deformation of Ti-6Al-4V in the α and β phases, state that "the flow mechanisms and kinetics are different in the two phases. This renders a large number of deformation mechanisms responsible for the macroscopic behaviour of the alloy".

As can be seen in figure 2.39 on page 45, that once the β-transus temperature has been passed, the stress-strain curve suggests that steady state flow takes places in this high

temperature region. This almost constant flow stress suggests that DRC and DRX were in operation [51]. The small oscillations in flow stress in the β phase region seen in figure 2.39 d and e and more evident in the works of Momeni and Abbasi [52] and Bruschi et al. [56] can likely also be attributed to the occurrence of DRX in the β phase [52]. Seshacharyulu et al. [55] have also concluded that DRX is in operation during the deformation of Ti-6Al-4V in the β phase region.

In addition to the constant flow stress at temperatures above that of the β-transus, tests on Ti-6Al-4V at various temperatures and strain rates have found that: while at all temperatures the flow stress increases with increasing strain rate, at all strain rates the flow stress becomes temperature insensitive at temperatures above the β-transus (around 1000 ° C). These findings are shown graphically in figure 2.45 which shows the average flow stress for strains of 5 to 50%. The temperature sensitivity at temperatures below the transus temperature is also evident [57].

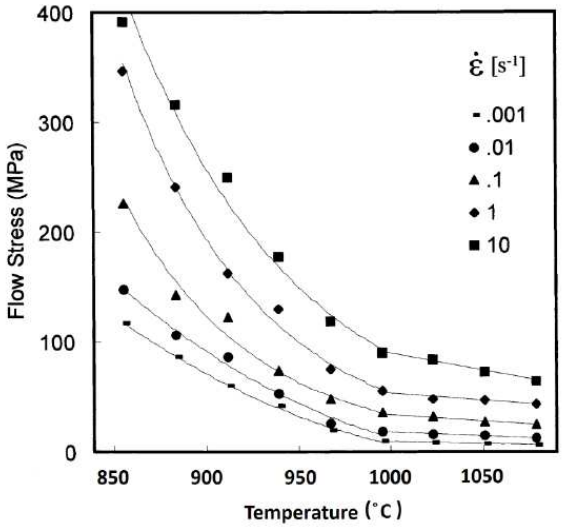

Figure 2.45 – Average flow stress vs Temperature graph showing the temperature insensitivity of the flow stress in the β phase region. Adapted from [57].

2.5.5 Deformation Twinning

Deformation Twinning in Titanium

The HCP structure of pure titanium has a c/a ratio of 1.587 – less than ideal from a deformation perspective. Within the HCP structure, at low temperatures, prismatic glide of a-type dislocations is the most favourable slip system by which deformation occurs. Basal slip and pyramidal slip of a-type Burgers vectors are also active at low temperature. This gives four independent slip systems. To undergo an arbitrary imposed plastic strain however, a polycrystalline material must be able to slip on five independent systems. For this reason it is necessary for titanium to undergo either <c + a> pyramidal slip or deformation twinning when being plastically deformed [64]. Deformation twinning has

been widely reported in high purity titanium with an equiaxed microstructure deformed at room temperature [64–68].

Salem et al. [64], conducting uniaxial compression on titanium, found that mechanical twinning was most prevalent at low strains and that by a true plastic strain of 0.2, those grains undergoing deformation twinning were saturated with twins preventing any further twinning taking place.

Zhong et al. [65] also showed that twinning is most prevalent at "low to medium" deformations and that after 40% reduction by rolling, twinning was strongly depressed due to the drastically refined grain size as a result of the previous twinning and that further deformation was accommodated by slip. It was also shown that twinning will preferentially happen in certain parent grains as a result of their orientation. As a result, a heterogeneous microstructure can result and comprise of large grains that haven't undergone twinning and greatly refined grains occurring as a result of twinning in other more favourably oriented grains [65, 66].

Paton and Backofen [69] studied the influence of temperature on twinning. Their research involved growing titanium single crystals and loading them in various orientations at increasing temperatures. They observed various twinning for temperatures up to 500 $^\circ$C, but at higher temperatures deformation was accommodated by prism slip. It was concluded that <c + a> slip must be very important to the deformation of polycrystalline titanium at elevated temperatures.

It has been concluded that the presence of alloying and interstitial elements (impurities) suppress twinning in titanium [68, 70]. Zaefferer [70] conducted experiments on titanium with two different oxygen concentrations and found that twinning as a deformation mechanism was present for the low oxygen specimens (Ti + 1000 ppm O) but absent in those with a high oxygen content (Ti + 2000 ppm O).

Williams et al. [71] working with single Ti-Al crystals of differing Al content comprehensively showed that increasing Al content and temperature both suppress twinning and promote <c + a> slip as a deformation mechanism.

Deformation Twinning in Ti-6Al-4V

Despite the aforementioned phenomenon of alloying elements and in particular aluminium suppressing twinning in titanium, there have been a number of works reporting deformation twinning in Ti-6Al-4V under certain loading conditions.

Prakash et al. [72] summarised in their review of the literature prior to 2010 that deformation twinning in Ti-6Al-4V had only been reported for very high strain rates (exceeding 1000 S^{-1}) or under cryogenic loading temperatures. Their own work however reported twinning occurring during uniaxial deformation at room temperature at a strain rate of 10^{-6} S^{-1}. Subsequently Coghe et al. [73] have reported twinning in Ti-6Al-4V under uni-

axial deformation at both quasi-static and dynamic strain rates, finding it to be more prevalent at dynamic rates of deformation.

To the knowledge of the author of this work the only published literature identifying deformation twinning in Ti-6Al-4V at elevated temperatures was produced by Yapici et al. [74] and involved several passes of equal channel angular extrusion (ECAE) of billets heated to 800 ˚ C prior to each pass. The ECAE produces simple shear at an approximate equivalent strain rate of 1 S^{-1}.

2.6 Thermomechanical Processing of Powder Metallurgy Ti-6Al-4V

Although no published literature has been found by the author of this work on a comparison of the hot deformation of wrought and PM TI-6Al-4V it is evident from a comparison of the hot deformation curves at similar temperatures for wrought material [53,55,59] and for PM material [75] that the deformation of PM Ti-6Al-4V is characterised by considerable strain hardening as compared to conventional IM material. This strain hardening of PM material undergoing hot deformation is shown in figure 2.46 for "dense" TI-6Al-4V compacts created by HIPing PA powder. da Silva and Ramesh [62] conducted research

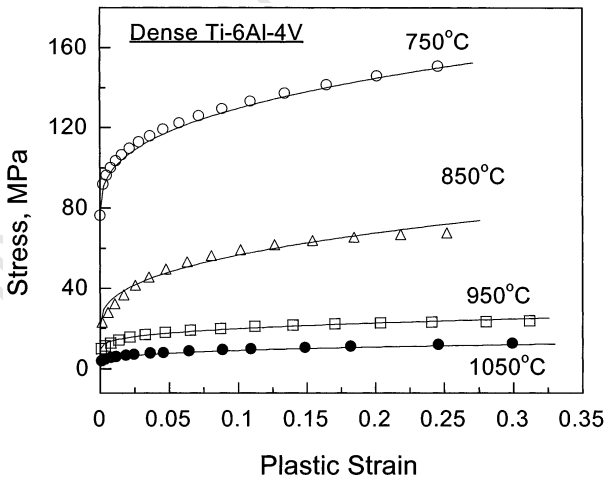

Figure 2.46 – Stress-strain curves for the hot deformation of PA PM Ti-6Al-4V compacts at various temperatures [75].

into the deformation behaviour of porous and fully dense PA PM Ti-6Al-4V compacts at room temperature and showed that the porous material underwent more pronounced strain hardening than the fully dense samples and this was attributed to hardening resulting from pore compaction during deformation of the porous material. This is shown in figure 2.47 on the next page. Kim et al. [76] similarly observed an increased strain hardening for a porous specimen as compared to a dense one.

Kim et al. [76] subjected sintered PA powder compacts to hot upset tests to 40% height reduction at temperatures of 850 ˚ C, 950 ˚ C and 1050 ˚ C. In doing so the density was

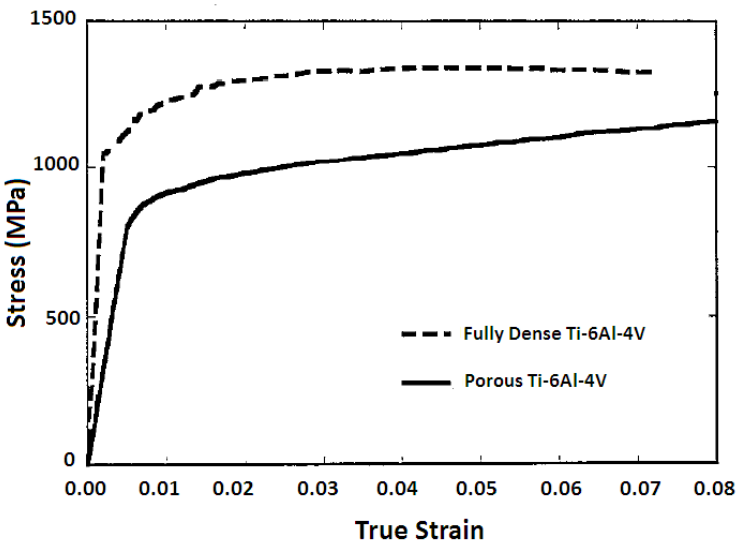

Figure 2.47 – Comparison of deformation behaviour at room temperature of porous (7.6 vol. % porosity) and fully dense PM Ti-6Al-4V compacts. Adapted from [62].

improved from the as-sintered relative density of 82% to 90% after deformation and the density improvement was not sensitive to the deformation temperature at all.

2.6.1 Thermomechanical Processing of Blended Elemental Ti-6Al-4V

Two research papers were found that subjected BE Ti-6Al-4V to TMP and considered it's affect on the density and mechanical properties. These papers are briefly discussed here.

Lee et al.

Lee at al. [77] performed work on the TMP of BE Ti-6Al-4V compacts. The material used in the study was blended from titanium sponge fines and an Al-V master alloy powder and was sintered to a relative density of 98.8%. The TMP was carried out at 800 ˚C and in 3 cross-rolling passes to a combined strain of 0.54. Following the TMP, the samples were quenched and underwent one of 3 different heat treatments: 800 ˚C for 1 hour to create an equiaxed microstructure; 960 ˚C for 30min to create a bi-modal microstructure; and 1000 ˚C for 15min to create a lamellar structure. The samples were again quenched after the heat treatments and subsequently aged for 24 hours at 500 ˚C, after which mechanical test specimens were machined from the material.

Results and Findings: The relative density after the deformation was measured to have risen to 99.2% and no further increase in density was observed after any of the 3 heat treatments, leading to the conclusion that it was primarily the mechanical deformation responsible for healing the macro pores, rather than the thermal treatment. The heat

treatments were not successful in creating the desired microstructures as the temperatures used were as per IM material and did not take into account the increase in β-transus temperature as a result of the elevated impurity content in BE material.

The yield and ultimate tensile strengths of all the material having undergone TMP improved as compared to the as-sintered material by a minimum of 15%. Although a strength difference of up to 9% was observed across the 3 different microstructures, drawing any conclusions on the effects of the different microstructures was hampered by the fact that the microstructures were not properly formed as previously explained. One clear trend however was a decreasing elongation with increasing lamellar portion of the microstructure.

Despite the improved tensile properties following the TMP, the fracture toughness of the material was seen to decrease by between 17% and 27% from the as-sintered condition for the three different heat treatment conditions.

The improved density, altered microstructure and aging treatments were all considered to have contributed to the altered mechanical properties resulting from the TMP, and therefore it is difficult to isolate the influence of any one of those factors.

Weiss et al.

Weiss et al. [40] conducted research into the isothermal hot forging (IHF) of BE compacts. Two different materials were compared in this research, both BE powders, one using titanium sponge fines (HP) and the other using titanium powder produced by an electrolytic reduction process (EP), the difference being that the EP powder had far lower levels of contaminants - especially chlorine. Samples of both materials were subjected to IHF at 925 ° C to 30% and 68% height reduction and were subsequently furnace cooled

Results and Findings: The result of lower contamination resulted in much larger β grains existing in the EP material at the sintering temperature and therefore a far higher aspect ratio lamellar structure occurred in the as-sintered material. The HP powder sintered to 99% relative density, while the EP sintered to 92%. After undergoing IHF to 30% and 68% height reduction, the HP relative density improved to 99.4% and 99.6% respectively and the EP relative density improved to 99.7% and 99.8% respectively.

The static strengths of both materials increased with deformation (and therefore density). This was accredited to both the improved density and refined microstructure resulting from the deformation.

The high cycle fatigue strength proved more complex. The HP material forged to 68% height reduction showed a slight decrease in fatigue strength as compared to the same material forged to 30% height reduction. This was believed to be a result of circular pores being squashed into elongated pores with sharp edges at the higher deformation and the

resulting stress concentration degrading the fatigue performance. The EP material forged to 68% however showed a drastic improvement in high cycle fatigue strength over that forged to 30% height reduction. This was accredited to the partial recrystallisation of the high aspect ratio structure into a more refined microstructure.

Chapter 3

Experimental Methodology

3.1 General Experimental Methodology

This study comprised two separate TMP sequences of the BE material. The first being the hot uniaxial deformation of cylindrical specimens at different temperatures. The second being the plane strain compression (PSC) of rectangular specimens at deformation temperatures chosen as a result of the findings of the hot uniaxial deformation tests. The general testing methods that are common to both these testing sequences are given in this section.

3.1.1 Material

The BE Ti-6Al-4V material used in this work was blended from separate elemental powders supplied by Alfa Aesar and the details of these powders are given here:

- Direct reduction titanium powder: -200 mesh, 99.5% (metals basis)
- Aluminium powder: -100+325 mesh, 99.5% (metals basis)
- Vanadium powder: -325 mesh, 99.5 % (metals basis)

These elemental powders were blended at Stellenbosch University (South Africa) for a total of 7 minutes.

3.1.2 Density Measurement

The procedure used for measuring the density of impermeable sintered materials is given in detail in Standard 54 of the MPIF standards 2010 edition [78] and is included in the appendix of this work on page 131. The equipment required is shown in figure 3.1. The rig consists of a mass balance, a "bridge", a beaker and a specimen support structure. The

bridge is used to support the beaker above the balance pan and the specimen support is connected to the balance pan. A wire basket, connected to the specimen support, hangs into the water and contains the specimen.

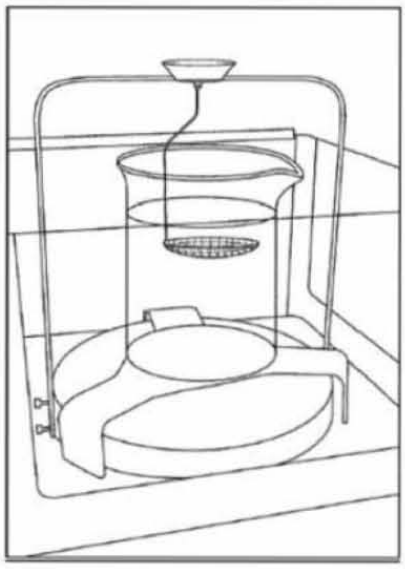

Figure 3.1 – Test rig for density measurement of sintered products. Note the 'bridge' supporting the beaker above the balance pan and the specimen support rig connected to the balance pan [78].

The technique involves taking four measurements: the mass of the test specimen in air (A); the apparent mass of the test specimen and specimen support when suspended in the water (B); the mass of the specimen support in the water without the specimen (C); the temperature of the water during the process. The density of the specimen (D, in g/cm^3) is then given by the following equation:

$$D = \frac{A/\left[A - (B - C)\right]}{\rho_w}$$

Where ρ_w is the density of water at the measured temperature in g/cm^3. 0.07 volume % dish-washing liquid was added to the distilled water to act as a wetting agent. Relative density is calculated as a percentage of the theoretical full density of Ti-6Al-4V and a figure of 4.43 g/cm^{3}is used for this density.

3.1.3 Microstructural Analysis

Grinding and Polishing

Specimens were ground and polished by conventional techniques for Ti-6Al-4V as detailed in table 3.1 on the facing page.

Table 3.1 – Steps for the grinding and polishing used for microscopy specimen preparation.

Step	Grit/Pad	Speed	Force	Time	Lubricant
1	800 SiC	150 rpm	30N	2:00	Water
2	1200 SiC	150 rpm	30N	2:00	Water
3	MD Dac	150 rpm	30N	10:00	9µm diamond suspension
4	MD Chem	150 rpm	30N	10:00	OP-Nap colloidal silica
5	MD Chem	150 rpm	30N	5:00	Water

Microscopy

Both Light Microscopy (LM) and SEM were used to analyse the microstructure of the samples.

Light Microscopy: The specimens for which LM was used to analyse the grain morphology were etched using Kroll's reagent (100ml distilled water, 4ml HNO_3 and 2ml HF) after being polished according to the method detailed in table 3.1. LM was carried out on a Reichert MeF3A inverted light microscope fitted with a Leica DCF 320 camera and Leica DCF acquisition software.

Scanning Electron Microscopy: All specimens for which SEM was used to analyse the microstructure were prepared by the method detailed in table 3.1. The SEM used was an FEI Nano FEGSEM 230. EBSD was employed using this SEM and an Oxford Instruments solid state EBSD detector in tandem with the Oxford HKL Channel 5 Flamenco software package. For EBSD analysis, an 8mm working distance, 166mm detector distance and a 70 $^{\circ}$ pre-tilt specimen stub were employed. An accelerating voltage of 20.0 keV and a spot size of 3.5 was used for all EBSD scans and the step size used varied between 0.05 and 0.3 µm. The majority of EBSD was conducted with a step size of 0.2µm and this is to be assumed unless stated otherwise for a particular map presented in this work. EBSD maps were processed using the Tango mapping program which is part of the Oxford HKL Channel 5 software suite. Maps were "cleaned" by first removing any wild spikes and then implementing noise-reduction which assigned any unindexable point a certain index if that index was shared by at-least 4 of it's neighbors. This noise reduction works on a scale of 1 to 8 neighbors, where at a setting of 1, only a single indexed neighbor is required for an unindexed point to assume that same index and is therefore the most severe noise reduction setting.

When using the Energy Dispersive Spectroscopy (EDS) detector a working distance of 5mm, a spot size of 4.5 and an accelerating voltage of 20.0 keV was used. This same accelerating voltage of 20.0 keV was used when taking BSE images, but a spot size of 3.5 was employed and a working distance of between 5.0mm and 7.0mm was maintained.

3.2 Methodology of Uniaxial Deformation Processing

The first experiments carried out in this work was the TMP by hot uniaxial deformation of sintered cylindrical specimens at various deformation temperatures followed by annealing the specimens. The methodology used for those experiments is detailed here.

3.2.1 Press and Sinter of Cylindrical Specimens

Cylindrical specimens were pressed in a 10mm diameter floating die set to a nominal height of 15mm at a pressure of 375 MPa. The specimen then underwent pressureless sintering for 2 hours at a temperature of 1200 $^{\circ}$C in a vacuum environment of pressures lower than 10^{-5}torr. The heating rate up to the sinter temperature was 300 $^{\circ}$C/hour and the specimen was allowed to furnace cool after the sintering process.

3.2.2 Uniaxial Deformation

Specimen Preparation

Cylindrical specimens were deformed using a Gleeble 3800 thermomechanical simulation system under uniaxial compression conditions using the "ISO-T" cylindrical compression anvils. This system heats by direct resistance heating and monitors the temperature of the specimen by a thermocouple that is percussion welded to the outside of the specimen with both thermocouple wires welded not further than 5 wire diameters away from each other in the same cross sectional plane in the centre of the specimen - midway between contact faces of the cylinder.

In order to achieve a quality weld, the surface where the thermocouples were to be welded was lightly ground by hand using an "Indian stone" to remove any surface contamination and then given a brief rub using 800 grit SiC grinding paper. A welding voltage of 42V was used for the welding process and a ceramic sheath was placed on one of the thermocouple wires to prevent the two wires from touching and creating a short circuit. At temperatures of 1000 $^{\circ}$C and below, a type K (chromel - alumel) thermocouple was used, however at higher temperatures, the type K thermocouples were prone to falling off the samples and as such, for deformation temperatures of 1100 $^{\circ}$C, a type S (platinum - platiunum-rhodium) thermocouple was used.

The ends of the cylindrical specimens were surface ground from their as-sintered state prior to deformation to ensure the parallelism and good surface finish of the two contact faces. In an attempt to alleviate the specimen-anvil friction and prevent welding of the specimen to the compression anvil, graphite paper and 0.10mm thick tantalum foil was used to create a "sandwich" of graphite paper-tantalum foil-graphite paper which was stuck to

the contact faces of the cylindrical deformation specimen using a drop of conductive glue made from equal parts carpet glue and carbon powder.

A cylindrical compression specimen with these sandwiches stuck to the specimen ends and a type K thermocouple welded in place with the ceramic sheath over the red thermocouple wire is shown in figure 3.2.

Figure 3.2 – Photograph showing a cylindrical compression specimen prepared for a uniaxial hot upset test. Note the type K thermocouple welded within 5 wire widths of each other on the same cross-sectional plane midway between the two specimen ends, the ceramic sheath over the red thermocouple wire to prevent the thermocouple wires from touching and the graphite paper-tantalum foil-graphite paper sandwiches on the specimen ends.

Deformation Parameters

Vacuum Atmosphere: The deformations were carried out at high vacuum of greater than 10 x 10^{-4} torr throughout the test to avoid any oxidation. This vacuum was established before any heating of the specimens was started.

Compressive Strain: All of the cylindrical specimens were deformed to half of their original height, resulting in a nominal axial true strain of 0.69.

Strain Rate: All of the cylindrical specimens were deformed at a strain rate of $1s^{-1}$.

Temperature Profiles: Six different deformation temperatures were investigated, namely: 600 ˚ C, 700 ˚ C, 800 ˚ C, 900 ˚ C, 1000 ˚ C and 1100 ˚ C. The heating rate to these temperatures was kept at a constant 4 ˚ C/sec. Once the deformation temperature was obtained, the specimen was maintained at this temperature for a dwell time of 5 minutes to ensure thermal equilibrium throughout the specimen and allow time for microstructural homogeneity, with the exception of the specimen deformed at 1100 ˚ C. At this high temperature, the material had softened to such a degree that the holding force required to ensure good electrical contact between the platen and specimen was sufficient to very

slowly compress the specimen. If a 5 minute dwell was employed at this temperature, this deformation was considerable and as such a dwell time of just 20 seconds was employed for the specimen deformed at 1100 ˚ C. While deformation was underway, a temperature spike as a result of adiabatic heating was observed that raised the temperature by a maximum of around 50 ˚ C for the sample deformed at 600 ˚ C and 700 ˚ C. This adiabatic temperature spike decreased with increasing deformation temperature and was less than 1 ˚ C at a deformation temperature of 1100 ˚ C.

Following deformation the specimen was air-quenched. The cooling rates for the specimens deformed at 1100 ˚ C and 1000 ˚ C were identified at a temperature of 900 ˚ C (in accordance with how the cooling rate was defined in the work of Ahmed and Rack [15] whose findings were presented in figure 2.7 on page 14) and were between 100 ˚ C/s and 120 ˚ C/s. For the lower deformation temperatures, the cooling rate was calculated at a temperature 100 ˚ C below the deformation temperature and was in all cases between 70 ˚ C/s and 96 ˚ C/s.

A graphical representation of this TMP program is given in figure 3.3

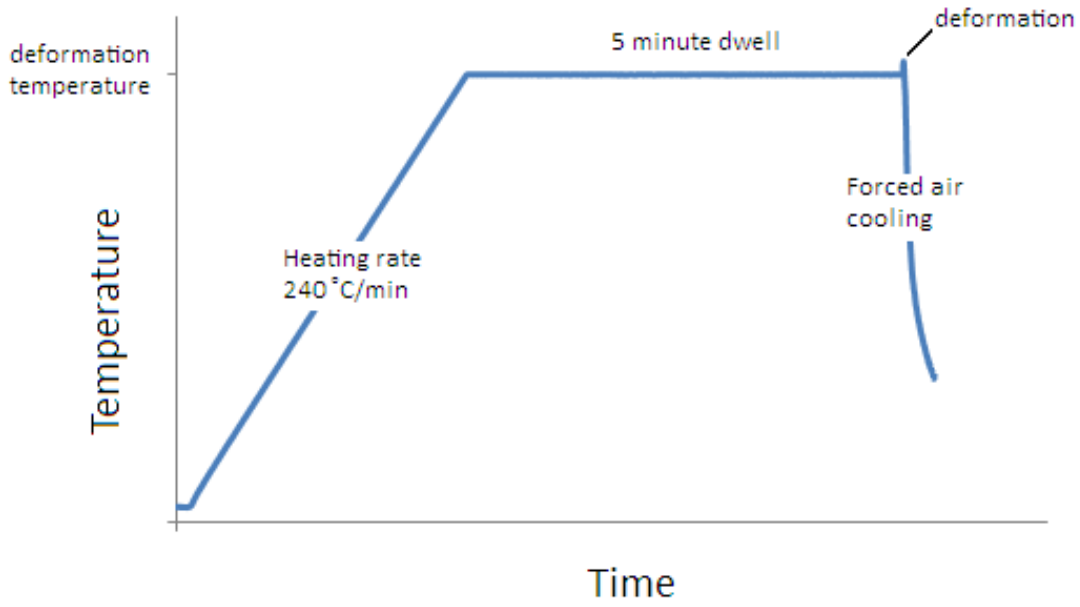

Figure 3.3 – Graphical representation of the TMP treatment used for the hot uniaxial deformation of the cylindrical specimens.

The instructions input to the "Quicksim" program which is used to control the Gleeble in order to achieve this thermomechanical process are shown in figure 3.4 on the next page for a deformation temperature of 800 ˚ C.

3.2.3 Annealing Treatment

Following deformation, the samples deformed at all 6 temperatures (600 ˚ C, 700 ˚ C, 800 ˚ C, 900 ˚ C, 1000 ˚ C and 1100 ˚ C) were all annealed. The deformed specimens were

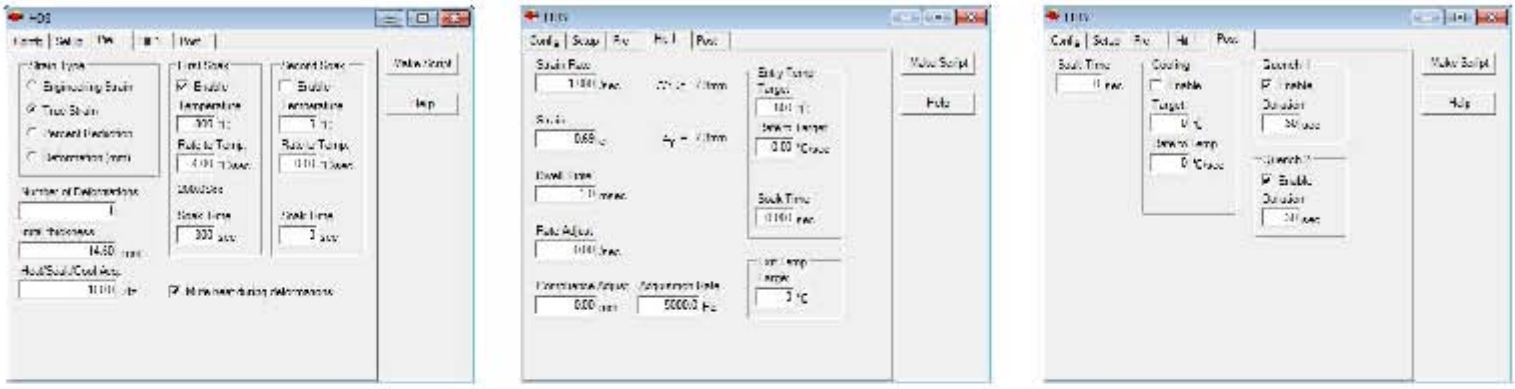

Figure 3.4 – Screen-shots of the thermomechanical process parameters being input to Quicksim for a specimen which is to be heated to 800 ˚C at a rate of 240 ˚C/min, left to soak at that temperature for 5 minutes before being deformed to a strain of 0.69 at a strain rate of $1s^{-1}$ and subsequently air quenched.

annealed to continue, statically, any metadynamic recrystallisation that had initiated during the deformation and subsequent cooling.

The annealing cycle was as follows:

The samples were heated at 5 ˚C/min to 870 ˚C. They were then held at 870 ˚C for 1 hour. The samples were then cooled from 870 ˚C to 600 ˚C at a rate of 3 ˚C/min. From 600 ˚C the samples were allowed to furnace cool to room temperature at a rate greater than 5 ˚C/min. All of this was conducted in a horizontal Elite 12/50/400 furnace, fitted with quartz tube and a vacuum system maintaining a vacuum greater than 5 x 10^{-5} torr.

3.3 Methodology for Plane-Strain-Compression Processing

By considering the results obtained from the uniaxial deformation of the cylindrical specimens at deformations at 600 ˚C, 700 ˚C, 800 ˚C, 900 ˚C, 1000 ˚C and 1100 ˚C the deformation temperatures of 800 ˚C and 1000 ˚C were identified as those TMP processes whose resulting mechanical properties were to be tested. In order to create mechanical test specimens from the TMP processed material, sufficient material would be required. As the 10mm diameter cylindrical specimens deformed in uniaxial compression did not offer sufficient material, the TMP was carried out using a Gleeble 3800 thermomechanical simulation system with plane-strain-compression anvils. The methodology used for those experiments is detailed here.

3.3.1 Press and Sinter of PSC Specimens

PSC deformation requires specimens of rectangular cross-section and as such the pressing of the BE powder for these specimens was carried out using the tooling prescribed in

standard 41 of the MPIF standards (2010 edition) [78] for creating transverse rupture bars (TRB). MPIF standard 41 is given in the appendix on page 128 and details of the TRB tooling is given there. The die cavity is rectangular with dimensions of 31.75mm X 12.70mm and the "thickness" of the specimen is controlled by the amount of powder used. For the creation of the TRB specimens used in this work, the thickness of the green compacts was around 7mm. The press and sinter procedure used for these TRB specimens was kept exactly as that used for the cylindrical specimens, namely: the pressing of the green compact from the BE powder was done at a pressure of 375 MPa and the specimen then underwent pressureless sintering for 2 hours at a temperature of 1200 $^\circ$C in a vacuum environment at pressures lower than 10^{-5} torr. The heating rate up to the sinter temperature was 300 $^\circ$C/hr and the specimen was allowed to furnace cool after the sintering process.

3.3.2 PSC Deformation

Specimen Preparation

TRB specimens were deformed using a Gleeble 3800 thermomechanical simulation system using the "large" PSC anvils. The width of the contact face of these anvils is 10mm and the length (42mm) is comfortably longer than that of the TRB specimen. The thermocouple was percussion welded to the "end" of the TRB specimen, with the two wires in the same plane (parallel to the deformation surfaces) equidistant from each of the specimen's contact faces. The thermocouple wires were welded no greater than 5 wire diameters away from one another.

In order to achieve a quality weld, the surface where the thermocouples were to be welded was lightly ground by hand using an "Indian stone" to remove any surface contamination and then given a brief rub using 800 grit SiC grinding paper. A welding voltage of 42V was used for the welding process and a ceramic sheath was placed on one of the thermocouple wires to prevent the two wires from touching and creating a short circuit. A type K (chromel - alumel) thermocouple was used for both deformation temperatures.

The contact surfaces of the TRB specimens were surface ground prior to deformation to ensure the parallelism and good surface finish of the two contact faces. A single piece of 0.10mm thick tantalum foil was stuck to the contact surfaces of the TRB specimens in an attempt to alleviate the specimen-anvil friction and prevent welding of the specimen to the compression anvil. The foil was stuck to the contact faces of the specimen using a drop of conductive glue made from equal parts carpet glue and carbon powder.

A TRB specimen prepared for PSC with the tantalum foil stuck to the contact surfaces and a type K thermocouple welded in place with the ceramic sheath over the yellow thermocouple wire is shown in figure 3.5 on the facing page.

Figure 3.5 – Photograph showing a TRB specimen prepared for PSC deformation. Note the type K thermocouple welded within 5 wire widths of each other on the same plane midway between the two contact surfaces, the ceramic sheath over the yellow thermocouple wire to prevent the thermocouple wires from touching and the tantalum foil on the contact surfaces of the specimen.

Deformation Parameters

Vacuum Atmosphere: The deformations were carried out at high vacuum of greater than 10 x 10^{-4} torr throughout the test to avoid any oxidation. This vacuum was established before any heating of the specimens was started.

Compressive Strain: The TRB specimens were deformed to a true strain of 0.69 in PSC.

Strain Rate: The PSC deformation was carried out at a strain rate of $1s^{-1}$.

Temperature Profiles: The two different deformation temperatures used for the PSC deformation were 800 ˚ C and 1000 ˚ C. The TMP process was kept as close to that as used for the uniaxial deformation of the cylindrical specimens as possible. The heating rate to the deformation temperatures was kept at a constant 240 ˚ C/min. Once the deformation temperature was obtained, a dwell time of 5 minutes at the deformation temperature was used for the specimens deformed at 800 ˚ C. Persistent heating difficulties and thermocouples falling off during the soak period coupled with a limited supply of specimens, quickly being depleted by such failures led regrettably to varying soak times being used for those specimens deformed at a temperature of 1000 ˚ C. As a result of this one of the specimens deformed at 1000 ˚ C underwent a dwell time of 2 minutes, another 50 seconds and the third only 40 seconds. Despite these varying soak periods, no discernible difference was evident in the microstructures of the three specimens and it is expected that equilibrium and homogeneous microstructures were established within the specimens during all of these soak times as the diffusional kinetics at this temperature are shown to be very rapid.

Following deformation the specimen was air-quenched in the same manner as the cylindrical specimens undergoing uniaxial compression had been.

The instructions input to the "Quicksim" program which is used to control the Gleeble in order to achieve this thermomechanical process were identical to that shown in figure 3.4 on page 61 for the uniaxial deformation, however when measuring the "thickness" of an initial specimen deformed at 800 °C, it was found to have under-deformed by some 0.80mm. This was corrected by inserting a "compliance adjust" value of 0.80mm in the "Hit1" tab shown in figure 3.4. This under-straining was not observed at a deformation temperature of 1000 °C.

Heating of the TRB samples and maintaining an even temperature throughout the specimens using the large PSC anvils proved very troublesome as mentioned above. The difficulties encountered were overcome by systematically increasing the "air-ram" clamping force that the anvils impart on the specimen during heating, improving the contact between the anvils and the specimen, until satisfactory heating and heat distribution was achieved.

3.3.3 Annealing Treatment

Following the PSC, the TRB specimens were annealed in the exact same way as the uniaxially deformed specimens had been: heated at 5 °C/min to 870 °C, held at 870 °C for 1 hour and then cooled from 870 °C to 600 °C at a rate of 3 °C/min. From 600 °C the samples were allowed to furnace cool to room temperature at a rate greater than 5 °C/min. All of this was conducted in a horizontal Elite 12/50/400 furnace, fitted with quartz tube and a vacuum system maintaining a vacuum better than 5 x 10^{-5} torr.

3.4 Mechanical Testing of Material

3.4.1 Three-Point-Bend Tests

In order to evaluate any improvement in mechanical properties resulting from the TMP of the porous as-sintered BE material, mechanical testing of the processed material was required. The limited amount of material available due to the small size of the TRB specimens that underwent PSC made it impossible to conduct standard tensile tests.

The MPIF standard 41 [78] for determining the transverse rupture strength of PM materials, where the tooling for creating the TRB specimens used in this research is detailed, involves breaking these TRB specimens in a three-point-bend arrangement as shown in figure 3.6 on the facing page. The transverse rupture strength is then calculated from the following equation:

$$TRS = \frac{3PL}{2t^2w}$$

Transverse rupture strength is calculated in MPa where P is the breaking force in N, L is the distance between supporting rods (mm), t is the thickness of the TRB (mm) and w

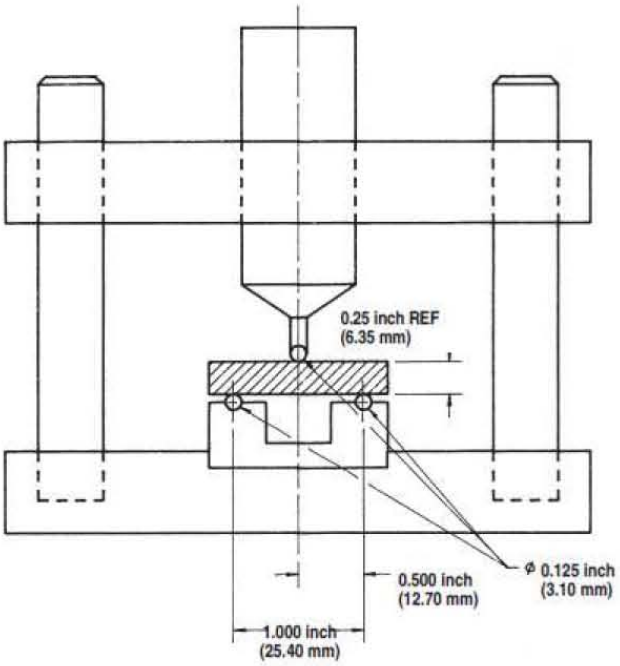

Figure 3.6 – Transverse rupture test fixture used to determine the transverse rupture strength of BE materials by loading them in three-point-bending [78] .

is the width of the TRB (mm). This equation is the stress in the outermost material as calculated by simple bending theory.

The standard states that this test is only applicable for PM material of negligible ductility (presumably so that bending theory is still applicable).

A three-point-bend fixture was created as per this standard and used to evaluate the mechanical properties of the TMP processed material created in this work with an understanding that in the event of noticeable plastic deformations, the tests will only be evaluated in a comparative manner.

Material in the as-sintered condition, TMP processed condition as well as commercial IM material was evaluated using this rig. For all the specimens subjected to this transverse rupture strength evaluation a nominal specimen geometry of width 9.70mm and thickness 2.80mm was used in order to avoid any effects resulting from differing specimen geometries. A pre-load of 20N and a cross-head speed of 2mm/min was employed during testing. A photograph of the three-point-bend rig and test specimen is shown in figure 3.7 on the next page. The testing was carried out on a Zwick 1484 universal testing frame equipped with a 200kN load cell.

Creating the Three-Point-Bend Specimens

A three-point bend specimen needed to be created from the deformed and subsequently annealed TRB specimens. To achieve this the “bulging ends” on either side of the material that was in contact with the PSC platen was machined off until a rectangle was achieved. The sides of this rectangle that were the contact faces during the PSC deformation were

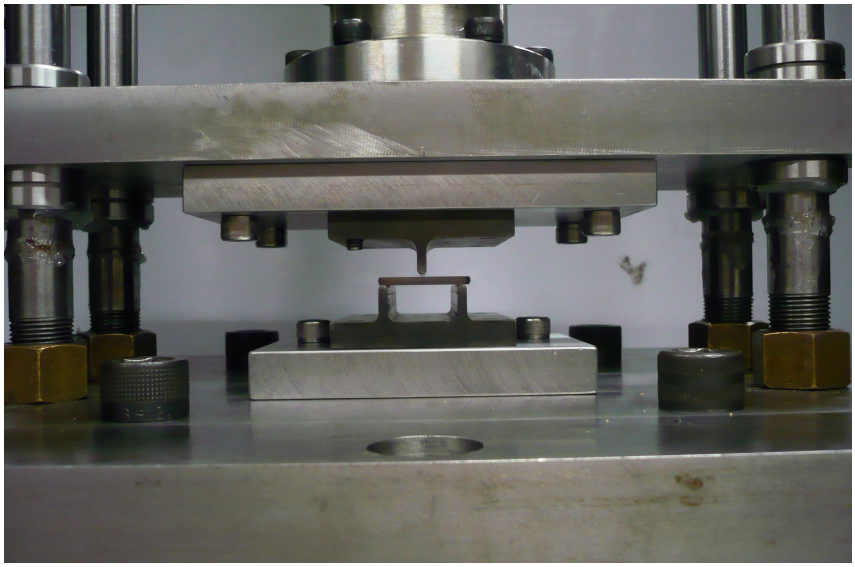

Figure 3.7 – Photograph showing the three-point-bend rig with test specimen in place used to measure the mechanical properties of the material in this study.

surface ground to achieve the three-point-bend specimen nominal thickness of 2.80mm. Care was taken to remove equal material from both of the contact faces in order to remove any material where the deformation was influenced by the specimen-platen interface. The part of the deformed PSC material that was used to create the three-point-bend specimens is shown in figure 3.8.

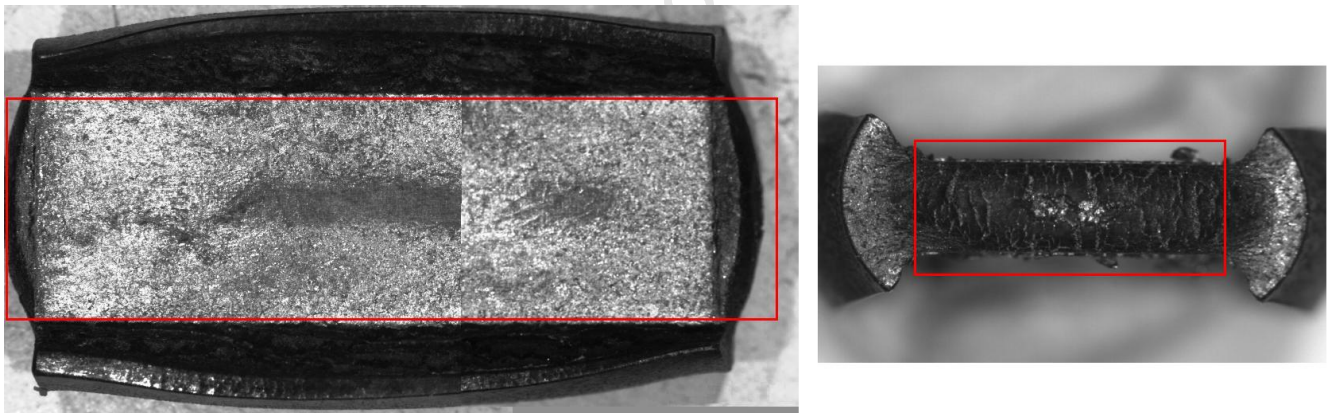

Figure 3.8 – Photograph showing which part of the specimens deformed by PSC was used to create the three-point-bend mechanical test specimens.

3.4.2 Hardness Testing

In addition to the transverse rupture strength evaluations conducted using the three-point-bend rig, hardness measurements were conducted on specimens from each of the four conditions (as-sintered, TMP processed at 800 °C, TMP processed at 1000 °C and the commercial IM material) that underwent the three-point-bend evaluation. Hardness was measured on the Vickers hardness scale by means of a Zwick/Roell ZHV hardness

indenter using a 10kg force which was maintained for 10s as well as at indenting forces of 500g and 100g using a Highwood HWDM3 microhardness tester

11 hardness measurements were taken from each specimen and were conducted across the width of the transverse rupture strength specimens. The material was prepared for these hardness tests by the same grind and polish program used for the microscopy in this work, given in table 3.1 on page 57.

Chapter 4

Results and Discussion of Uniaxial Deformation

4.1 As-Sintered Specimens

4.1.1 Elemental Composition of As-Sintered Material

An EDS scan was used to measure the elemental composition achieved in the sintered material studied in this work. A continuous scan of 120s over a block of 200µm X 200µm was carried out at 11 points evenly spaced along the cylindrical axis of a sectioned specimen as shown in figure 4.1 . As a reference, EDS scans under the exact same conditions

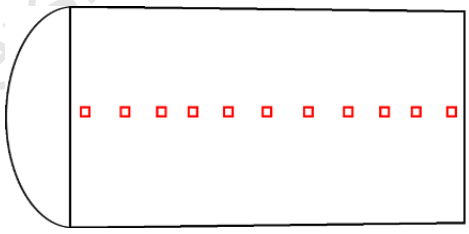

Figure 4.1 – Scan sites for EDS analysis of as-sintered material

were conducted at 11 random sites on a commercial wrought Ti-6Al-4V sample. The elemental indexing was limited to the elements Ti, Al and V. The results of the scans for the as-sintered and wrought materials are shown graphically in figure 4.2 on the next page where the weight percentage of both Al and V are given. In each of these cases Ti will make up the balance of the composition.

As can be seen in figure 4.2 on the following page the vanadium content of the sintered material lies fairly consistently on the 4 weight percent line as desired. It is worth noting however that the vanadium content of the commercial wrought sample measured nearer the 5 wt. % mark for the same test conditions. The aluminium content of the sintered material is consistently lower than both the desired 6 wt. % and the level measured for the wrought sample. It is thought that the fact that the sintering temperatures are almost

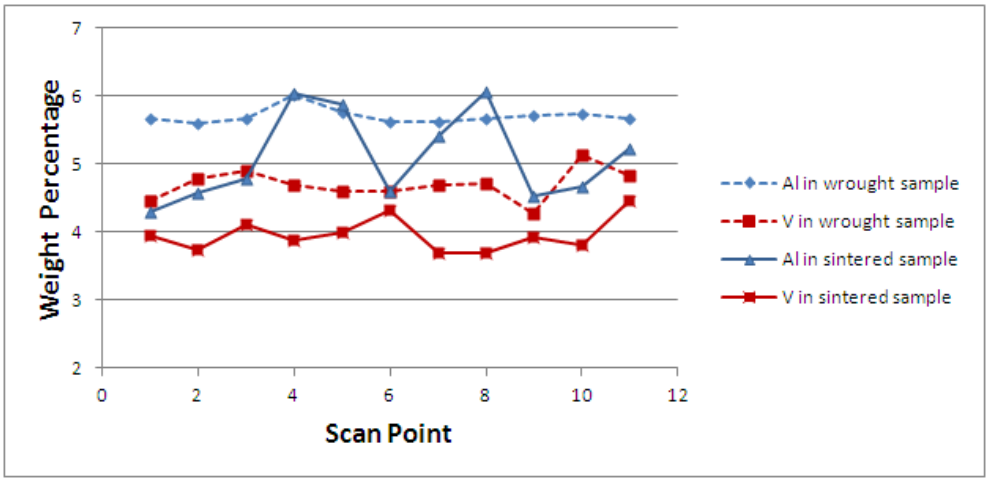

Figure 4.2 – Elemental composition as determined by EDS scans on both as-sintered material and a commercial wrought sample

twice that of the melting temperature of the aluminium powder particles may have led to the decreased content and that the use of a master Al-V alloy powder for future work might rectify this shortcoming.

4.1.2 Porosity and Density of Sintered Specimens

Figure 4.3 shows a low-mag micrograph of an un-etched sintered specimen. The degree, size and distribution of the porosity are clearly seen. This as-sintered material was measured to have a density of 88.0%. As can be seen, the as-sintered specimen exhibits a bi-modal pore size distribution consisting of larger pores (of between 50μm and 120μm) and smaller pores of about 2μm to 17μm.

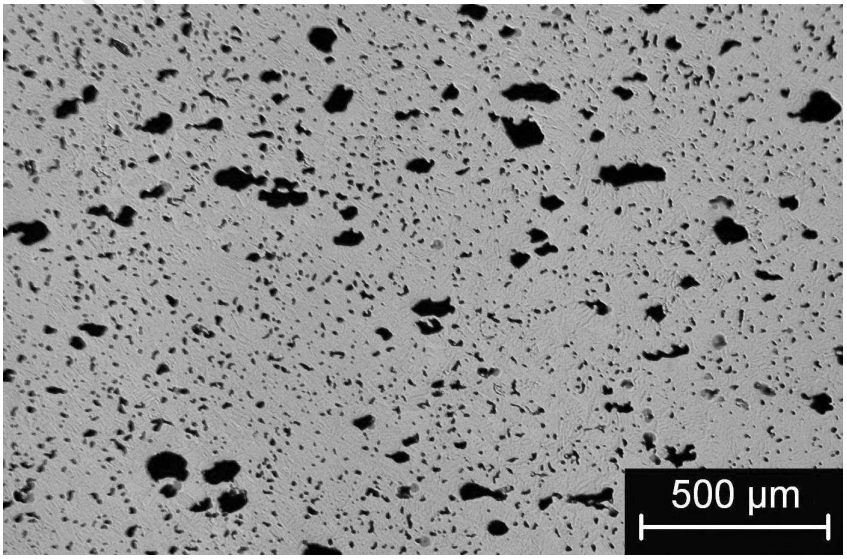

Figure 4.3 – Micrograph showing the porosity in an un-etched as-sintered specimen.

4.1.3 Microstructure of Sintered Specimens

Figure 4.4 shows a micrograph of an as-sintered specimen that has been etched to reveal the grain structure and figure 4.5 shows the results of EBSD conducted upon the as-sintered material by means of a band-contrast map and an Euler colour orientation map. Any β phase that was indexed has been coloured blue on the band-contrast map. Therefore any material not coloured blue on the band-contrast map was either indexed as α or was unable to be indexed. Those points that were not indexed are shown as black in the orientation map.

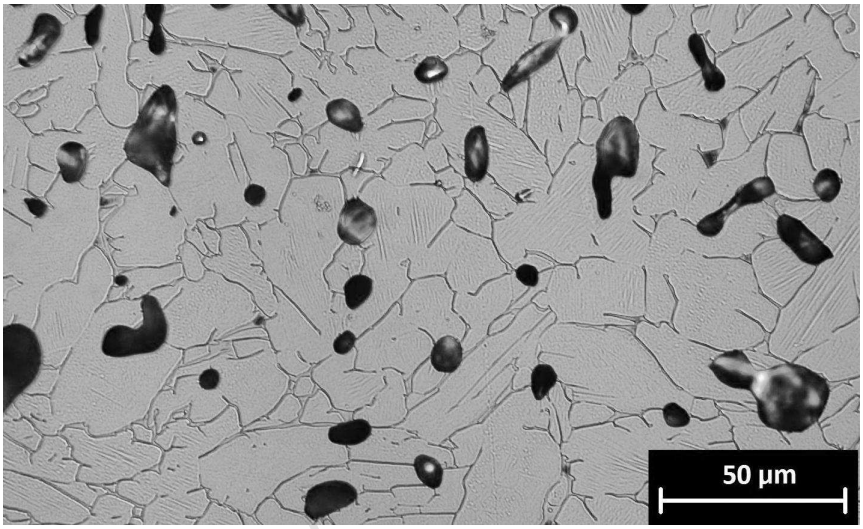

Figure 4.4 – Micrograph of etched as-sintered specimen to reveal the microstructure

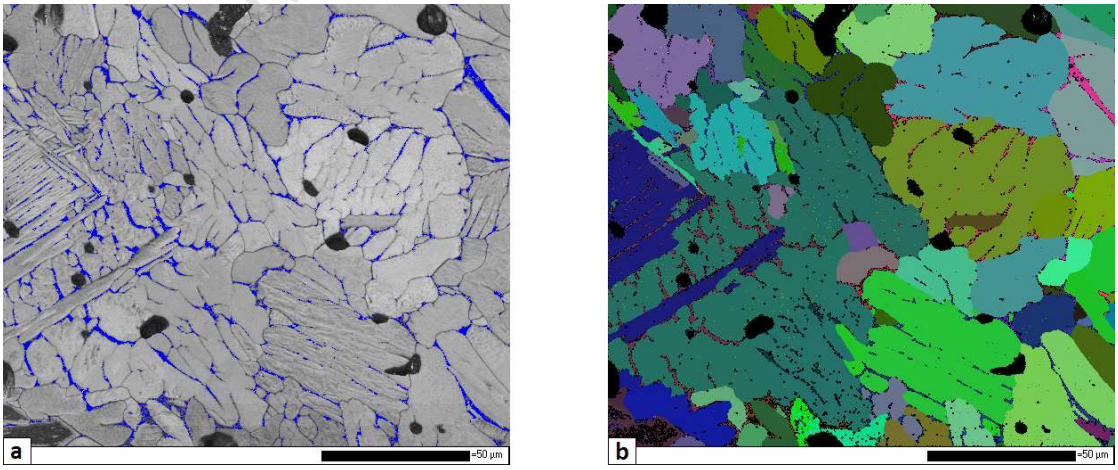

Figure 4.5 – Results of EBSD conducted on an as-sintered specimen shown by means of a) a band-contrast map and b) an Euler colour orientation map. Any β phase indexed has been coloured blue on the band-contrast map. The pores in the sintered material are evident as the black voids where no indexing was possible. A step size of 0.3 µm was used for these maps.

4.1.4 Discussion of As-Sintered Microstructure

The as sintered grain structure was as expected as it very closely resembles the grain structure of BE TI-6Al-4V material created in other studies [35, 39, 40, 77]. Typical of BE material, the aspect ratio of the α lamellae is small in comparison to those resulting from higher purity PA powder due to the size of the β grains existing above the transus temperature being limited by impurities [40].

The density of the as-sintered material is lower and the size of the porosity is greater than those in other work involving BE powder and large pores of between 50µm and 120µm are present. The aluminium powder particles are the largest in the blend (fitting through mesh of 150µm square openings), the next largest being the titanium particles (passing through a mesh of 75µm squared) whereas the vanadium particles are far finer. It is therefore conceivable that these large particles may arrange themselves at certain sites so as to result in these large pores existing in the green compact after die compaction - bearing in mind the relatively low powder compacting pressure of 375MPa. Other considerations are the lower sintering temperature and shorter sintering time used in this study compared to others and the unknown behaviour of the pure aluminium particles heated to these high temperatures - with the sintering temperatures being almost twice that of the melting temperature of aluminium, it is possible that the aluminium particles (if not fully diffused into an alloy by the time the temperature reaches their melting temperature) vaporise to leave behind the large voids.

4.2 Stress-Strain Curves of Uniaxial Deformation

Although barreling was clearly evident in the specimens deformed at all of the investigated temperatures, the barreling coefficient was measured to be just above the 0.9 threshold, below which correction for friction is necessary [42]. Due to this and the fact that the flow stress was not of particular importance in the current work, friction was ignored. The stress was therefore calculated as per the equation for true stress in uniaxial compression, with no correction for friction made. The true stress-true strain curves for the uniaxial deformations carried out at all of the six different deformation temperatures investigated in this work are given in figure 4.6 on the facing page. From these deformation curves, it appears as though the specimens deformed at higher temperatures, specifically 1000 $^\circ$C and 1100 $^\circ$C, undergo less strain than those deformed at the lower temperatures and less than the 0.69 desired. This is as a result of the material softening at these high temperatures to such a degree that they very slowly deform under the clamping force during the soak period, such that less deformation remains to be conducted during the "deformation" step. The results of this is that the final dimensions of the specimen reveal a strain of 0.69, however at the high temperatures of 1000 $^\circ$C and 1100 $^\circ$C, some of this straining was achieved at very slow rates during the soak period.

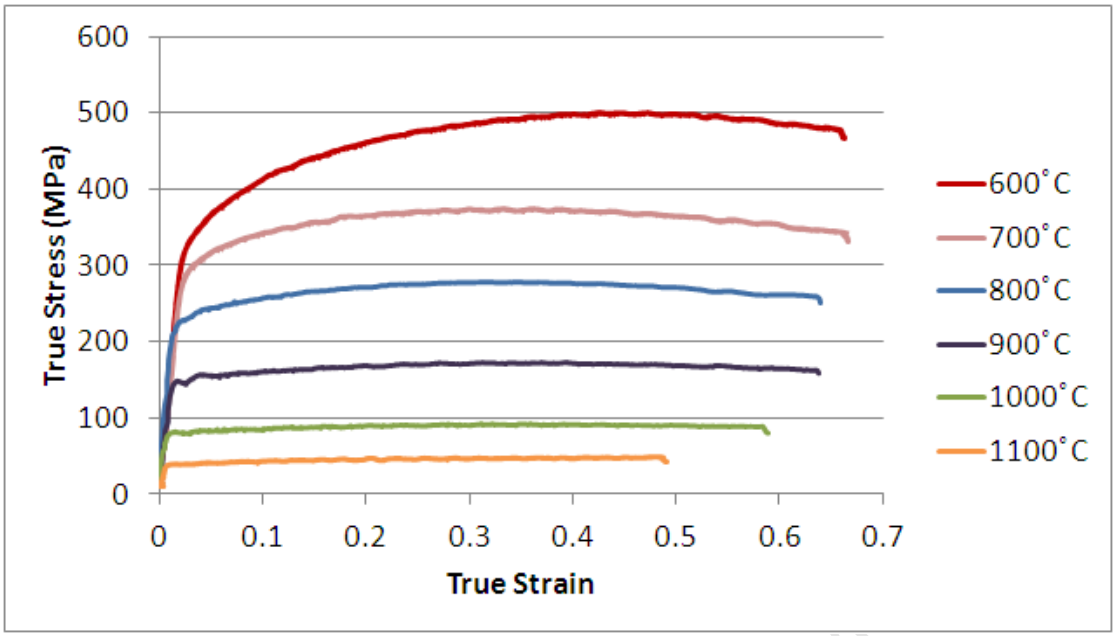

Figure 4.6 – True stress-true strain curves for the uniaxial deformation of sintered cylindrical specimens at elevated temperatures and a strain rate of $1s^{-1}$.

4.2.1 Discussion of Stress-Strain Curves of Uniaxial Deformation

The true stress-true strain curves in figure 4.6 which show the results of the hot uniaxial deformation of the BE compacts clearly shows a decreasing flow stress with increasing deformation temperature which of was course was expected as [58] had shown this to be the case for all starting microstructures of Ti-6Al-4V when undergoing hot deformation. The specimens deformed at 900 ˚ C and below show significant strain hardening. This strain hardening reduces at higher deformation temperatures and the flow stress is almost steady state when deformation takes place at 1100 ˚ C. This again was as expected due to the the microstructure not being of a fine lamellar colony morphology, the BE material was not expected to undergo the pronounced flow softening associated with that microstructure when undergoing hot deformation as described in the literature review on page 44. Both da Silva and Ramesh [62] as well as Kim et al. [76] have also observed greater strain hardening in porous material as compared to “dense” specimens which is considered to contribute considerably to the strain hardening of these as-sintered specimens due to their considerable porosity. Furthermore the steady state flow stress observed at temperatures exceeding 1000 ˚ C has been widely reported and attributed to the rate of restoration mechanisms at this high temperature negating any strain hardening [51, 55].

Note too that none of the flow curves at any of the deformation temperatures studied show the oscillations that other researchers [50, 52, 55] have used as an indication of dynamic recrystallisation taking place (especially in the β single phase region).

4.3 Analysis of Hot Uniaxially Deformed Specimens

4.3.1 Densification and Porosity-gradient in Deformed Specimens

Part a of figure 4.7 shows a macroscopic view of the specimen deformed at 1000 ˚ C. The barreling that occurred is easily seen and the specimens deformed at all of the other temperatures exhibited similar barreling to that shown here. Figure 4.7 b shows a micrograph of a sectional strip taken from the middle of the specimen shown in figure a and has platen-specimen interfaces at the top and bottom of the micrograph. From this micrograph, the extent of the strain concentration at the centre of the cylinder is evident and the amount of pore closure and densification in this strained region is also clearly seen. However the region of the sample near the specimen-platen interface shows little or no densification or pore closure, and porosity similar to that evident in the as-sintered specimen is seen in this region.

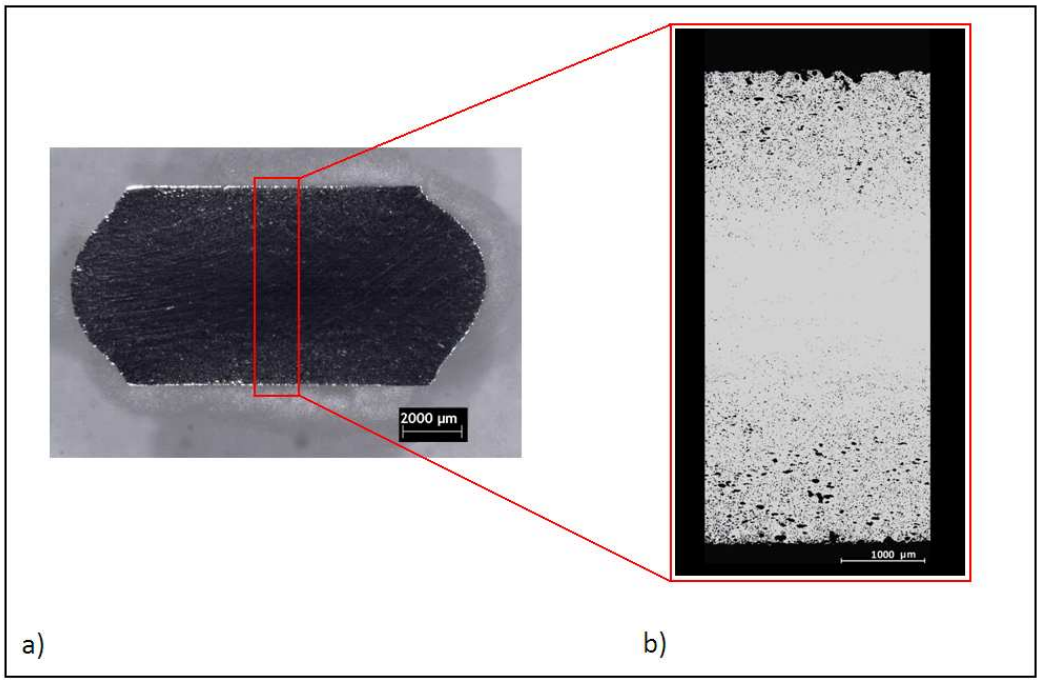

Figure 4.7 – a): Macroscopic section showing the barreling as a result of the hot deformation of the cylindrical specimen deformed at 1000 ˚ C. b): Micrograph of section from the middle of figure a).

Micrographs showing a section from the specimens deformed at all six of the deformation temperatures used in this study are shown in figure 4.8. In this figure the varying "heights" of the deformed specimens are due to differing initial heights of the undeformed specimens.

The specimens deformed at 800 ˚ C, 900 ˚ C and 1000 ˚ C were processed at DSI in New York state whereas those deformed at 600 ˚ C, 700 ˚ C and 1100 ˚ C were processed on a brand new system installed at the University of Cape Town (UCT). As can be seen in

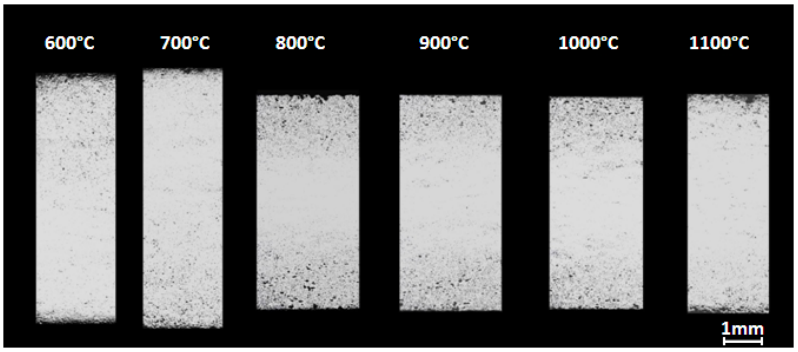

Figure 4.8 – Micrograph sections through the centre of specimens deformed at all six of the deformation temperatures used in this work. Specimen-platen interfaces exist at the top and bottom of each micrograph. The different "heights" of the specimens is due to varying heights of the undeformed specimens and not inconsistent strain.

figure 4.8 and corroborated by a larger barreling coefficient, the strain distribution within those samples deformed at 600 ˚ C, 700 ˚ C and 1100 ˚ C is more uniform throughout the thickness of the specimen as compared to those deformed at DSI. This was deemed to be as a result of the tests run on the system at UCT experiencing less specimen-platen friction as a result of better lubrication from the graphite paper-tantalum foil "sandwich".

The densities measured after the hot deformation at the 6 deformation temperatures were as given in table 4.1.

Table 4.1 – Relative densities of the BE specimens in the as-sintered condition and after uniaxial compression at 600 ˚ C, 700 ˚ C, 800 ˚ C, 900 ˚ C, 1000 ˚ C and 1100 ˚ C

Specimen Condition	Relative Density Measured
As-Sintered	88.0%
Deformed at 600 ˚ C	97.4%
Deformed at 700 ˚ C	97.4%
Deformed at 800 ˚ C	94.0%
Deformed at 900 ˚ C	96.0%
Deformed at 1000 ˚ C	96.0%
Deformed at 1100 ˚ C	97.5%

These densities were measured for the whole specimen and looking at the pore distributions in figure 4.8, one can easily conclude that the density of the porous material near the edges will be lower than the figure stated in table 4.1, and the density of the material in the centre, will be higher than this figure.

There is no apparent relationship between the temperature of deformation and the resulting density, suggesting that the increase in density achieved through the hot deformation of this porous BE preform was as a result of the mechanical deformation and is insensitive to the temperature at which it is conducted, in accordance with the findings of [77].

The relative densities for these specimens was calculated against the theoretical full density of Ti-6Al-4V (4.43 g/cm^3). Due to the observations presented on page 70 of the BE material used in this research not achieving a perfect Ti-6Al-4V composition and impor-

tantly that it is lean in the light element of aluminium, the theoretical full density of this material would be expected to be greater than that value used for Ti-6Al-4V and as a result of this it is likely that the figures presented here (and elsewhere in this work) for density are slightly overestimated. Nonetheless this does not make comparing relative densities of this material after the various processing investigated in this research any less accurate or reliable.

4.3.2 Microscopy of the Highly Deformed Region

The microstructure of the uniaxially deformed specimens were investigated in the centre of the specimens where the strain was concentrated. Light micrographs showing the microstructure in these areas for the samples deformed at 600 ˚ C, 700 ˚ C, 800 ˚ C, 900 ˚ C, 1000 ˚ C and 1100 ˚ C and subsequently force cooled by air quenching are given in figure 4.9 on the next page.

EBSD analysis was conducted to further study the microstructure in the highly strained centre of the deformed specimens. The results of this EBSD analysis are presented here by the band-contrast map generated from the scans and an Euler colour orientation map for each of the deformed specimens. For the deformation temperatures of 600 ˚ C, 700 ˚ C and 800 ˚ C these results are given in figure 4.10 on page 78 where the specimens deformed at 600 ˚ C, 700 ˚ C and 800 ˚ C are shown in figures a-c respectively and the band-contrast maps are denoted by the subscript “1” and the orientation maps by “2”. The same results for those specimens deformed at 900 ˚ C, 1000 ˚ C and 1100 ˚ C are given by parts a-c of figure 4.11 on page 79 respectively where the subscripts are as per the results in figure 4.10 for the lower deformation temperatures. For the band-contrast maps in figures 4.10 and 4.11, all the β phase that was indexed has been coloured blue. Everything that is not blue was either indexed as α or was unable to index. Those points that were unable to index are shown as black in the orientation maps.

SEM micrographs of the as-deformed specimens were obtained in the backscattered electron mode to analyse any elemental partitioning within the microstructure. These BSE micrographs at two different magnifications are given in figure 4.12 on page 80 for the deformation temperatures of 800 ˚ C and 900 ˚ C and in figure 4.13 on page 81 for the deformation temperatures of 1000 ˚ C and 1100 ˚ C.

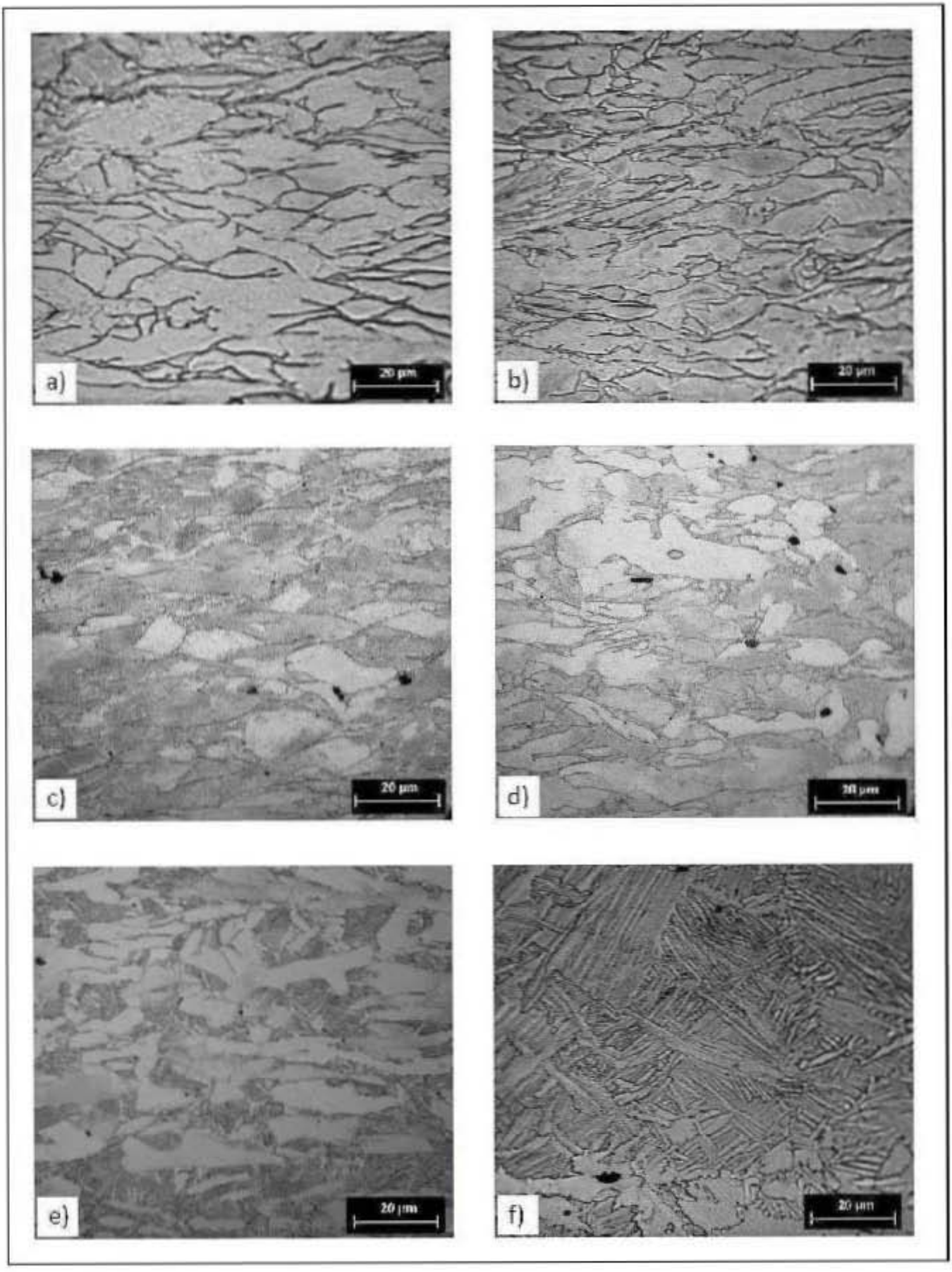

Figure 4.9 – Light micrographs of the as-deformed microstructure in the centre of samples deformed at a) 600 ˚C , b) 700 ˚C, c) 800 ˚C, d) 900 ˚C, e) 1000 ˚C and f) 1100 ˚C and subsequently quenched with air. The compression axis is vertical for all the micrographs.

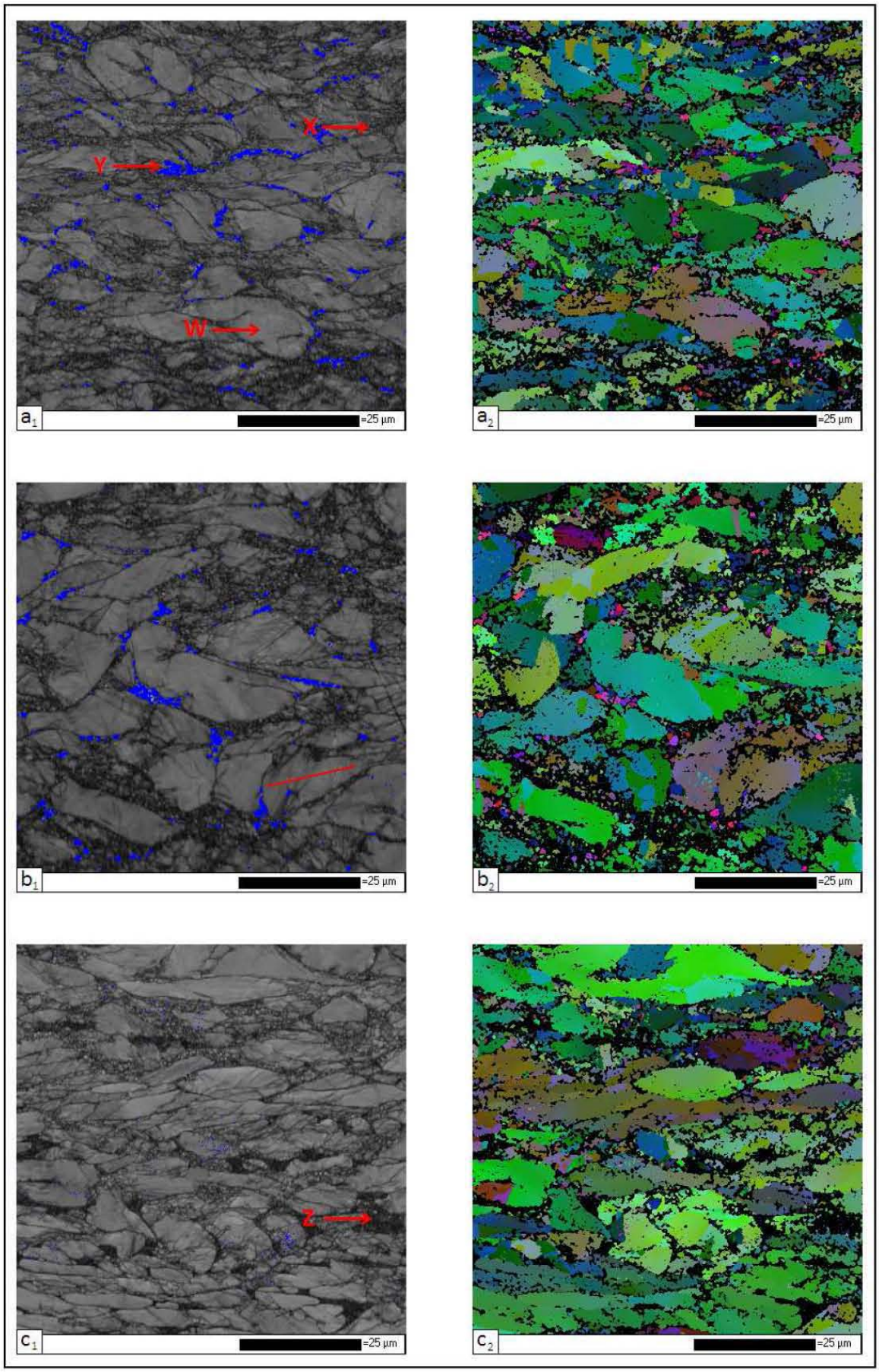

Figure 4.10 – Results of the EBSD analysis of the specimens deformed at 600 ˚ C, 700 ˚ C and 800 ˚ C (a-c respectively) presented by way of a band-contrast map (subscript of "1") and an orientation map (subscript of "2"). Any β phase that was indexed is coloured blue in the band-contrast maps. The line along which the misorientation profile introduced later in figure 4.19 was conducted is drawn in the band-contrast map of b_1. The Compression axis is vertical for all the micrographs.

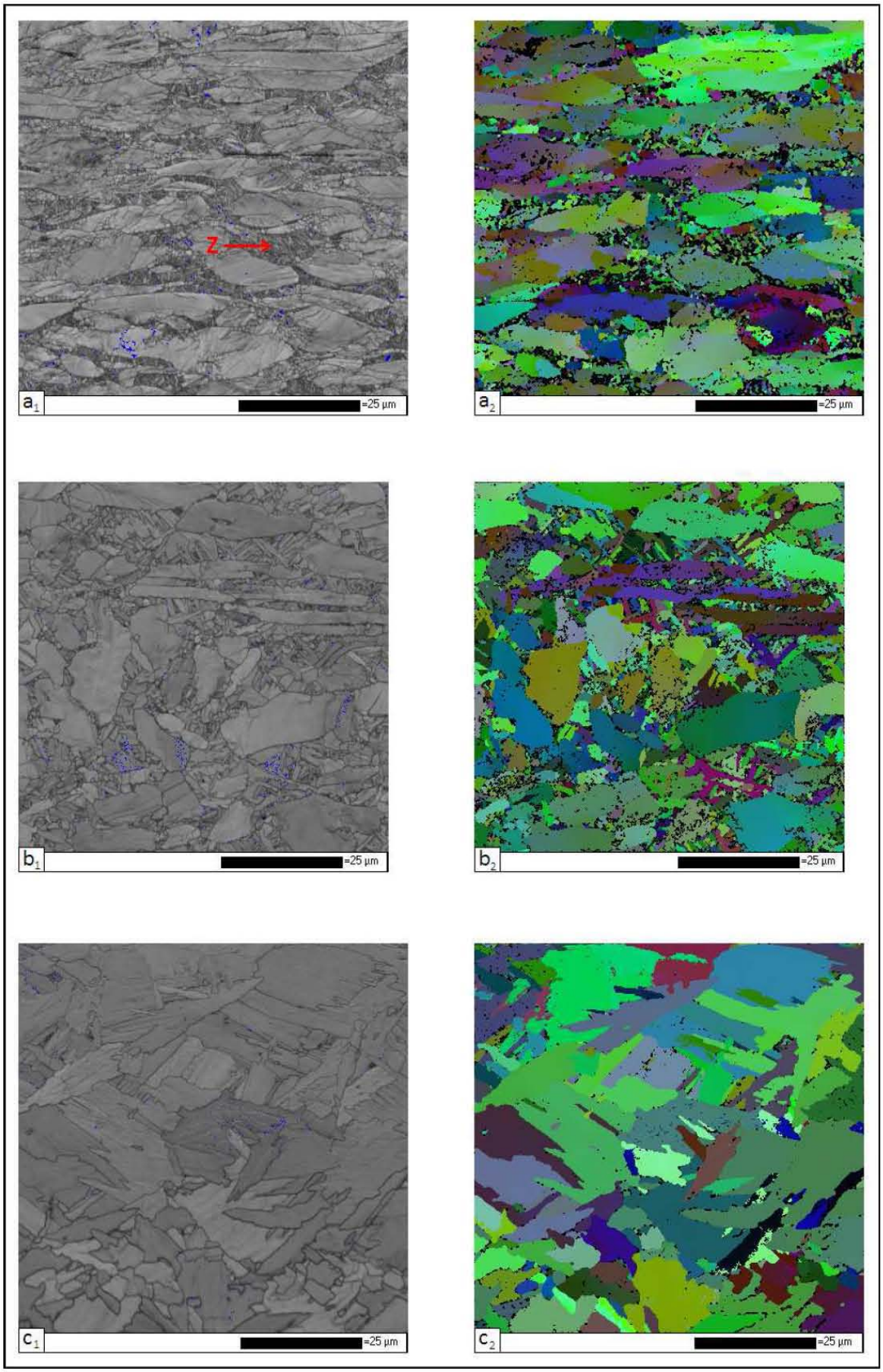

Figure 4.11 – Results of the EBSD analysis of the specimens deformed at 900 ˚C, 1000 ˚C and 1100 ˚C (a-c respectively) presented by way of a band-contrast map (subscript of "1") and an orientation map (subscript of "2"). The Compression axis is vertical for all the micrographs.

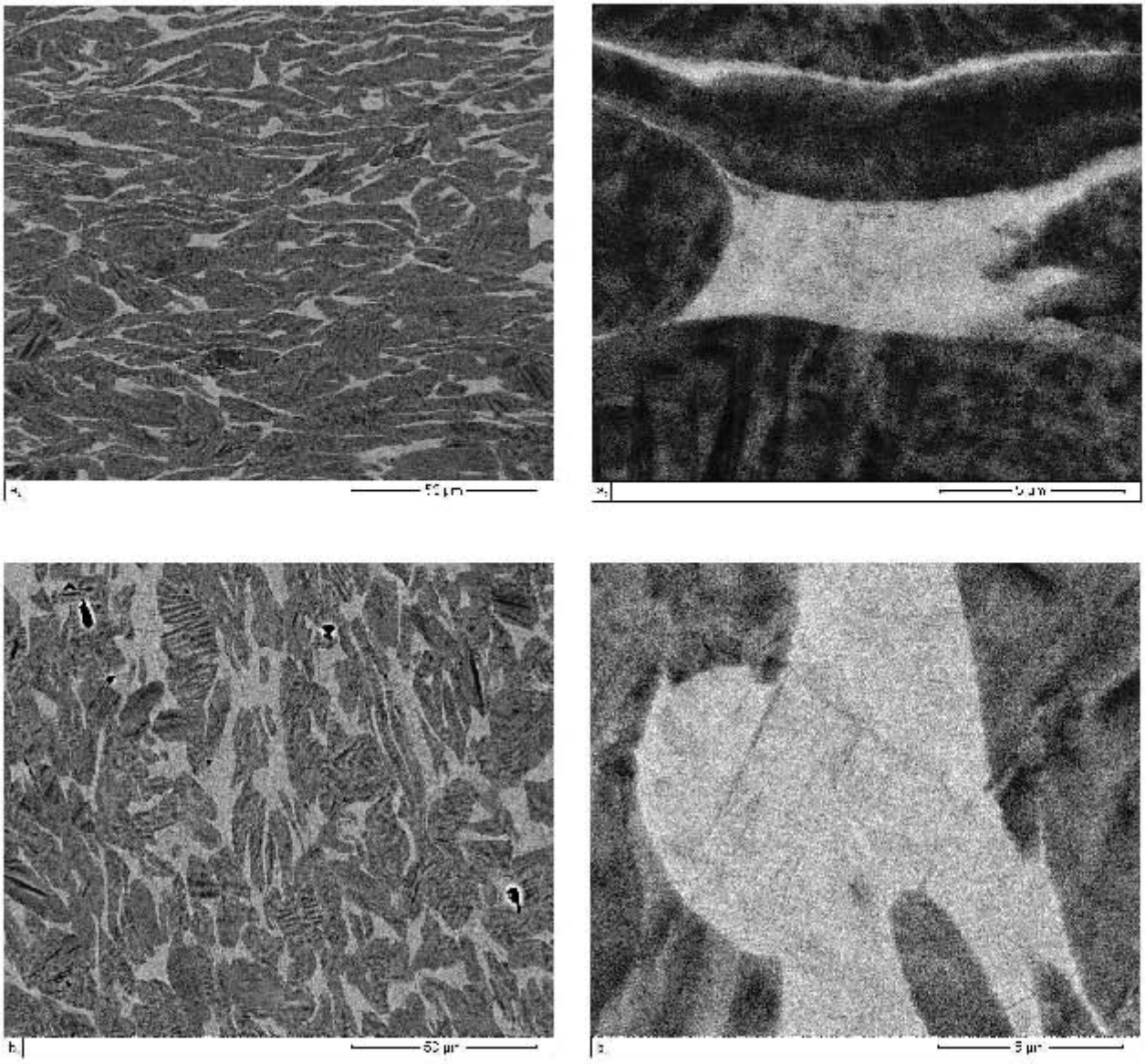

Figure 4.12 – Backscattered electron (BSE) micrographs of the as-deformed microstructure deformed at temperatures of 800 ˚ C (a) and 900 ˚ C (b) at two different magnifications. The subscript "1" denotes a "low magnification" image while "2" denotes a "high magnification" image.

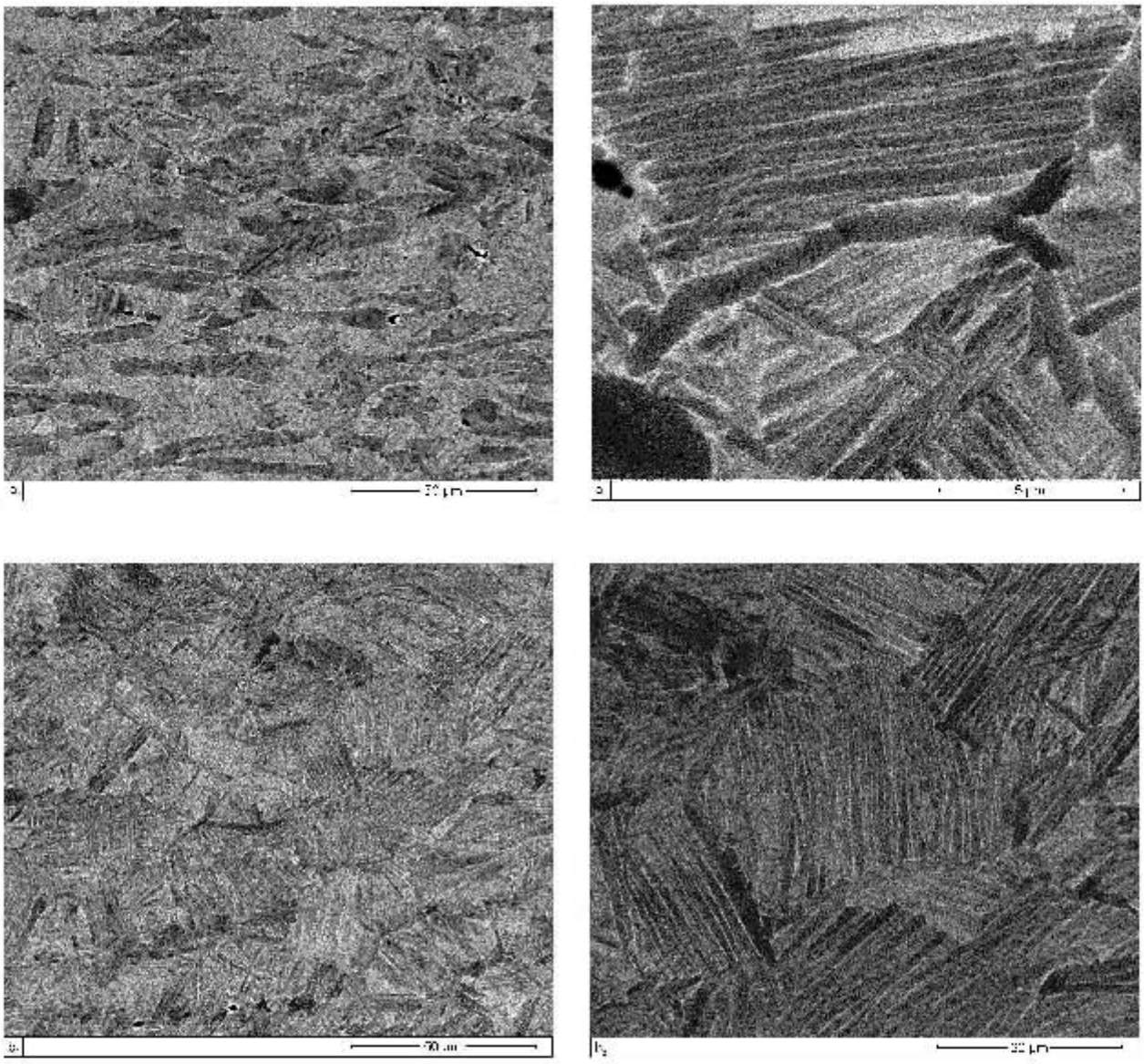

Figure 4.13 – Backscattered electron micrographs (BSE) of the as-deformed microstructure deformed at temperatures of 1000 ˚C (a) and 1100 ˚C (b) at two different magnifications. The subscript "1" denotes a "low magnification" image while "2" denotes a "high magnification" image. Not that the high magnification image of the specimen deformed at 1100 ˚C is at a lower magnification than those for the other 3 deformation temperatures for which BSE images are presented.

4.3.3 Microstructural Observations in the Highly Deformed Region

Specimens Deformed at 600 ˚C and 700 ˚C

By looking at the EBSD results for the specimen deformed at 600 ˚C (figure 4.10a) it can can see from the band contrast map that the microstructure comprises of some β phase which has been coloured blue and two distinct morphologies in the remainder of the microstructure which indexed either as α phase or were unable to be indexed. An Example of the β phase has been labeled with a "Y" on figure 4.10a$_1$. The other two

morphologies have been been labeled with a "W" and an "X". The morphology that has been labeled with an "X" are grains that have clearly been indexed as being α phase. These are the primary α grains that have been retained from the starting microstructure, through the heating and deformation and are still present in the microstructure after it has been forced cooled.

The regions of the microstructure that are like that labeled with an "X" in figure 4.10a$_1$ show a very fine cellular morphology. These areas proved very difficult to index as can be seen in figure 4.10a$_2$, but that material that was indexed in these regions was indexed as α phase.

The microstructure of the specimen deformed at 700 ˚ C (figure 4.10b) comprises the same three morphologies as that deformed at 600 ˚ C: Some β phase that had been retained to room temperature upon cooling; primary α grains; fine polygonal structure.

Specimen Deformed at 800 ˚ C

By looking at the EBSD results for the specimen deformed at 800 ˚ C (figure 4.10c) it is seen that no concentrated areas of β phase were indexed for this specimen as had been seen at the two lower deformation temperatures and only isolated and minimal traces of β phase was detected as shown by the few blue dots seen in the band-contrast map. The remaining two morphologies that comprised the microstructure of the specimens deformed at both 600 ˚ C and 700 ˚ C, namely the primary α grains and the fine polygonal structure discussed for those deformation temperatures are still clearly evident in the specimen deformed at 800 ˚ C. The microstructure of this specimen deformed at 800 ˚ C still comprised 3 discrete types of microstructure, but instead of any concentrated β phase being present, very dark areas of poor signal quality are evident (labeled with a "Z") in the band-contrast map of figure 4.10c$_1$. In these dark areas almost no indexing was possible at all, except for a few isolated points which indexed as being α phase.

In the BSE micrographs of the specimen deformed at 800 ˚ C (figure 4.12a) two distinct and contrasting shades are evident. Areas of a darker shade represent a lower atomic number in that region and the areas lighter in colour represent those areas of higher atomic number. This atomic number contrast is as a result of elemental partitioning between the α and β phases. Vanadium will be concentrated in the β phase and as such the prior β will be of a higher atomic number resulting in it's bright appearance when imaged using a BSE detector. The primary α grains that were present at the deformation temperature will be lean in vanadium content and therefore their relatively low atomic number results in their dark appearance. This interpretation of the BSE images is substantiated by their strong agreement with the morphologies observed in both the light micrographs and EBSD maps for this sample. The high magnification BSE image shown in figure 4.12a$_2$ shows a slight contrast within the light area corresponding to what was β phase at deformation temperature; however this contrast is too subtle to make inferences from.

Specimen Deformed at 900 ˚ C

The EBSD maps of figure 4.11a show that the specimen deformed at 900 ˚ C shows the same three constituents as the sample deformed at 800 ˚ C but in different fractions. The primary α grains are still clearly evident and there is still some of the fine polygonal structure existing within the microstructure, although far less than was observed at all three of the lower deformation temperatures. Finally those very dark (poor pattern quality) areas that were evident in the band contrast map for the specimen deformed at 800 ˚ C are seen here, for the specimen deformed at 900 ˚ C, to have increased in volume substantially and a fine elongated morphology is evident within these areas which has indexed (albeit poorly) as α phase. These areas have been labeled "Z" on 4.11a$_1$.

When considering the BSE micrographs of this specimen (figure 4.12b) we can see, as was the case for the specimen deformed at 800 ˚ C, two distinctly different shades within the images. The bright material, which was explained for the specimen deformed at 800 ˚ C to represent the material that was β phase at the deformation temperature, has increased in volume fraction. This is as expected as a greater amount of β phase would be present at this higher deformation temperature. The high magnification BSE image shown in figure 4.12b$_2$ shows what appear to be very thin (less than 0.4 μm) needle like structures existing within the prior β phase region .

Specimen Deformed at 1000 ˚ C

The microstructure of the specimen deformed at 1000 ˚ C is most easily observed in light micrograph (e) of figure 4.9 on page 77. It is seen in this light micrograph that the microstructure is made up of two separate morphologies and not three as has been the case for all the lower deformation temperatures studied in this work. There are still primary α grains clearly evident in the light micrograph but about 50 % of the microstructure now comprises of a microstructure showing high aspect ratio grains which all index as being of α phase as is seen in the orientation map of figure 4.11b$_2$. Turning our attention to the band contrast map of this specimen in figure 4.11b$_1$ it is more difficult to distinguish between the two morphologies that make up the microstructure that were so distinct in the light micrograph. The reason for this is that, as can be seen in the orientation map, what appeared to be individual elongated grains in the light micrograph are actually grouped together in packets of similar orientation whose dimensions are almost comparable to those of the primary α grains. It is also noted from the orientation map, that at this high deformation temperature the indexing of the specimen has improved as compared to those of the specimens deformed at lower temperatures and still only trace amounts of β phase has been indexed.

From the BSE micrograph of figure 4.13a, the volume fraction of the bright (prior-β phase) material is greatly increased as compared to the specimen deformed at 900 ˚ C which is expected as the higher deformation temperature will result in a greater β phase volume

fraction. The BSE image of figure 4.13a$_2$ shows a high magnification image of the bright (prior β phase) area. Unlike the prior β phase shown in the BSE micrographs of specimens deformed at the lower deformation temperatures, figure 4.13a$_2$ clearly shows structured elemental partitioning within the prior β phase region which consists of darker lamellar structures with divisions of bright material between them.

Specimen Deformed at 1100 ˚ C

The microstructure of the specimen deformed at 1100 ˚ C clearly comprised of only a single morphology. In a similar manner to what was observed for that part of the microstructure of the specimen deformed at 1000 ˚ C that wasn't primary α grains, the microstructure of the specimen deformed at 1100 ˚ C appears to comprise of single elongated grains in the light micrograph of 4.9f, but these individual high aspect-ratio lamellae are seen to be grouped into packets of similar orientation in the EBSD maps of figure 4.11c. Note that at this high temperature the indexing was almost 100%.

As per the EBSD and light micrographs for this specimen, the BSE images of figure 4.13b show no primary α grains and consists entirely of the lamellar structures that appear dark in the BSE image that have light material between them - as described for the high magnification BSE image for the specimen deformed at 1000 ˚ C.

4.3.4 Discussion of Microstructures in the Highly Deformed Region

The discussion of the microstructures existing in the highly deformed centre of the as-deformed cylindrical specimens will begin with the microstructure resulting from deformation at 1100 ˚ C and then proceed with decreasing deformation temperature.

As can be seen from the light micrographs (figure 4.9f), EBSD maps (figure 4.11c) and BSE micrographs (figure 4.13b), at a deformation temperature of 1100 ˚ C , the specimen was in the β single phase at this temperature. This is evidenced by no primary α grains being identified in any of the aforementioned micrographs. The microstructure is seen to comprise of a single morphology. The light micrographs show this morphology to consist of high aspect ratio lamellae that exist in clusters that are aligned parallel to one another. The EBSD orientation maps show that these clusters of parallel lamellae share an orientation and are of α phase. The dark lines that are seen in the light micrograph to separate these individual lamellae are however not clearly evident in the EBSD maps. By analysing the BSE images on this sample, it can be seen that these lamellae appear darker than the thin material that separate them from one another (which appear contrastingly bright). This suggests an atomic number variation between the lamellae and the inter-lamellae material. This is evidence of elemental partitioning within the prior β phase and

this was used by Kelly [13] to identify a diffusional transformation, as by definition a martensitic transformation would result in a compositionally invariant product.

Therefore by considering the information obtained from all of these microscopy techniques, it has been shown that the α colonies of shared orientation that were identified by the EBSD study, are seen by light micrographs to consist of high aspect ratio lamellae separated from one another by what appears in the light micrograph as fine dark lines. The BSE micrographs in turn show this inter-lamellae material to be of greater atomic number than the α lamellae themselves. All of these observations are consistent with a classic nucleation and growth transformation from β phase into a Widmanstätten microstructure where α phase grows from allotriomorphs along the prior β grain boundary in the form of parallel α lamellae of shared orientation with retained β phase present between individual lamellae as explained in "Diffusional β→α Transformation" on page 15. If one considers the high magnification BSE micrograph of figure 4.13b$_2$, all of the features shown in the schematic representation of the diffusional transformation from β phase into a Widmanstätten microstructure (2.10 on page 17) can be identified. The continuous grain-boundary α that has grown around the boundary of the prior-β grain can be identified and from that, the packets of parallel α lamellae growing into the parent β grain.

The lack of indexing of inter-lamellae β phase during the EBSD study can be explained by the fact that the β phase is in fact so fine that it is unlikely to be indexed due to pattern overlap and that which might have been indexed would have been isolated and stood a good chance of being eliminated with even the modest noise reduction applied to the maps presented here, as discussed in the methodology used for the EBSD study on page 57.

This conclusion is in contrast with the findings of Ahmed and Rack [15] and Filip et al. [79], who reported that cooling rates of greater than 20 ˚C/s resulted in a martensitic transformation (figure 2.7 on page 14), as the cooling rate achieved in the current work was in excess of 100 ˚C/s. The temperature of the sample in the current work was recorded by a thermocouple percussion welded to the outside of the specimen and would have cooled quickly as a result of the quench air passing over it, whereas the microscopy was done on the centre of the specimen. It is therefore safe to assume that the cooling rate of the material that has been analysed here by microscopy was below that reported by the thermocouple; however it would still have been greatly in excess of the critical cooling rate of 20 ˚C/s reported to suppress diffusional transformations. Another important consideration would be the considerable affect that an elevated oxygen content (characteristic of BE material as used in this research) has on accelerating the transformation kinetics of Ti-6Al-4V as discussed in the literature review on page 13.

For a deformation temperature of 1000 ˚C, the light micrograph (figure 4.9e) shows about half the microstructure to consist of primary α grains that have been retained upon heating. These primary α grains are clearly seen in the BSE micrograph of figure 4.13a

to be of darker contrast to the remainder of the material which was β phase at the deformation temperature and therefore rich in vanadium. It was concluded (for the exact same reasons as discussed for the specimen deformed at 1100 ˚C) that this prior β phase has transformed by nucleation and growth into a Widmanstätten microstructure. The fact that the lamellar microstructure is grouped into colonies of similar orientation means that the two different morphologies are not easily distinguished from one another in the band-contrast or orientation maps of figure 4.11b, but they are easily distinguished in the light and BSE micrographs (figures 4.9e and 4.13a respectively).

At a deformation temperature of 900 ˚C, the prior β phase (identified by its bright appearance in the BSE micrograph of figure 4.12b) shows no such elemental partitioning as was the case for the prior β phase at the two higher deformation temperatures. Very fine needle like structures appear to be evident within the prior β phase shown in the high magnification BSE image of figure 4.12b and this morphology is also seen within the prior β phase (labelled with a "Z") present in the band contrast map of figure 4.11a$_1$. A fine step size (0.05 μm) EBSD scan was conducted over this region and a misorientation profile was constructed to confirm this region as being prior β phase. The band-contrast map of the scan is shown in figure 4.14 with the line along which the misorientation profile was constructed drawn in. The misorientation profile is given in figure 4.15 on the facing page.

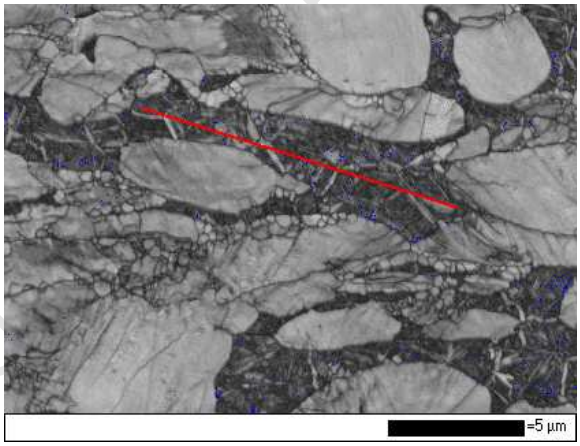

Figure 4.14 – High magnification band-contrast map of specimen deformed at 900 ˚C with the line for a misorientation profile (figure 4.15) drawn in.

This misorientation profile shows misorientations grouped trimodaly around the 30 ˚, 60 ˚ and 90 ˚ marks. These orientations are consistent with those resulting from the transformation from the BCC titanium structure of the parent β grain to HCP titanium and shows that this material is indeed transformed from prior β phase. The compositionally invariant nature of the prior β phase as evidenced by the lack of contrast within the bright material seen in the BSE images and the change in appearance of this prior β in the band contrast maps as opposed to those for the deformation temperature of 1000 ˚C, have led to the conclusion that the β phase present within the material deformed at a temperature of 900 ˚C transforms martensitically upon cooling. The exact nature of the martensite

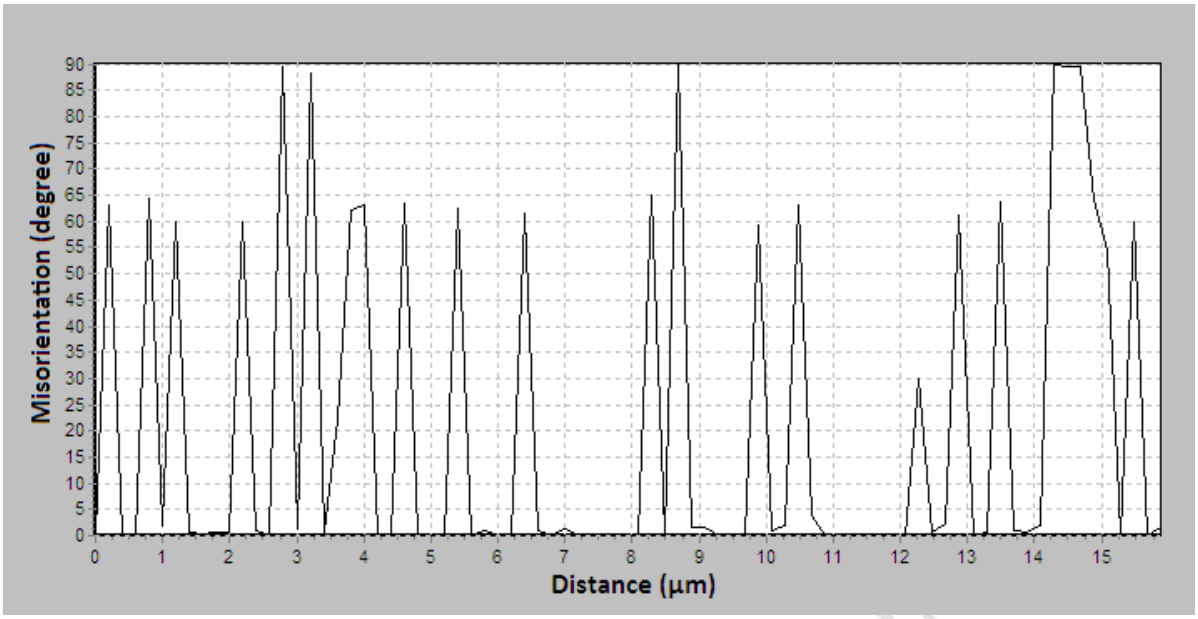

Figure 4.15 – Misorientation profile for the line drawn on figure 4.14

would be impossible to comment on without a thorough TEM study; however the fact that areas within this prior β region have been indexed as HCP during the EBSD study suggest that it has formed an α' martensite. This is substantiated by the misorientation profile conducted within this prior β region showing misorientations grouped trimodaly around the 30 ° , 60 ° and 90 ° marks, as already discussed. These misorientations are indicative of the BCC to HCP transformation.

There is little change in the microstructure of the specimen deformed at 800 ° C as compared to the deformation temperature of 900 ° C, except for a decreasing volume fraction of prior β phase. The β phase that was present at a deformation temperature of 800 ° C was also concluded to have transformed martensitically upon cooling.

It is clear that for a deformation temperature of 600 ° C and 700 ° C, that β phase that was present at the time of deformation has been retained upon cooling down to room temperature and has been indexed as such during the EBSD study. This is due to the fact that the β phase present at such low temperatures is rich enough in β-stabilising vanadium that it is stable down to room temperature.

HCP metals, as was discussed in the literature review on page 50, require either <a+c> slip or twinning to accommodate an arbitrary plastic deformation imposed upon them. Comprehensive studies, as was discussed (page 50), have failed to identify any mechanical twinning taking place in Ti-6Al-4V at temperatures anywhere near even the lowest deformation temperature studied in the present work of 600 ° C. In addition to this, the high interstitial content that characterises BE material is known to greatly suppress twinning. As a result of this, it is assumed that no twinning takes place in the hot upset tests conducted as part of this research. No evidence uncovered through the EBSD study of these specimens shows any evidence to suggest any twinning did take place. Therefore it can be assumed that <a+c> slip must have been in operation. Due to the complexity of

deformation within the HCP unit cell, the deformation of an HCP polycrystalline metal is strongly influenced by grain orientation with those grains initially oriented to accommodate deformation along the c axis preferentially deforming before other less favorably oriented grains. This has been cited as the reason for the development of a heterogeneous microstructure developing in the works of [65, 66] and is considered to be responsible for the fine polygonal structure (labeled as "X" in figure 4.10a$_1$) that has been observed in the microstructures of the specimens deformed as part of this research. It is proposed that the fine polygonal microstructure is born from α grains that were orientated in such a manner as to accommodate the majority of the deformation imposed on the specimens. As such, these α grains would have had a large amount of strain imposed upon them whereas others, not favorably oriented for deformation along the c-axis, would have had far less strain imposed upon them. These grains undergoing minimal deformation would be retained upon cooling and are the primary α grains present in the microstructure of all the specimens deformed up to 1000 ˚ C. Whereas those α grains that have had large amounts of strain introduced into them during the deformation, would have had a sufficient driving force (minimisation of strain energy) to undergo meta-dynamic recrystallisation to create the fine structure observed in those specimens deformed at 600 ˚ C, 700 ˚ C, 800 ˚ C and 900 ˚ C once cooled to room temperature.

For the deformation temperatures within the α+β region (600 ˚ C to 1000 ˚ C), it can be seen from figures 4.10 on page 78 and 4.11 on page 79 that the volume fraction of the fine recrystallised structure decreases with increasing deformation temperature. This can be explained by the following two reasons: the amount of β phase present at the deformation temperature increases as the deformation temperature increases. The β phase is far softer than the α phase and as such, deformation will preferentially take place within the β grains, resulting in less and less deformation and therefore strain taking place within the α grains as the β phase volume fraction increases; the second reason for the amount of fine recrystallised structure decreasing with increasing deformation temperature is that at higher temperatures the rate of recovery mechanisms will be greatly increased and therefore the amount of strain energy introduced into the α grains will diminish with increasing deformation temperatures. Both of these will result in less strain energy being introduced into the α grains and therefore will diminish the driving force for the recrystallisation of these grains into the fine (meta-dynamically) recrystallised structure.

Having Identified prior β phase that was present at each of the deformation temperatures it is immediately obvious that the volume fraction of β phase present at these elevated deformation temperatures is far less than what was experimentally shown for wrought Ti-6Al-4V by Elmer et al. [12] (figure 2.5 on page 12). The β-transus temperature for the material used in that research was given as 974 ˚ C. At a deformation temperature of 1000 ˚ C in this research however, as is most easily seen in the light micrograph in figure 4.9 on page 77 , there is still around 50 % vol. fraction of primary α grains retained at this temperature. This suggests that the β-transus temperature for the material created for

the current research is somewhat greater than 1000 ˚C. This is easily explained by the fact that the impurities such as oxygen which are far greater in BE material as apposed to wrought material are strong α-stabilisers and will therefore have the effect of increasing the β-transus temperature. As can be seen in figure 2.5 on page 12, the gradient of β vol. fraction as a function of temperature at temperatures high in the α+β region is steep and as such, even a small shift in the β-transus temperature will have a pronounced effect on the amount of β phase present at a given temperature within the α+β region.

4.4 Analysis of the Post-Deformation Annealed Specimens

Following the hot uniaxial deformation process, specimens deformed at each of the deformation temperatures tested in this research were annealed for one hour at 870 ˚C. The details of the annealing treatment are given on page 60 and the results of examining the specimens after the annealing treatment are given here.

4.4.1 Microscopy of Annealed Specimens

Both light and electron microscopy was used to analyse the microstructure in the centre of the specimens that were annealed after undergoing uniaxial deformation at temperatures of 600 ˚C, 700 ˚C, 800 ˚C, 900 ˚C, 1000 ˚C and 1100 ˚C. The results of the light microscopy are given in figure 4.16 on the following page and the results of an EBSD study are shown by means of band contrast maps and Euler colour orientation maps in figure 4.17 on page 91 for those specimens deformed at 600 ˚C, 700 ˚C and 800 ˚C and in figure 4.18 on page 92 for those specimens deformed at 900 ˚C, 1000 ˚C, 1100 ˚C. As per the EBSD band-contrast maps for the as-deformed specimens, any β phase that was indexed is coloured blue and anything not coloured blue was therefore indexed as α or was unable to be indexed.

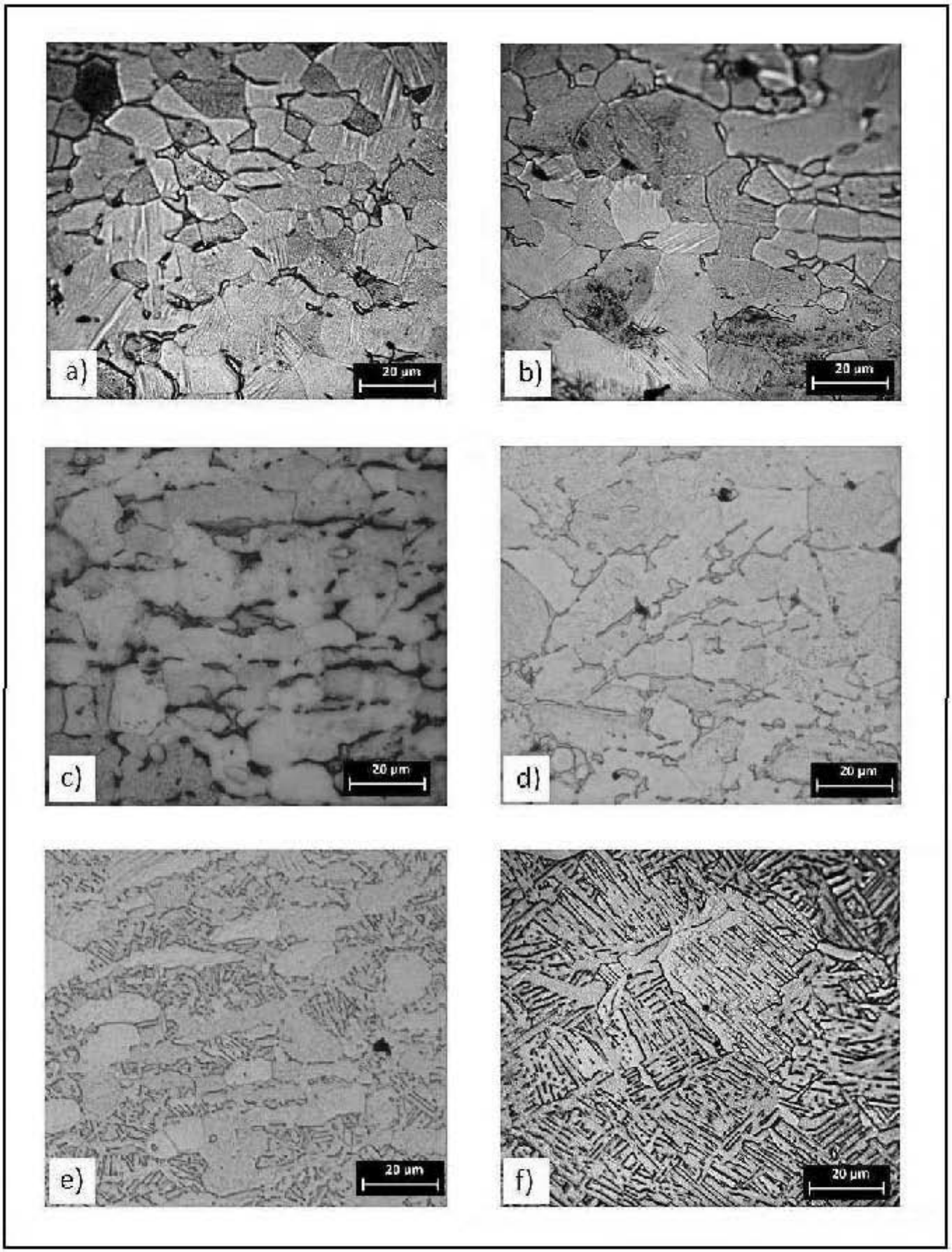

Figure 4.16 – Light micrographs of the microstructure in the centre of samples that were annealed after undergoing uniaxial deformation at a) 600 ˚C , b) 700 ˚C, c) 800 ˚C, d) 900 ˚C, e) 1000 ˚C and f) 1100 ˚C. The Compression axis is vertical for all the micrographs.

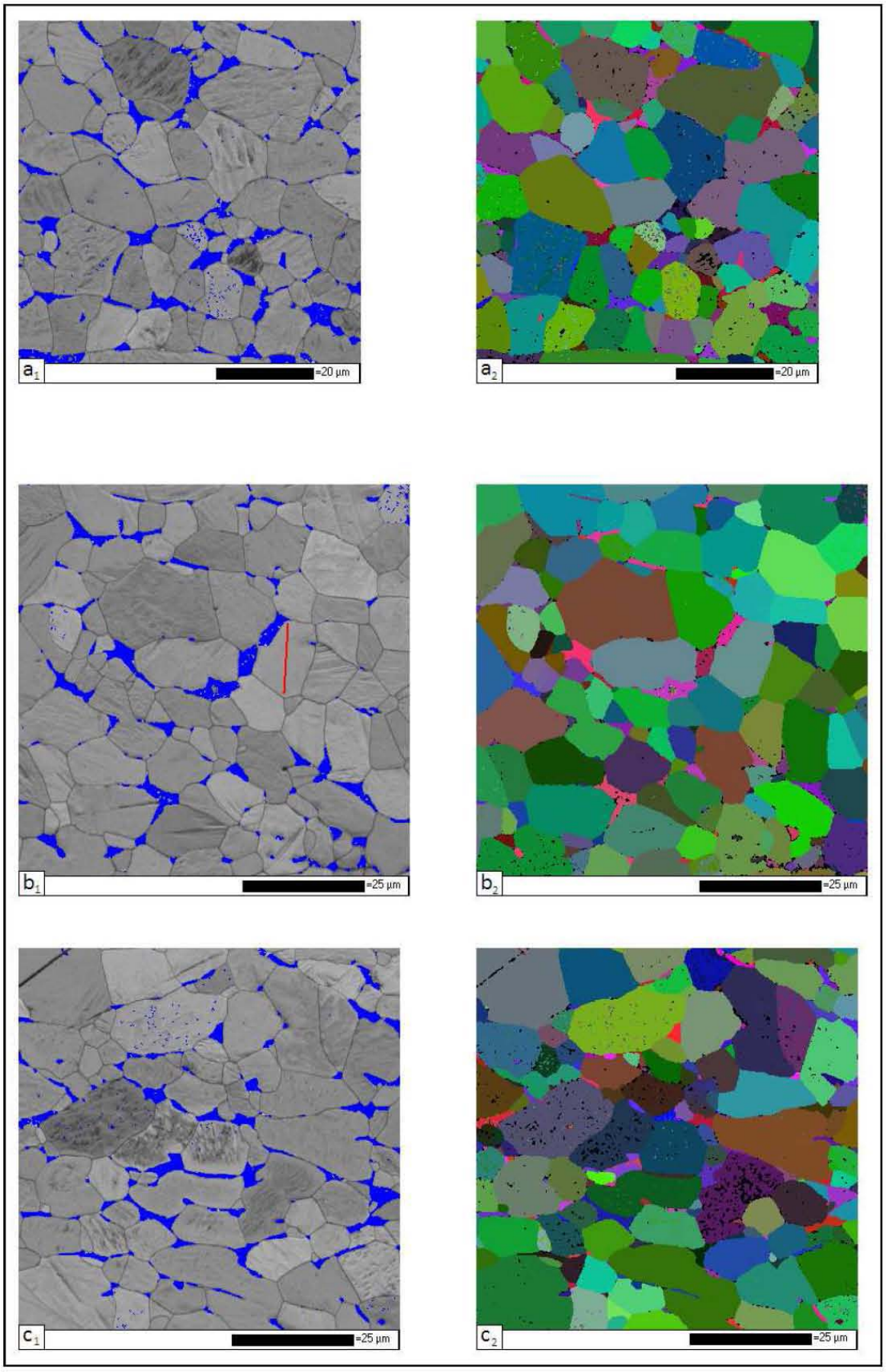

Figure 4.17 – Results of the EBSD analysis of the specimens that were annealed after being deformed at 600 ° C, 700 ° C and 800 ° C (a-c respectively) presented by way of a band-contrast map (subscript of "1") and an orientation map (subscript of "2"). Any β that was indexed is coloured blue in the band-contrast map. The line along which the misorientation profile introduced later in figure 4.20 was conducted is drawn in the band-contrast map of b_1. The Compression axis is vertical for all the micrographs.

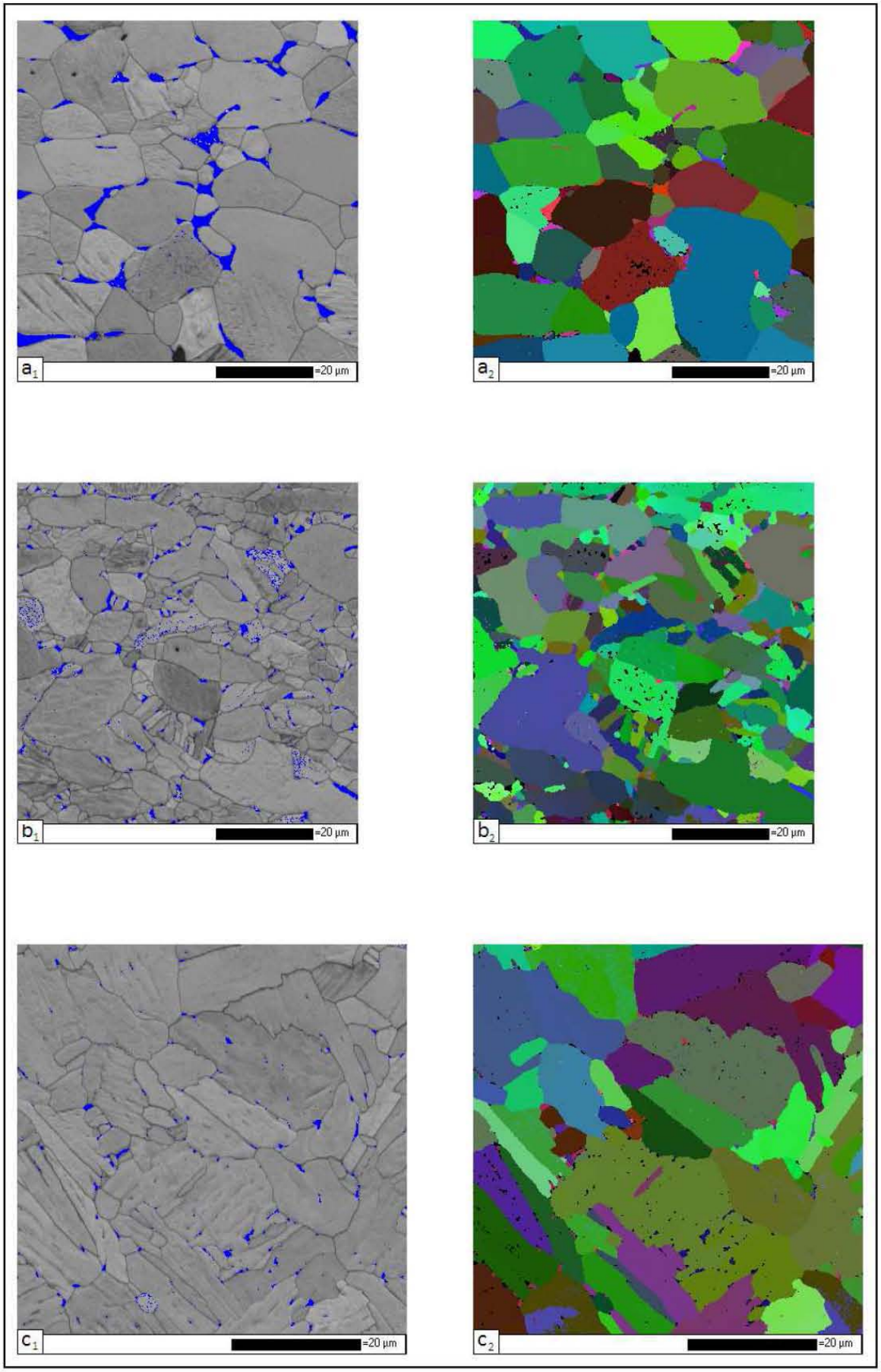

Figure 4.18 – Results of the EBSD analysis of the specimens that were annealed after being deformed at 900 ˚C, 1000 ˚C and 1100 ˚C (a-c respectively) presented by way of a band-contrast map (subscript of "1") and an orientation map (subscript of "2"). Any β that was indexed is coloured blue in the band-contrast map. The Compression axis is vertical for all the micrographs.

4.4.2 Microstructural Observations in the Post-Deformation Annealed Specimens

Specimens Annealed After Undergoing Deformation at 600 ˚ C, 700 ˚ C, 800 ˚ C and 900 ˚ C

As can be seen in both the light micrographs of figure 4.16 on page 90 and the EBSD maps of figures 4.17 on page 91 and 4.18 on the preceding page, the specimens that were deformed at temperatures of 600 ˚ C, 700 ˚ C, 800 ˚ C and 900 ˚ C exhibit (in their centre) a microstructure of equiaxed α grains with some β phase present at the triple points of some of the α grains after being annealed. The average grain size of the equiaxed α grains that are observed in the microstructures for those annealed samples that were deformed at 600 ˚ C, 700 ˚ C, 800 ˚ C and 900 ˚ C were calculated by the Channel 5 Tango mapping program and are given in table 4.2. The misorientation profiles constructed along the lines

Table 4.2 – Average grain diameter for the equiaxed α grains observed in the microstructure of those samples that were annealed after undergoing deformation at 600 ˚ C, 700 ˚ C, 800 ˚ C and 900 ˚ C.

Temperature of Deformation Prior to Annealing Treatment	Average α Grain Diameter (μm)
600 ˚ C	7.6
700 ˚ C	8.6
800 ˚ C	8.1
900 ˚ C	10.7

drawn on the band-contrast maps of the specimen deformed at 700 ˚ C in the as-deformed condition (figure 4.10b) and the post-deformation annealed condition (figure 4.17b) are shown here by figures 4.19 on the next page and 4.20 on the following page respectively.

Specimen Annealed After Undergoing Deformation at 1000 ˚ C

By comparing the light micrographs of the specimen deformed at 1000 ˚ C in the as-deformed condition in figure 4.9 on page 77 and in the post-deformation annealed condition in figure 4.16 on page 90, it can be seen that the primary α grains that existed in the as-deformed specimen are still evident in the microstructure after being annealed. The α/β lamellar structure that existed between these primary α grains in the as-deformed specimen can however be seen to have changed as a result of the annealing treatment. In the as-deformed condition the lamellar structure appears as a very fine structure. After being annealed this Widmanstätten material still has an elongated morphology, but has changed to become far more coarse - the aspect-ratio decreasing noticeably.

Specimen Annealed After Undergoing Deformation at 1100 ˚ C

By comparing the Euler colour orientation maps of the specimen deformed at 1100 ˚ C in the as-deformed (figure 4.11) and post-deformation annealed (figure 4.18) conditions,

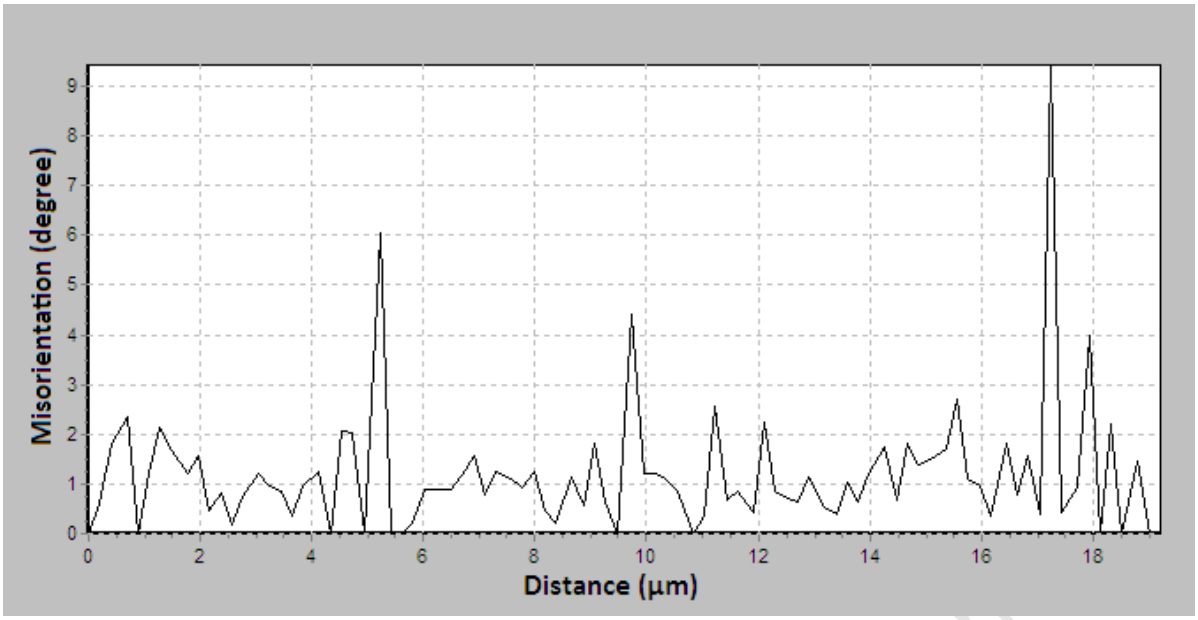

Figure 4.19 – Misorientation profile conducted along the line drawn on the band contrast map of figure 4.10b as part of the EBSD study of the as-deformed microstructure of the specimen deformed at 700 ˚ C.

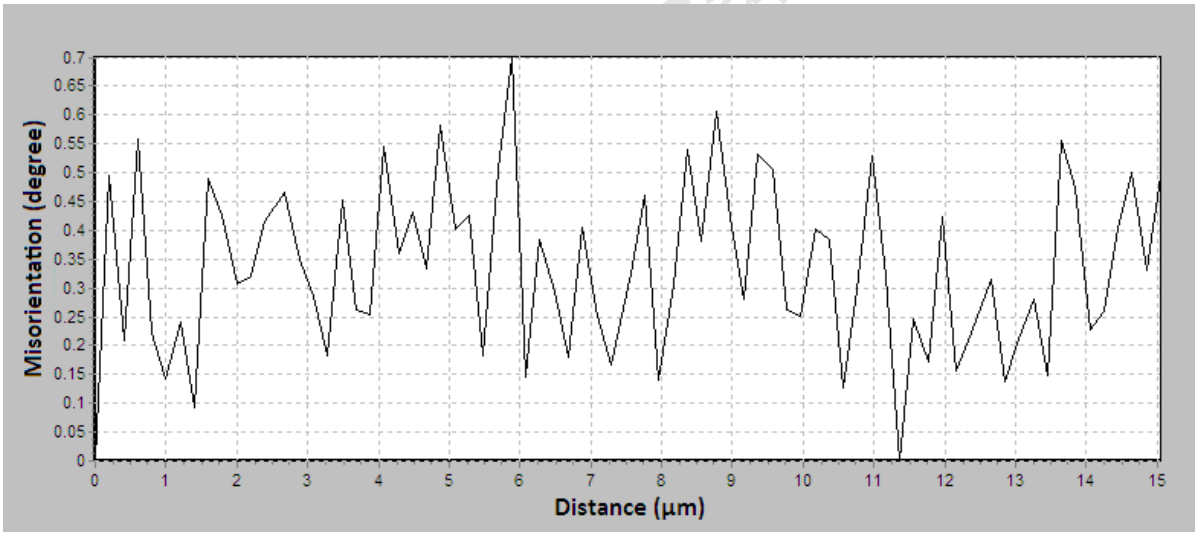

Figure 4.20 – Misorientation profile conducted along the line drawn on the band contrast map of figure 4.17b as part of the EBSD study of the post-deformation annealed microstructure of the specimen deformed at 700 ˚ C.

it is seen that the annealing process had little affect on the fundamental morphology of the microstructure and both specimens show a Widmanstätten colony microstructure. These colonies are seen to have increased in size slightly following the annealing process, as compared to the as-deformed condition, and slight spheroidisation of these colonies is observed - evidenced by the rounded edges to the colonies in the annealed condition compared to their very jagged and sharp edges in the as-deformed condition.

4.4.3 Discussion of Microstructures in the Post-Deformation Annealed Specimens

By comparing the misorientation profiles for the equiaxed α grains evident in the microstructure of the specimen annealed after undergoing deformation at a temperature of 700 ˚ C and the primary α grains present in the as-deformed structure (figures 4.19 and 4.20 respectively) it is evident that the annealed grains have negligible strain within their crystal structure as compared to the primary α grains present in the as-deformed structures. This alleviation of strain energy and more so, the change from the heavily distorted, heterogeneous morphologies of the as-deformed specimen could not have taken place by static recovery alone and the microstructure has clearly fully recrystallised upon being subjected to the annealing process. This is clearly also the case for the specimens deformed at temperatures of 600 ˚ C, 800 ˚ C and 900 ˚ C.

The increase in the average grain size of the equiaxed grains resulting from recrystallisation process from 7.6 μm for the sample deformed at 600 ˚ C to 10.7 μm for the sample deformed at 900 ˚ C can be explained by the fact that metadynamic recovery during the deformation and subsequent cooling processes would have been more rapid at the higher temperature. This would result in fewer recrystallised grains being nucleated (either meta-dynamically during the deformation and cooling or statically during the annealing process) and hence the individual recrystallised grains would be able to grow larger while driven by the strong driving force of minimisation of strain energy before meeting another strain-free recrystallised grain and growth continuing further by the comparatively low driving force of minimising the grain boundary area (and hence the energy associated with grain boundaries).

The fact that the specimens that were deformed at 600 ˚ C, 700 ˚ C, 800 ˚ C and 900 ˚ C recrystallised upon annealing means that sufficient strain energy was imparted to the microstructure during the deformation process to create the critical driving force required for recrystallisation.

The sample deformed at 1000 ˚ C and subsequently annealed still shows α grains that are of a deformed shape (seen most easily in the light micrograph of figure 4.16f). This shows that these are still primary α grains that were present from the as-sintered microstructure, were retained throughout the heating and deformation process and subsequently throughout the annealing process. This means that at a deformation temperature of 1000 ˚ C, insufficient strain energy was retained in the specimen to result in recrystallisation when annealed. This would be due to the fact that at such a high temperature, metadynamic recovery would be very rapid and that there was considerable amounts of softer β phase present at this deformation temperature. The lamellar microstructure present between these primary α grains after deformation is seen to undergo grain growth when annealed. The specimen deformed at 1000 ˚ C and annealed therefore comprises of a bimodal microstructure of primary α grains and α/β lamellae.

At the highest deformation temperature of 1100 ˚C, the deformed microstructure consisted entirely of Widmanstätten structure and as such was still of lamellar structure after being annealed with the most noticeable change resulting from the annealing treatment being the spheroidisation of the lamellar colonies that appeared as sharp and jagged in the as-deformed specimen.

4.5 Decisions Made For Mechanical Testing Based on Findings From Uniaxial Deformation Experiments

The deformation temperatures of 800 ˚C and 1000 ˚C were chosen for the TMP parameters that would be used for the PSC deformation in order to create mechanical test specimens.

The deformation temperature of 800 ˚C was chosen as it offered a good compromise between creating a refined and recrystallised equiaxed microstructure and at the same time had the benefit of a reduced flow stress as compared to the specimens deformed at the two lower temperatures of 600 ˚C and 700 ˚C.

Deformation temperatures of 600 ˚C, 700 ˚C, 800 ˚C and 900 ˚C were seen to result in a recrystallised microstructure after an annealing treatment. The grain size measurement presented in table 4.2 on page 93 for these deformation temperatures reveal little change in the average grain size for the deformation temperatures of 600 ˚C, 700 ˚C and 800 ˚C. A deformation temperature of 900 ˚C however, was seen to result in markedly larger recrystallised grains after being annealed. In order to achieve the benefits of a refined microstructure and at the same time maintaining as high a deformation temperature as possible for the ease of deformation benefits, a deformation temperature of 800 ˚C was chosen for the PSC deformation and mechanical test specimens.

In order to evaluate the role of microstructural refinement on the mechanical properties of the TMP material, it was desirable to also test a deformed specimen that did not feature this recrystallised microstructure. As the deformation temperature of 1100 ˚C had posed considerable difficulties during these uniaxial deformation trials, it was decided to carry out PSC TMP at a temperature of 1000 ˚C, which has been shown not to recrystallise following an annealing treatment and results in a bi-modal microstructure.

Chapter 5

Results and Discussion of Plane Strain Compression and Mechanical Testing

Three TRB specimens were deformed by PSC at each temperature of 800 ˚ C and 1000 ˚ C in order to enable the mechanical testing as a function of TMP process condition.

These three specimens processed at 800 ˚ C and 1000 ˚ C will be referred to as PSC800(1), PSC800(2), PSC800(3), PSC1000(1), PSC1000(2) and PSC1000(3) respectively and this designation will be used throughout this chapter.

5.1 As-Sintered Specimens

The BE powder used for the creation of the TRB specimens to undergo PSC was exactly the same powder as that used to create the cylindrical specimens for the uniaxial deformation; furthermore the powder compaction process and sintering program was kept exactly the same as that used in the creation of those cylindrical specimens. As such the as-sintered TRB specimens were seen to have exactly the same microstructure and relative density (around 88%) as was discussed in the results and discussion of the uniaxial deformation on page 70.

5.2 Deformation Curves for PSC Deformation

The time-temperature and true stress-true strain curves resulting from the PSC deformation of the as-sintered TRB specimens are given in figures 5.1 and 5.2 on the following page respectively.

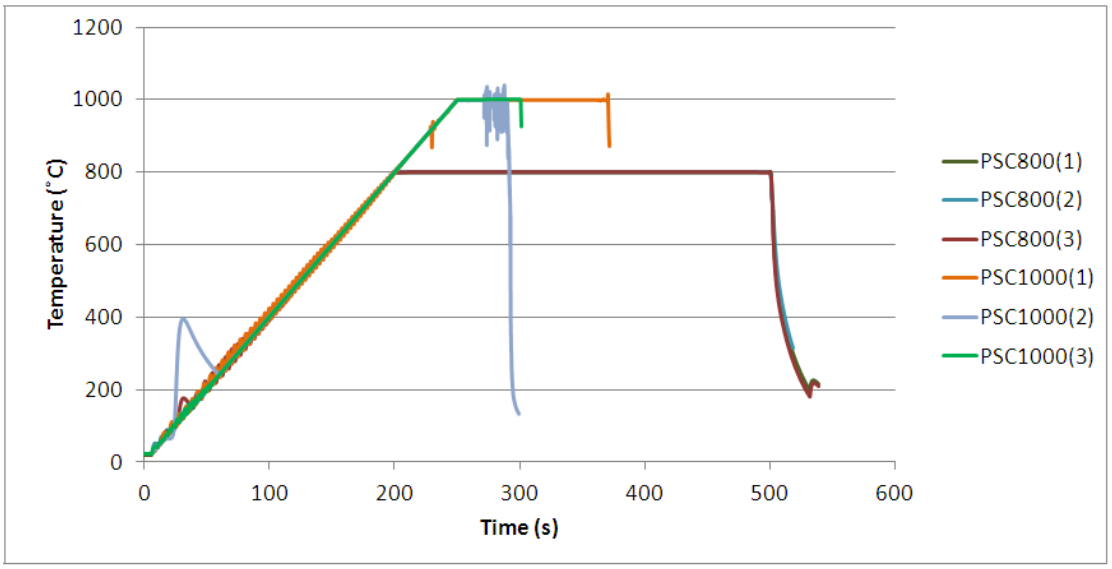

Figure 5.1 – Time-temperature graph of the PSC deformation process conducted on the six as-sintered TRB specimens.

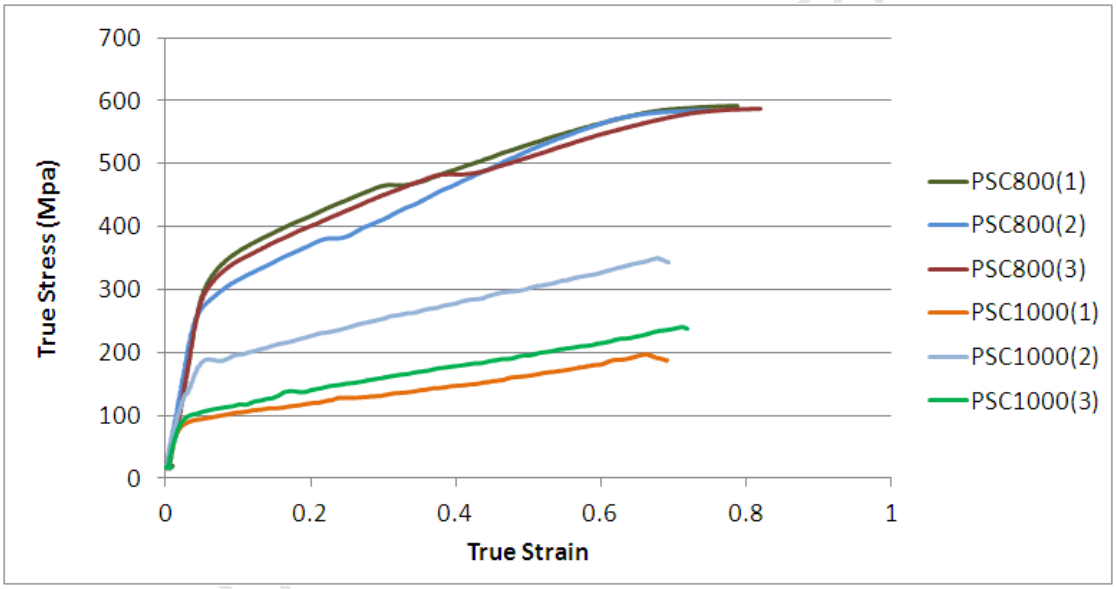

Figure 5.2 – True stress-true strain graph of the PSC deformation process conducted on the six as-sintered TRB specimens.

5.3 Discussion of the Deformation Curves during PSC Deformation

From analysing the time-temperature and true stress-true strain curves in figures 5.1 and 5.2 respectively for the PSC deformation of as-sintered TRB specimens we can see that for a deformation temperature of 800 °C, this temperature was held perfectly constant during the soak period preceding the deformation. This has resulted in true stress-true strain curves for the specimens PSC800(1), PSC800(2) and PSC800(3) that show little deviation from one another.

Contrastingly, a perfectly constant soak temperature for all of the specimens deformed at

1000 ° C - PSC1000(1), PSC1000(2) and PSC1000(3) - was not achieved. This is as a result of the heating difficulties associated with these tests as discussed in the methodology on page 64 and is seen to result in true stress-true strain curves that show large discrepancies between each other. The specimen PSC1000(1) is seen to have maintained a constant soak temperature at 1000 ° C and as such shows the lowest flow stress during deformation. The soak temperature for specimen PSC1000(2) is seen to have become unstable just prior to deformation and in fact the deformation commenced at a temperature of 980 ° C resulting in the greatest flow stress during deformation of those specimens deformed at 1000 ° C. Although no such unstable soak temperature for specimen PSC1000(3) was observed, as was the case for specimen PSC1000(2), analysis of the data does show that the temperature at the time of deformation was about 990 ° C and this is evident in the slightly higher flow stress during deformation of this specimen as compared to PSC1000(1). As can be seen from the temperature-time graphs and was discussed in the experimental methodology on page 63, specimen PSC1000(1) was soaked at temperature for 2 minutes prior to deformation, specimen PSC1000(3) for 50 seconds and PSC1000(2) for just 40 seconds.

The true stress-true strain curves shown in figure 5.2 on the facing page show a strain for the specimens deformed at 800 ° C that is greater than 0.69. This is as a result of the "compliance adjustment" used during their deformation as discussed on page 64.

5.4 Mechanical Testing

Following the annealing treatment of the TRB bars which underwent PSC deformation the thickness in the deformed region was measured as is given in table 5.1. As can be seen,

Table 5.1 – Thickness of the deformed region on the as-deformed TRB specimens after undergoing PSC deformation to a strain of 0.69 and the amont of material needed to be surface ground of each side to achieve the three-point-bend specimen thickness of 2.80mm.

Specimen	thickness of as-deformed specimen (mm)	Amount of material to be ground off each surface (mm)
PSC800(1)	3.68	0.44
PSC800(2)	3.80	0.50
PSC800(3)	3.40	0.30
PSC1000(1)	3.20	0.20
PSC1000(2)	3.36	0.28
PSC1000(3)	3.36	0.28

the specimens had varying thicknesses in the deformed region following PSC deformation resulting from their varying initial thicknesses. As a result of this, different amounts of material was removed for each of the specimens to achieve the 2.80mm nominal thickness used for the three-point-bend specimens. As was discussed in the methodology, care was

taken that the material required to be removed was done so equally from each surface. This too is shown in table 5.1 on the preceding page.

5.4.1 Three-Point-Bend Specimens

In addition to the specimens deformed by PSC at temperatures of 800 ˚ C and 1000 ˚ C, three-point-bend tests were conducted on three specimens of the as-sintered material and three specimens of a commercial IM Ti-6Al-4V material. The three as-sintered specimens will be referred to as: A-S(1), A-S(2) and A-S(3) and the specimens produced from the commercial stock: IM(1), IM(2) and IM(2). Micrograph sections through the thickness of an as-sintered specimen and specimens deformed by PSC at 800 ˚ C and 1000 ˚ C are shown in parts a-c respectively of figure 5.3. As is clearly seen in figure 5.3, the porosity in the

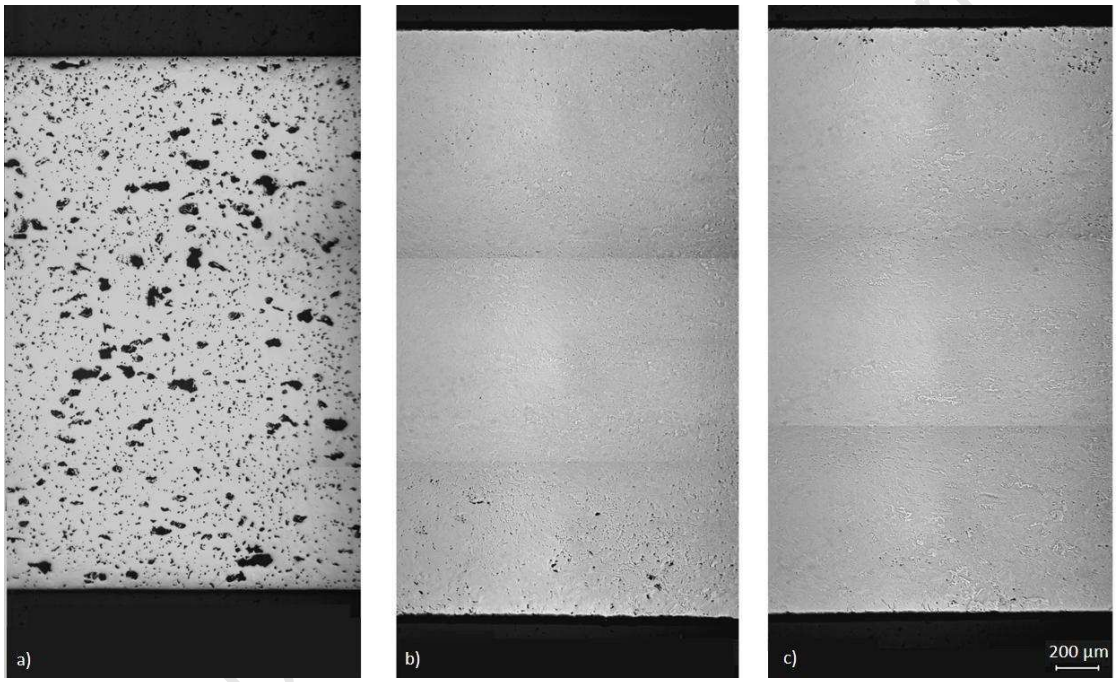

Figure 5.3 – Micrograph sections through the thickness of three-point-bend specimens in the a) as-sintered condition, b) PSC deformed at 800 ˚ C and c) PSC deformed at 1000 ˚ C.

TMP processed specimens has been greatly reduced as compared to that of the starting as-sintered condition. Measuring the density of the six TMP processed three-point-bend specimens gave the results presented here in table 5.2 on the facing page. When comparing these reported densities against the micrograph sections and the degree of porosity shown in figure 5.3, one might get the impression that the densities are somewhat inflated, as may well be the case as was discussed when presenting the measured densities of the uniaxially deformed cylinders on page 75.

The commercial IM material used to create three-point-bend specimens for comparative purposes was received as annealed plate which was then subjected to the same final heat treatment as the TMP processed BE material, i.e the annealing treatment detailed on page 60. The microstructure of this commercial Ti-6Al-4V can be seen in figure 5.4 to

Table 5.2 – Measured relative densities of the TMP processed specimens produced for three-point-bend tests.

Specimen	relative density (%)
PSC800(1)	99.5
PSC800(2)	98.2
PSC800(3)	99.5
PSC1000(1)	99.5
PSC1000(2)	99.0
PSC1000(3)	98.5

comprise of equiaxed α grains with β phase present at the α grain boundaries and triple points. The microstructure of the three-point-bend specimens created from the TMP processed BE samples are seen in figures 5.5 and 5.6 on the next page for deformation temperatures of 800 ˚ C and 1000 ˚ C respectively. As was the case for the cylindrical samples that underwent uniaxial deformation, the specimen deformed by PSC at 800 ˚ C and annealed comprised of fully recrystallised α grains with β phase present at the α grain boundaries and triple points and the specimen deformed by PSC at 1000 ˚ C and annealed had a bimodal microstructure of primary α grains as well as Widmanstätten α/β structure.

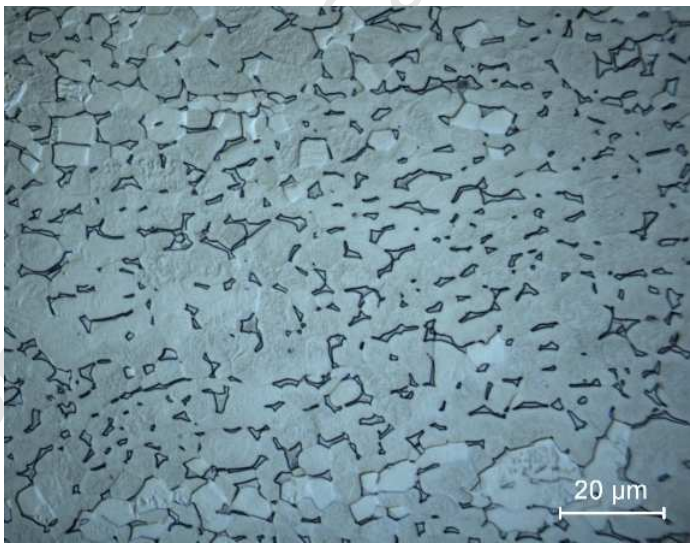

Figure 5.4 – Light micrograph showing the equiaxed microstructure of the commercial IM Ti-6Al-4V material used for three-point-bend tests as a referance.

5.4.2 Three-Point-Bend Results

The results of the three point bend tests are shown for the as-sintered specimens and the TMP processed specimens in figure 5.7 on page 103 by way of a plot of bending stress as a function of midpoint deflection. For comparative purposes, the results of bending tests conducted on the commercial stock specimens are shown in the same manner in figure 5.8 on page 103.

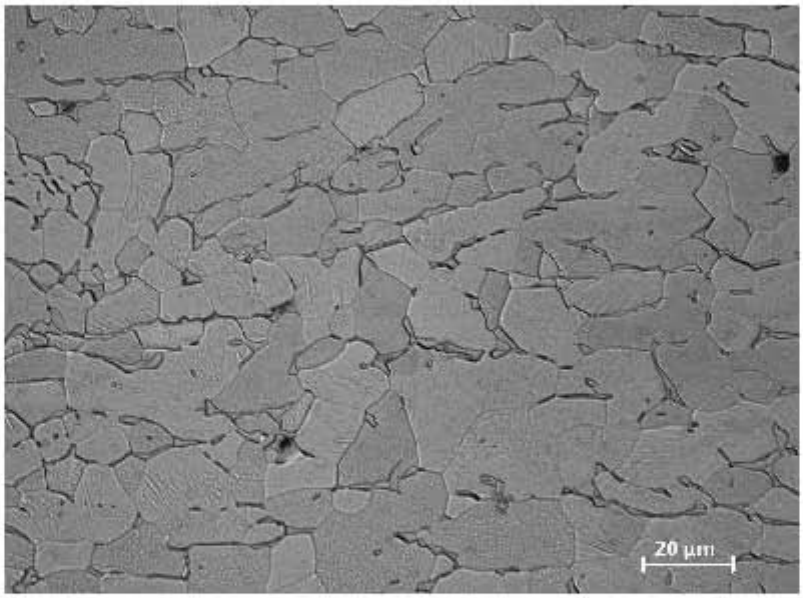

Figure 5.5 – Light micrograph of the microstructure within the three-point-bend specimen created from the be material that underwent PSC deformation at 800 ˚C and was subsequently annealed. The microstructure is seen to comprise of fully recrystallised a grains with β phase present at the a grain boundaries and triple points.

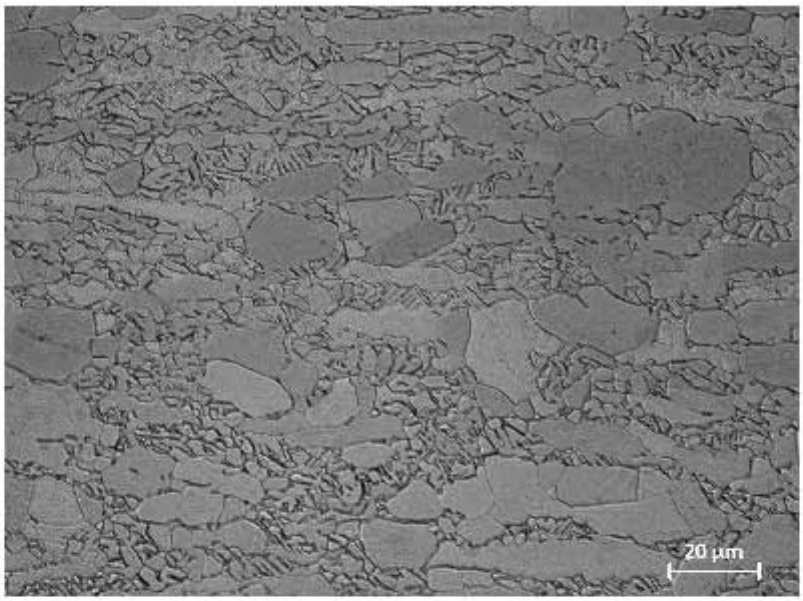

Figure 5.6 – Light micrograph of the microstructure within the three-point-bend specimen created from the BE material that underwent PSC deformation at 1000 ˚C and was subsequently annealed. The microstructure is seen to comprise of primary a grains as well as Widmanstätten a/β structure.

When interpreting these three-point-bend plots one must be careful not to attach too much meaning to the x-axis values of midpoint deflection. Whereas the bending stress (plotted on the y-axis) is an intrinsic property, the midpoint deflection is an extrinsic value which depends on the cross-sectional geometry of the specimen. It may therefore be interpreted as the deflection that was required to produce a certain bending stress in the outer most material of the specimen as per the theories of simple bending. Even though effort was taken in this research to maintain constant cross-sectional dimensions

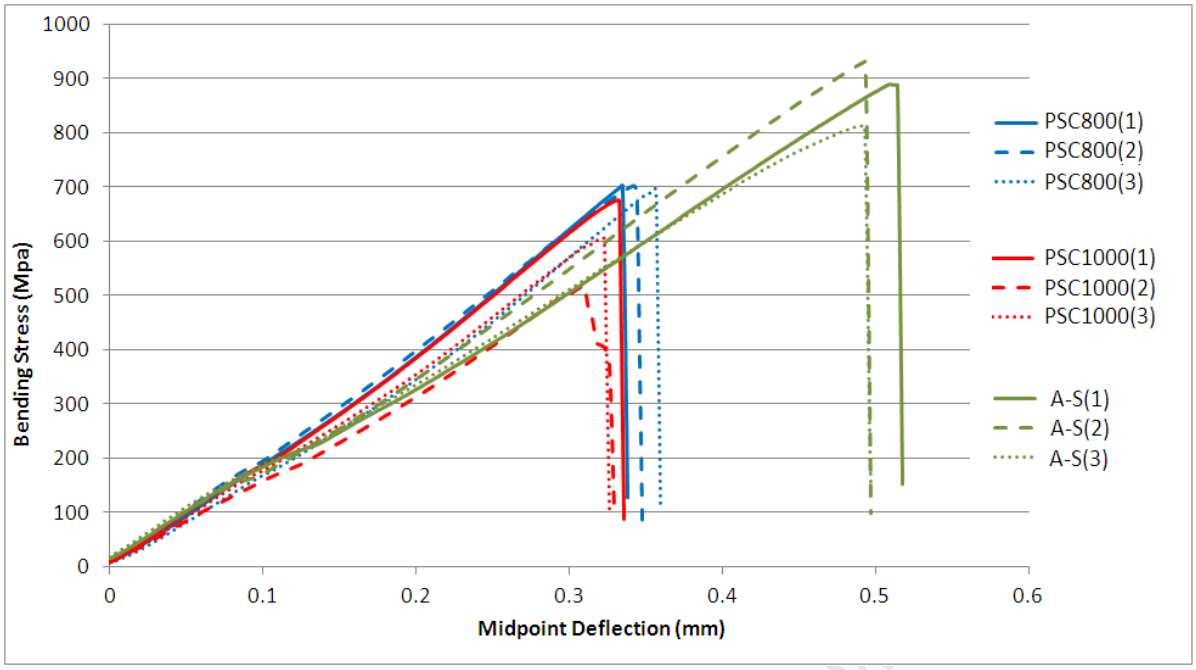

Figure 5.7 – Graphs plotting the bending stress as a function of the midpoint deflection as obtained from the three-point-bend tests conducted on the as-sintered and TMP processes BE material.

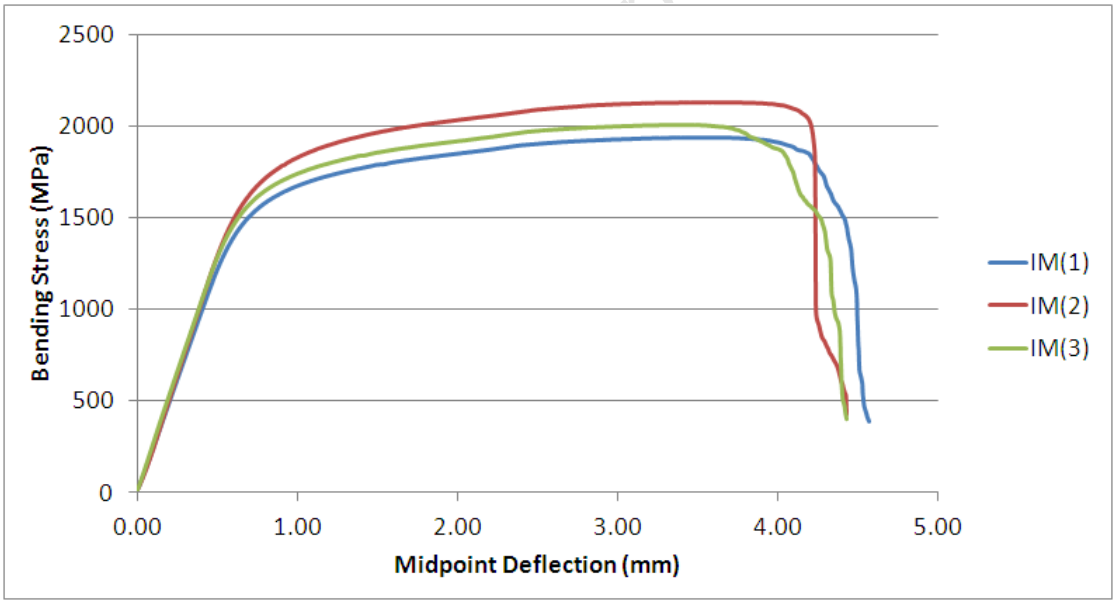

Figure 5.8 – Graphs plotting the bending stress as a function of the midpoint deflection as obtained from the three-point-bend tests conducted on the commercial stock material.

for all three-point-bend specimens, even small discrepancies in the thickness dimension will create a change in the mid-point deflection values. As a result of this, one cannot make inferences as to a material's properties based on the midpoint deflection at point of fracture, or the slope of the curves. The important properties that can be ascertained from these tests will be the failure stress (the transverse rupture stress according to MPIF standard 41, so long as the requirement of maximum plastic deformation is satisfied).

With this in mind, it is clearly seen that no evidence of any plastic deformation is evident in the three-point-bend curves for the as-sintered or TMP processed BE material shown

in figure 5.7. Therefore the failing stress may be interpreted as the transverse rupture strength of the materials. It is clear that the as-sintered material had a higher transverse rupture strength as compared to the TMP processed BE specimens processed at either of the two deformation temperatures tested. Furthermore it is noted that all three of the specimens that were processed at a deformation temperature of 800 ˚C had higher transverse rupture strength than those deformed at a temperature of 1000 ˚C.

The bending stress-midpoint deflection curves resulting from the three-point-bend tests conducted on the commercial material (figure 5.8) show that the material displayed a considerable amount of ductility and that this material yielded to plastic deformation at a bending stress in excess of the transverse rupture strength of the BE material in both the as-sintered and the processed conditions.

5.4.3 Hardness Testing Results

Hardness tests were conducted on the three-point-bend specimens A-S(1), PSC800(1), PSC1000(1) and IM(1) using a 10kg indenting force and the results are shown in figure 5.9 on the facing page. As can be seen, the IM material was measured to have a hardness of 320HV when measured using the 10kg indenting force, the hardnesses of specimens A-S(1), PSC800(1) and PSC1000(1) were 269HV, 419HV and 427HV respectively. In the case of the TMP processed specimens, this shows a significantly higher hardness than for the commercial material. The 11 hardness measurements taken for the A-S(1) specimen using the 10kg indenting force are seen to have a large variability ranging over 100 HV. The variability of the measurements taken for the TMP processed and commercial specimens are seen to be far less than that for the as-sintered material. In an attempt to determine the influence of the pores on the measured hardness of the A-S(1) specimen, the micro hardness was determined using indenting forces of 500g and 100g and efforts were made to conduct these measurements on pore-free areas of the as-sintered microstructure. The same micro hardness measurements were conducted on the PSC1000(1) and IM(1) specimens. These results are also shown with those results from the 10kg indenting force in figure 5.9 on the next page. The increasing variability of the measurements made for the PSC1000(1) and IM(1) samples using the micro hardness indenter testify to the increased difficulty in measuring hardness using a very small indent. In these two specimens, despite an increase in the variability of the hardness measurements, the mean value remains virtually unchanged from that measured with the 10kg indenting force. For the A-S(1) specimen however, there is a clear trend of increasing hardness measurements with decreasing indenting force.

5.4.4 Discussion of Mechanical Tests

The density of the as-sintered material was increased from about 88% to at least 98% for all of the 6 TMP processed specimens tested in three-point-bending. This resulted in the

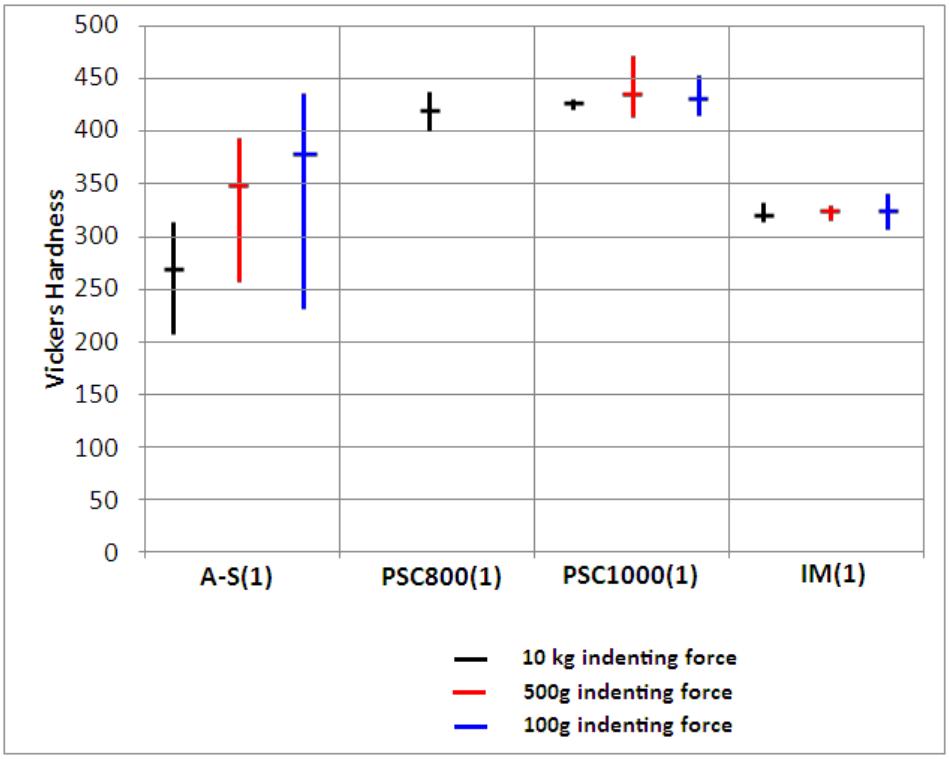

Figure 5.9 – Hardness measurements conducted on the specimens A-S(1), PSC800(1), PSC1000(1) and IM(1) using 100g, 500g and 10kg indenting forces. The vertical line shows the range of the measurements and the horizontal line marks the mean of the measurements. 11 measurements were conducted for each set of data.

hardness measured with a 10kg force to increase from 269HV in the as-sintered condition to 419HV and 427HV for the specimens deformed at 800 ˚C and 1000 ˚C respectively. When measuring the hardness by means of micro-hardness indentation at forces of 500g and 100g, the mean value for the specimen deformed at 1000 ˚C was measured to be 10HV higher than the measurement achieved using a 10kg indenting force, whereas for the specimen in the as-sintered condition, the mean hardness measurement rose by as much as 110HV using microhardness indentation as compared to the values obtained using a 10kg indenting force. This suggests that the porosity within the material in the as-sintered condition was interacting with the hardness indents when an indenting force of 10kg was used resulting in the measured hardness being so low. When measuring the hardness of the as-sintered material with the micro hardness indenter and making an effort to avoid pores, a substantial increase in the measured hardness occurred. The possibility of this being as a result of a systematic error was eradicated by conducting all of the same hardness measurements on the commercial material specimen - IM(1) - which exhibits an increase in the variability of the 11 measurements taken as compared to those using the 10kg indenting froce, but the mean remains almost constant for the three different indenting forces.

These findings suggest that the hardness of the PM material studied in this research is significantly harder than commercial IM material. The lower hardness of the as-sintered material as measured by 10kg indenting force has been shown to be as a result of pore

interaction and micro-hardness measurements have shown that the pore-free material has a hardness nearly as high as those PM specimens that underwent TMP. Those BE specimens that underwent TMP were measured to have a hardness in excess of 100VH greater than the IM material.

All of the PM material specimens subjected to three-point-bend tests fractured in a brittle manner and exhibited no signs of any plastic ductility prior to fracture. This inherent brittle nature of the BE PM material is in accordance with the high hardness measurements of the material and is most likely as a result of the high oxygen content associated with the BE powders used.

Other researchers [35, 38–40, 62, 77] who determined the mechanical properties of BE Ti-6Al-4V created by simple press and sinter techniques all reported significant plastic ductility when subjecting the material to tensile loading. Importantly it must be noted that in all of those cases the material was created using titanium powders blended with an Al-V master alloy powder. It is therefore suspected that the use of separate elemental powders, rather than a master alloy, in creating the material used in the current research has contributed to its brittle behaviour. Both the aluminium and vanadium powders will have an oxide layer on the surface of the particle and it is possible that separate elemental powders have a far greater impurity associated with them than master alloy powder.

The hard and brittle nature of the BE PM material used in this work would not be able to be altered by any TMP, but one would still expect to see an increase in rupture strength with an increase in density of the material. This was however not the case and all 6 of the TMP three-point-bend specimens tested exhibited a rupture strength of at least 100MPa less than the weakest of the as-sintered specimens, despite having densities that were greater than the as-sintered specimens by more than 10%.

These findings are in contrast to the norms of PM, where mechanical properties are said to be normalised by density; however what must be considered is that such rules of thumb for the PM industry would relate to the density achieved as a result of the primary PM manufacturing and not, as is the case here, the density resulting after such processes as TMP. The TMP that the as-sintered material was subjected to as part of this research achieved the relative density ($> 98\%$) that has been concluded [36] to result in PM components whose mechanical properties are competitive with those of IM products; however the measured rupture strength for each of the TMP specimens tested was far less than in the as-sintered condition.

Therefore the strength increase that was achieved by the TMP of BE Ti-6Al-4V compacts by the researchers Lee et al. [77] and Weiss et al. [40] discussed in the literature review on page 52 was not accomplished in the present work. Two noticeable differences in the research conducted by the aforementioned groups and the current work is the far higher relative density of the as-sintered preforms used in their work (around 98%) and the ductile nature of the material created in those works as compared to the brittle material

created in this work, believed to be as a result of using separate elemental powders instead of an Al-V master alloy powder.

Chapter 6

Investigation of the Fractured Three-Point-Bend Specimens

The three-point-bend specimens that fractured when being tested were analysed by light microscopy. This analysis was conducted by viewing the fracture area from two separate orientations. The two different surfaces that were prepared for examination are shown in figure 6.1, where the surface that was loaded in tension during the three-point-bend test is

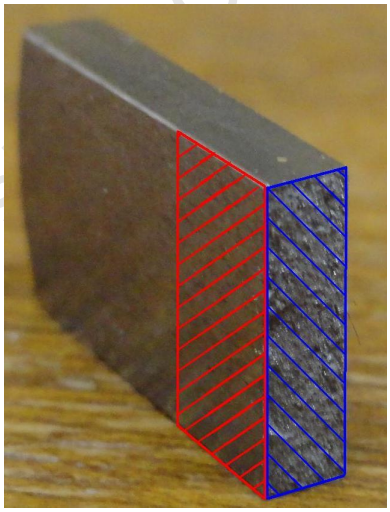

Figure 6.1 – Photograph showing the two surfaces that were prepared for light microscopy in order to investigate the fracture of the three-point-bend specimens. The surface shown by red cross-hatching is the surface of the specimen that was loaded in tension during the three-point-bending and the surface shown in blue cross-hatching is the fracture surface.

shown by red cross-hatching and the fracture surface is shown by blue cross-hatching. In the case of the fracture surface, the specimen was mounted and ground using only 1200 grit SiC grinding paper and was observed every 20 seconds of grinding until a planar surface was achieved and the rough characteristics of the fracture surface had been removed. This was done in an attempt to remove as little material as was possible to ensure that the prepared surface was as near to the fracture surface as possible. When preparing the tensile surface for light microscopy, the surface was ground for only 30 seconds using 1200

grit SiC grinding paper. Following this grinding, regular polishing as per the recipe shown in table 3.1 on page 57 resumed.

Light microscopy of the tensile surface was conducted on the specimens A-S(1), PSC800(3) and PSC1000(2) and the fracture surface of the specimens A-S(3) and PSC1000(1) was analysed. The results from the tensile surface are given here followed by the results from the fracture surfaces.

6.1 Light Microscopy of Tensile Surfaces

Light micrographs of the tensile surface in the vicinity of the fracture point of the three-point-bend specimens A-S(1), PSC800(3) and PSC1000(2) are given in figure 6.2. In each

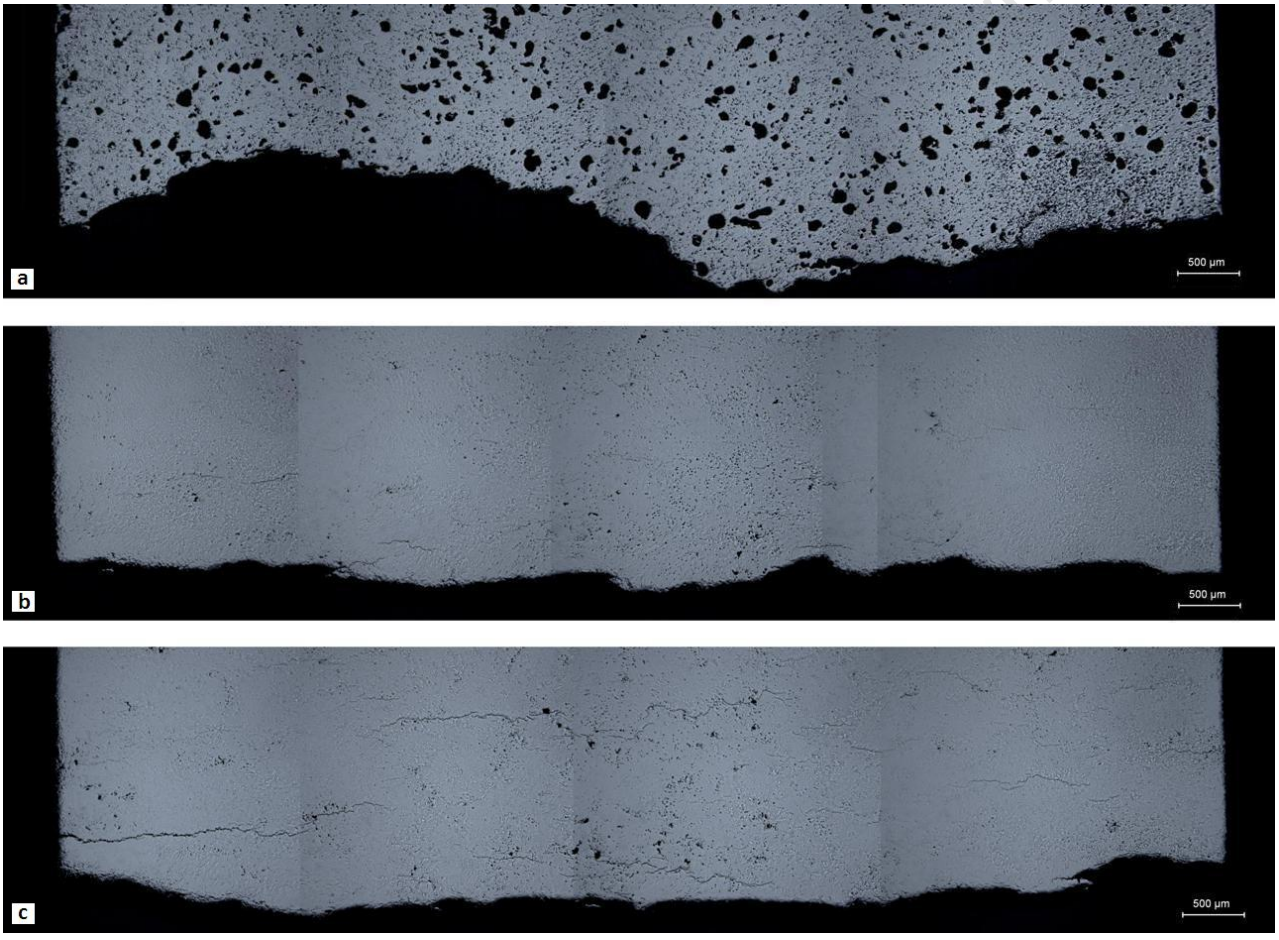

Figure 6.2 – Light micrographs of the tensile surfaces of the three-point-bend specimens: a) A-S(1) ; b) PSC800(3) ; c) PSC1000(2). The fracture surface is evident as a jagged edge at the bottom of each of the micrographs.

case the fracture surface is seen as a jagged edge at the bottom of each of the individual micrographs. Higher magnification light micrographs showing some of the cracks that were evident near to the fracture surface on this tensile surface for the specimens A-S(1), PSC800(3) and PSC1000(2) are given in figures 6.3 on the next page, 6.4 on the facing page and 6.5 on page 112 respectively.

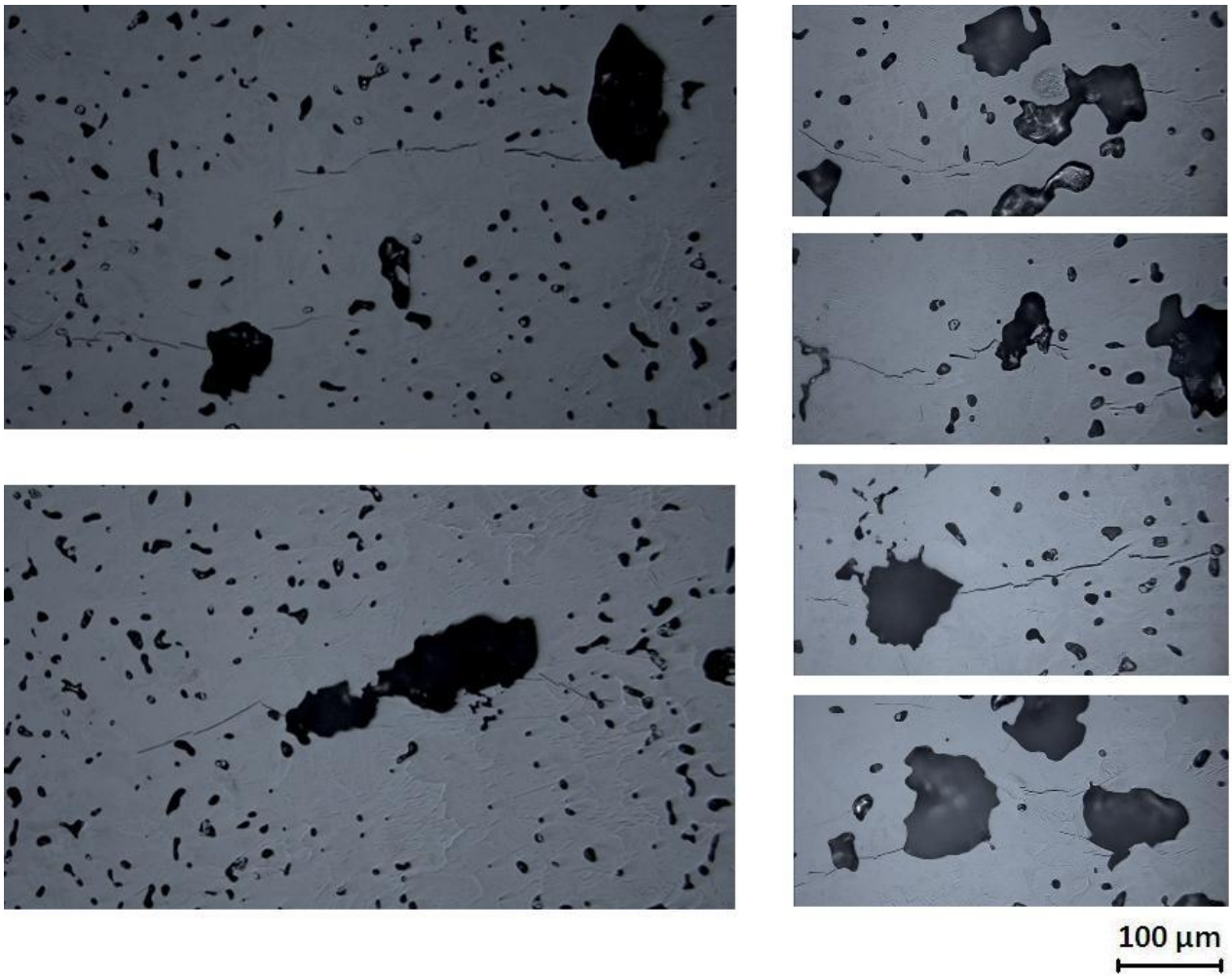

Figure 6.3 – Light micrographs showing some of the cracks evident on the tensile surface of the A-S(1) three-point-bend specimen near to the fracture surface.

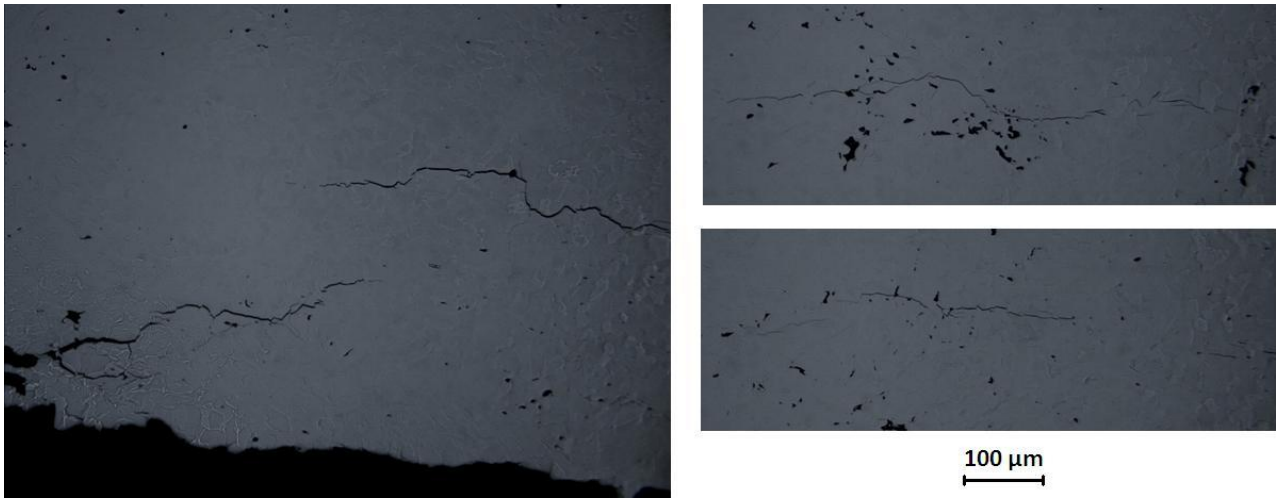

Figure 6.4 – Light micrographs showing some of the cracks evident on the tensile surface of the PSC800(3) three-point-bend specimen near to the fracture surface.

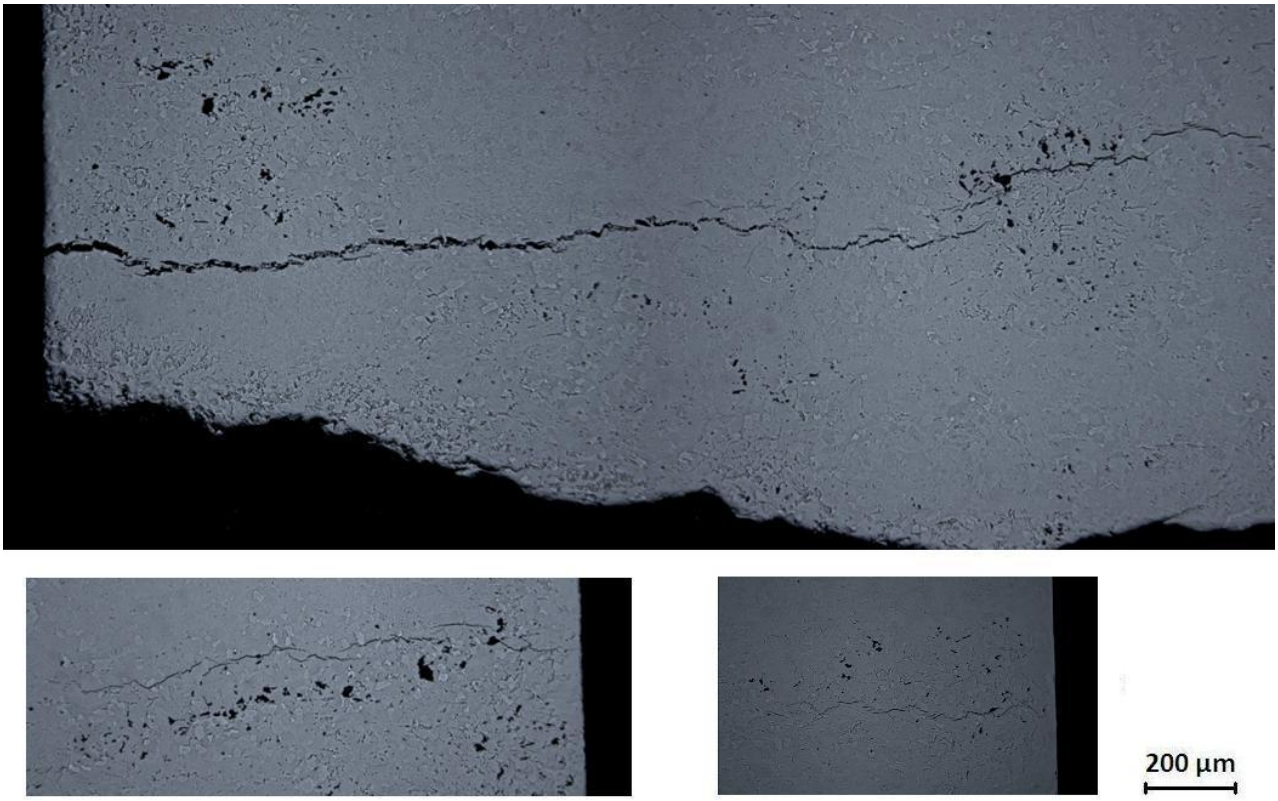

Figure 6.5 – Light micrographs showing some of the cracks evident on the tensile surface of the PSC1000(2) three-point-bend specimen near to the fracture surface.

6.2 Light Microscopy of Sections Parallel to Fracture Surfaces

Light micrographs were taken through the thickness of the three-point-specimens A-S(3) and PSC1000(1) in a plane as near to the fracture surface as it was possible to prepare a microscopy surface. A selection of micrographs showing some of the cracks evident in this plane are shown in figure 6.6 on the facing page for specimen A-S(3) and in figure 6.7 on page 114 for specimen PSC1000(1). In each of the micrographs an edge is seen; this edge is the tensile surface of the three-point-bend specimens which is where the cracking was evident.

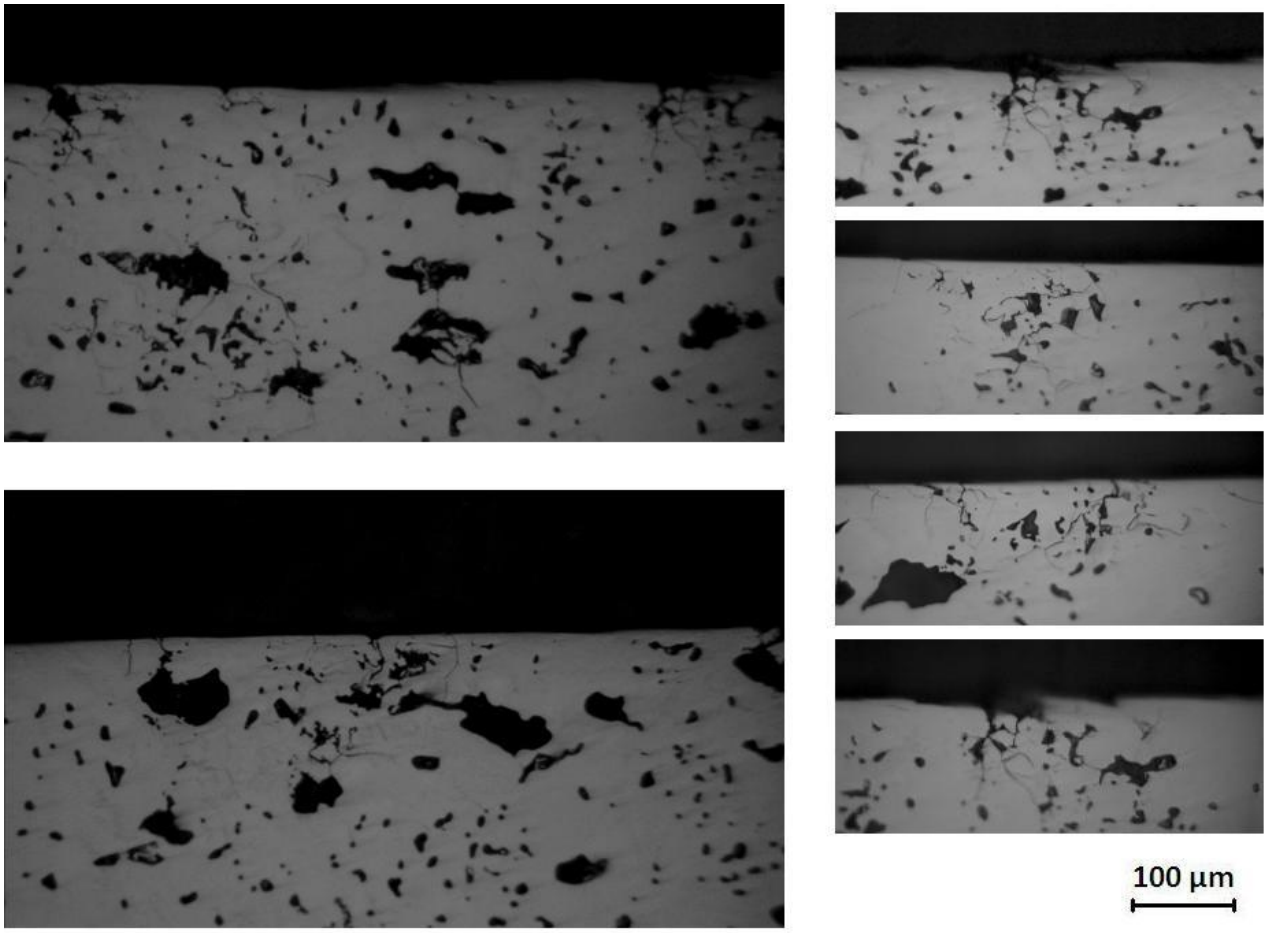

Figure 6.6 – Light micrographs showing cracking in the three-point-bend specimen A-S(3) in a through thickness plane near to the fracture surface. The edge visible in the micrographs is the edge that was loaded in tension during the testing which is where the cracking was concentrated.

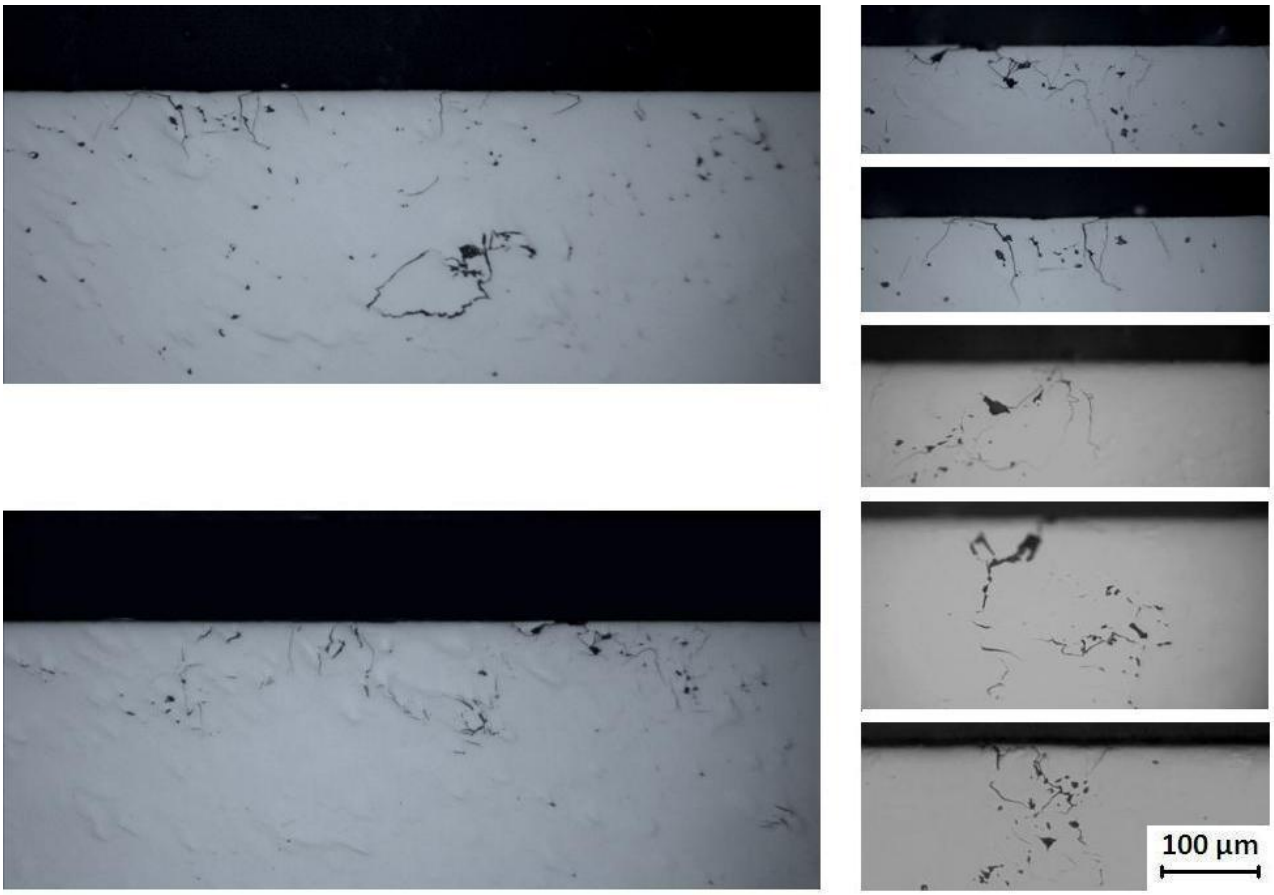

Figure 6.7 – Light micrographs showing cracking in the three-point-bend specimen PSC1000(1) in a through thickness plane near to the fracture surface. The edge visible in the micrographs is the edge that was loaded in tension during the testing which is where the cracking was concentrated.

6.3 Discussion of Light Microscopy of Fractured Three-Point-Bend Specimens

The light micrographs of the tensile surfaces of the A-S(1), PSC800(3) and PSC1000(2) specimens in figure 6.2 on page 110 reveal obvious cracks near the fracture surface of the specimen deformed at 1000 ° C - PSC1000(2). Cracks are also evident in the specimen deformed at 800 ° C - PSC800(3) - although to a lesser degree. Large cracks are not as easily seen in figure 6.2 for the specimen in the as-sintered condition - A-S(1) - as was the case for the TMP specimens. When viewed at a higher magnification however, cracking near to the fracture surface of the as-sintered specimen was evident and such cracks as are shown in figure 6.3 on page 111 were revealed. These cracks are seen always to include the very large pores existing in the microstructure of around 100 µm. It could be argued that these large pores are arresting the cracks rather than initiating them, but the observation that there are no cracks present that do not include these large pores suggest rather that these pores play some role in the initiation of these cracks.

When looking at the fractured as-sintered specimen - A-S(3) - in a plane parallel and very

near to the fracture surface (figure 6.6 on page 113) the cracks near to the tensile surface of the specimen are seen to coincide with the large pores. In some situations these cracks are seen not to be connected to the tensile surface but rather exist at a large pore just beneath the tensile surface.

In the microstructure of the BE specimens having undergone TMP, the large ($\approx 100\mu m$) pores are no longer evident. These pores must therefore have collapsed when the material was deformed. To what extent these collapsed pores exist as separate surfaces collapsed upon one another, creating the equivalent of a crack, or whether in fact these collapsed pores "heal" by means of the two surfaces collapsed together coalescing by way of diffusion is unknown. In the case of the former, this could be a possible explanation as to why the TMP material is seen to be weaker than the as-sintered material, as it would essentially have present within it already formed cracks which would propagate readily upon loading. Bearing in mind that the effect of any pores, cracks and stress concentrations existing within the BE material created for this research will be particularly detrimental to it's mechanical performance due to it's brittle nature.

The microscopy conducted on the tensile surface (figures 6.4 on page 111 and 6.5 on page 112) and on a through thickness plane near to the fracture surface (figure 6.7 on the preceding page) show that the cracks evident exist through or very nearby to small areas of high porosity density. It is possible that these areas represent the collapsed large pores that existed in the as-sintered material, but it cannot be determined for certain, and they may simply be pores that were not closed during the deformation. Whatever the origin of these pores, it is clear that cracks initiate preferentially near to these high-porosity areas. In the micrographs of cracks in the through-thickness plane of the PSC1000(1) specimen (figure 6.7 on the facing page), cracking is seen to exist beneath the tensile surface where some of these pores are present. This suggests that these pores play a role in initiating cracks, as the cracks are present at these pores beneath the surface and therefore have not grown from the surface which represents the highest stressed material.

Chapter 7

Conclusions

Based on the research conducted and presented in this dissertation, the following conclusions were drawn:

- The blending of separate Al and V elemental powders with direct reduction titanium powder followed by pressing this powder into a green compact at a pressure of 375MPa and sintering at a temperature of 1200 $^\circ$C for 2 hours created a material that was brittle and exhibited no plastic deformation prior to sudden fracture when subjected to three-point-bending. This brittle behaviour is thought to be as a result of using elemental powders as opposed to an Al-V master alloy, since creating BE Ti-6Al-4V using a master alloy powder with similar direct reduction titanium powder as used in this research has been shown by other researchers to produce material with significant plastic ductility.

- A combination of light microscopy, EBSD analysis and SEM imaging was successfully used to distinguish between the diffusional and martensitic transformation products when the Ti-5Al-4V alloy was cooled from temperatures high in the α+β region and β single phase regions.

- The BE material used in this research transformed from temperatures high in the α+β region and β single phase regions by diffusional nucleation and growth mechanisms at cooling rates (in excess of 100 $^\circ$C/s) that had been reported to suppress diffusional mechanisms and result in a martensitic transformation. This is thought to be as a result of the high oxygen content of BE material increasing the transformational kinetics of the material.

- Deformation to a compressive true strain of 0.69 and subsequent annealing resulted in recrystallisation creating a refined equiaxed microstructure when deformation was conducted at temperatures between 600 $^\circ$C and 900 $^\circ$C. At deformation temperatures of 1000 $^\circ$C and 1100 $^\circ$C, insufficient strain energy was retained within the material and no recrystallisation occurred during the annealing treatment and

instead a bi-modal (1000 ˚C) and fully lamellae (1100 ˚C) was achieved for these deformation temperatures.

- The TMP of porous PM Ti-6Al-4V can significantly increase the relative density of the material. This research has shown deformations to a true strain of 0.69 to result in a relative density increase from 88% to in excess of 98%.
- The increased density resulting from the TMP of porous PM Ti-6Al-4V is insensitive of the temperature at which the deformation is conducted within the temperature range tested of between 600 ˚C and 1100 ˚C.
- The TMP of the porous and brittle Ti-6Al-4V created by BE PM for this research, despite profoundly increasing the relative density, has a detrimental affect on the mechanical properties of the resulting TMP material.

Chapter 8

Future Work and Recommendations

As a result of the current research and findings, the author suggests the following:

- Any further research conducted on BE Ti-6Al-4V should be produced using an Al-V master alloy powder rather than separate elemental powders. It is thought that this will both improve the compositional control and the ductility of the resulting BE material.
- Any further research conducted on BE Ti-6Al-4V should be preceded by a study of BE practices and parameters as those practices and parameters used in this research have resulted in lower density and larger porosity (as large as 100 μm) than other researchers have achieved. It is probable that the use of an Al-V master alloy will influence these characteristics and therefore creating a sintered product from BE powder using a master alloy and the same press and sinter process used in this research would be a good starting point, after which compacting pressures to form the green compact and sintering temperature are two important parameters to be explored.
- A simpler approach to studying the possible strength benefits of the TMP of porous sintered preforms could be to repeat similar work as was done in this research using CP Ti direct reduction powder.

Bibliography

[1] M.J. Donachie. *Titanium: a technical guide*. Asm Intl, 2000.

[2] V.A.R. Henriques, P.P. Campos, C.A.A. Cairo, and J.C. Bressiani. Production of titanium alloys for advanced aerospace systems by powder metallurgy. *Materials Research*, 8(4):443–446, 2005.

[3] FH Froes, SJ Mashl, JC Hebeisen, VS Moxson, and VA Duz. The technologies of titanium powder metallurgy. *JOM Journal of the Minerals, Metals and Materials Society*, 56(11):46–48, 2004.

[4] C. Leyens and M. Peters. *Titanium and titanium alloys*. Wiley Online Library, 2003.

[5] G. Lutjering, JC Williams, and A. Gysler. Microstructure and mechanical properties of titanium alloys. *Microstructure and Properties of Materials*, 2:1–74, 2000.

[6] M. Donachie. *Titanium: A technical guide*. ASM International, 1988.

[7] VAR Henriques, HRZ Sandim, GC Coelho, and CRM da Silva. Microstructural evolution during hot pressing of the blended elemental ti-6 *Materials Science and Engineering: A*, 347(1):315–324, 2003.

[8] V. Moxson, O.N. Senkov, and FH Froes. Innovations in titanium powder processing. *JOM Journal of the Minerals, Metals and Materials Society*, 52(5):24–26, 2000.

[9] G. Lütjering and J.C. Williams. *Titanium*. Springer Verlag, 2007.

[10] S. Malinov, Z. Guo, W. Sha, and A. Wilson. Differential scanning calorimetry study and computer modeling of beta -> alpha phase transformation in a ti-6al-4v alloy. *Metallurgical and Materials Transactions A*, 32(4):879–887, 2001.

[11] S. Banerjee and P. Mukhopadhyay. *Phase transformations: examples from titanium and zirconium alloys*. Elsevier Science, 2007.

[12] JW Elmer, TA Palmer, SS Babu, and ED Specht. In situ observations of lattice expansion and transformation rates of α and β phases in ti–6al–4v. *Materials Science and Engineering: A*, 391(1):104–113, 2005.

[13] Shawn Michael Kelly. *Thermal and Microstructure Modeling of Metal Deposition Processes with Application to Ti-6Al-4V*. PhD thesis, Virginia Polytechnic Institute and State University, 2004.

[14] S. Malinov, W. Sha, Z. Guo, CC Tang, and AE Long. Synchrotron x-ray diffraction study of the phase transformations in titanium alloys. *Materials characterization*, 48(4):279–295, 2002.

[15] T. Ahmed and HJ Rack. Phase transformations during cooling in (alpha + beta) titanium alloys. *Materials Science and Engineering: A*, 243(1):206–211, 1998.

[16] S. Malinov, W. Sha, and Z. Guo. Application of artificial neural network for prediction of time-temperature-transformation diagrams in titanium alloys. *Materials Science and Engineering: A*, 283(1):1–10, 2000.

[17] DJ DeLazaro and W. Rostoker. The influence of oxygen contents on transformations in a titanium alloy containing 11 per cent molybdenum. *Acta Metallurgica*, 1(6):674–678, 1953.

[18] I.S. Polkin and I.I. Novikov. *Uprocniaustaia Termicheskaia Obrabotka Titanovih Splavov*. Metallurgia, 1984.

[19] YT Lee and G. Welsch. Young's modulus and damping of ti—6al—4v alloy as a function of heat treatment and oxygen concentration. *Materials Science and Engineering: A*, 128(1):77–89, 1990.

[20] A.M. Russell and K.L. Lee. *Structure-property relations in nonferrous metals*. Wiley Online Library, 2005.

[21] L. Zeng and TR Bieler. Effects of working, heat treatment, and aging on microstructural evolution and crystallographic texture of a, a' and a" phases in ti-6al-4v wire. *Materials Science and Engineering: A*, 392(1):403–414, 2005.

[22] G. Lütjering. Influence of processing on microstructure and mechanical properties of (alpha + beta) titanium alloys. *Materials Science and Engineering: A*, 243(1):32–45, 1998.

[23] M. Peters, G. ZIEGLER, and G. LUETJERING. Control of microstructures of (alpha+ beta)-titanium alloys. *Zeitschrift für Metallkunde*, 74:274–282, 1983.

[24] JP Immarigeon, RT Holt, AK Koul, L. Zhao, W. Wallace, and JC Beddoes. Lightweight materials for aircraft applications. *Materials characterization*, 35(1):41–67, 1995.

[25] G. Lütjering. Property optimization through microstructural control in titanium and aluminum alloys. *Materials Science and Engineering A*, 263(2):117–126, 1999.

[26] A. Dehghan-Manshadi, MH Reid, and RJ Dippenaar. Effect of microstructural morphology on the mechanical properties of titanium alloys. In *Journal of Physics: Conference Series*, volume 240, page 012022. IOP Publishing, 2010.

[27] H. Fujii. Strengthening of (alpha + beta) titanium alloys by thermomechanical processing. *Materials Science and Engineering: A*, 243(1):103–108, 1998.

[28] V. Upadhyay. *Manufacturing Processes (3rd Edition)*. S. K. Kataria & Sons, 2010.

[29] G. Greetham. Powder metallurgy - component manufacture by uniaxial pressing.

[30] F. Thümmler and R. Oberacker. *An introduction to powder metallurgy*. Institute of Materials series on powder metallurgy. Institute of Materials, 1993.

[31] R. German. *Powder Metallurgy Science second edition*. Princeton, 1994.

[32] DP Delo and HR Piehler. Early stage consolidation mechanisms during hot isostatic pressing of ti-6al-4v powder compacts. *Acta materialia*, 47(9):2841–2852, 1999.

[33] FH Froes and D. Eylon. Developments in titanium p/m. Institute for Materials & Advanced Processes (IMAP) University of Idaho, 2005.

[34] D.F. Heaney and R.M. German. Advances in the sintering of titanium powders. In *PM Lightweight and Porous Materials*, 2004.

[35] T. Fujita, A. Ogawa, C. Ouchi, and H. Tajima. Microstructure and properties of titanium alloy produced in the newly developed blended elemental powder metallurgy process. *Materials Science and Engineering: A*, 213(1):148–153, 1996.

[36] V.S. Moxson Duz, V.A. and O.M. Ivasishin. Recent developments in titanium powder metallurgy. In *2007 World Titanium Conference*, 2007.

[37] V. S. Moxson. Low cost components for armor and structural applications. In *International Titanium Conference*, 2005.

[38] JE Smugeresky and DB Dawson. New titanium alloys for blended elemental powder processing. *Powder Technology*, 30(1):87–94, 1981.

[39] G. Welsch, YT Lee, PC Eloff, D. Eylon, and FH Froes. Deformation behavior of blended elemental ti-6al-4v compacts. *Metallurgical and Materials Transactions A*, 14(3):761–769, 1983.

[40] I. Weiss, D. Eylon, MW Toaz, and FH Froes. Effect of isothermal forging on microstructure and fatigue behavior of blended elemental ti-6al-4v powder compacts. *Metallurgical and Materials Transactions A*, 17(3):549–559, 1986.

[41] J. R. Davis, editor. *Metals Handbook Ninth Edition: Volume 8 Mechanical Testing*. ASM, 1985.

[42] DSI. Gleeble systems application note. 2011.

[43] A. Duckham and RD Knutsen. Asymmetric flow during plane strain compression testing of aluminum alloys. *Materials Science and Engineering: A*, 256(1):220–226, 1998.

[44] J. Kliber, S. Aksenov, and R. Fabík. Numerical study of deformation characteristics in plane strain compression test(psct) volume certified following microstructure. *Metalurgija/Metallurgy*, 48(4):257–261, 2009.

[45] A.D. Rietman. *Numerical Analysis of Inhomogeneous deformation in plane strain compression*. Universiteit Twente, 1999.

[46] J.H. Beynon and C.M. Sellars. Strain distribution patterns during plane strain compression. *Journal of testing and evaluation*, 13(1):28–38, 1985.

[47] F.J. Humphreys and M. Hatherly. *Recrystallization and related annealing phenomena*. Elsevier Science Ltd, 1995.

[48] M.J. Dollman. The inlfuence of microstructure on the creep properties of 441 ferretic stainless steel. Master's thesis, University of Cape Town, 2003.

[49] T. Furuhara, B. Poorganji, H. Abe, and T. Maki. Dynamic recovery and recrystallization in titanium alloys by hot deformation. *JOM Journal of the Minerals, Metals and Materials Society*, 59(1):64–67, 2007.

[50] T. Seshacharyulu, SC Medeiros, WG Frazier, and Y. Prasad. Hot working of commercial ti-6al-4v with an equiaxed (alpha + beta) microstructure: materials modeling considerations. *Materials Science and Engineering: A*, 284(1):184–194, 2000.

[51] R. Ding, ZX Guo, and A. Wilson. Microstructural evolution of a ti-6al-4v alloy during thermomechanical processing. *Materials Science and Engineering: A*, 327(2):233–245, 2002.

[52] A. Momeni and SM Abbasi. Effect of hot working on flow behavior of ti-6al-4v alloy in single phase and two phase regions. *Materials & Design*, 31(8):3599–3604, 2010.

[53] N.K. Park, J.T. Yeom, and Y.S. Na. Characterization of deformation stability in hot forging of conventional ti-6al-4v using processing maps. *Journal of materials processing technology*, 130:540–545, 2002.

[54] C.H. Park, K.T. Park, D.H. Shin, and C.S. Lee. Microstructural mechanisms during dynamic globularization of ti-6al-4v alloy. *Materials transactions*, 49(10):2196, 2008.

[55] T. Seshacharyulu, SC Medeiros, WG Frazier, and Y. Prasad. Microstructural mechanisms during hot working of commercial grade ti-6al-4v with lamellar starting structure. *Materials Science and Engineering: A*, 325(1):112–125, 2002.

[56] S. Bruschi, S. Poggio, F. Quadrini, and ME Tata. Workability of ti-6al-4v alloy at high temperatures and strain rates. *Materials Letters*, 58(27):3622–3629, 2004.

[57] A. Majorell, S. Srivatsa, and RC Picu. Mechanical behavior of ti-6al-4v at high and moderate temperatures - part i: Experimental results. *Materials Science and Engineering: A*, 326(2):297–305, 2002.

[58] S. Nemat-Nasser, W.G. Guo, V.F. Nesterenko, SS Indrakanti, and Y.B. Gu. Dynamic response of conventional and hot isostatically pressed ti-6al-4v alloys: experiments and modeling. *Mechanics of Materials*, 33(8):425–439, 2001.

[59] Y. Prasad, T. Seshacharyulu, SC Medeiros, and WG Frazier. Influence of oxygen content on the forging response of equiaxed (α+ β) preform of ti–6al–4v: commercial vs. eli grade. *Journal of Materials Processing Technology*, 108(3):320–327, 2001.

[60] A.S. Khan, R. Kazmi, B. Farrokh, and M. Zupan. Effect of oxygen content and microstructure on the thermo-mechanical response of three ti–6al–4v alloys: Experiments and modeling over a wide range of strain-rates and temperatures. *International journal of plasticity*, 23(7):1105–1125, 2007.

[61] D.G. Lee, S. Kim, S. Lee, and C. Soo Lee. Effects of microstructural morphology on quasi-static and dynamic deformation behavior of ti-6al-4v alloy. *Metallurgical and Materials Transactions A*, 32(2):315–324, 2001.

[62] MG Da Silva and KT Ramesh. The rate-dependent deformation and localization of fully dense and porous ti-6al-4v. *Materials Science and Engineering: A*, 232(1):11–22, 1997.

[63] T. Seshacharyulu, SC Medeiros, JT Morgan, JC Malas, WG Frazier, and Y. Prasad. Hot deformation mechanism in eli grade ti-6al-4v. *Scripta materialia*, 41(3):283–288, 1999.

[64] A.A. Salem, SR Kalidindi, RD Doherty, and SL Semiatin. Strain hardening due to deformation twinning in alpha-titanium: Mechanisms. *Metallurgical and Materials Transactions A*, 37(1):259–268, 2006.

[65] Y. Zhong, F. Yin, and K. Nagai. Role of deformation twin on texture evolution in cold-rolled commercial-purity ti. *Journal of Materials Research*, 23(11):2954–2966, 2008.

[66] YB Chun, SH Yu, SL Semiatin, and SK Hwang. Effect of deformation twinning on microstructure and texture evolution during cold rolling of cp-titanium. *Materials Science and Engineering: A*, 398(1):209–219, 2005.

[67] J.W. Christian and S. Mahajan. Deformation twinning. *Progress in Materials Science*, 39(1-2):1–157, 1995.

[68] H. Conrad. Effect of interstitial solutes on the strength and ductility of titanium. *Progress in Materials Science*, 26(2):123–403, 1981.

[69] N.E. Paton and WA Backofen. Plastic deformation of titanium at elevated temperatures. *Metallurgical and Materials Transactions B*, 1(10):2839–2847, 1970.

[70] S. Zaefferer. A study of active deformation systems in titanium alloys: dependence on alloy composition and correlation with deformation texture. *Materials Science and Engineering: A*, 344(1):20–30, 2003.

[71] JC Williams, RG Baggerly, and NE Paton. Deformation behavior of hcp ti-al alloy single crystals. *Metallurgical and Materials Transactions A*, 33(13):837–850, 2002.

[72] DG Prakash, R. Ding, RJ Moat, I. Jones, PJ Withers, J. Fonseca, and M. Preuss. Deformation twinning in ti-6al-4v during low strain rate deformation to moderate strains at room temperature. *Materials Science and Engineering: A*, 527(21):5734–5744, 2010.

[73] F. Coghe, W. Tirry, L. Rabet, D. Schryvers, and P. Van Houtte. Importance of twinning in static and dynamic compression of a ti-6al-4v titanium alloy with an equiaxed microstructure. *Materials Science and Engineering: A*, 537:1–10, 2012.

[74] G.G. Yapici, I. Karaman, and Z.P. Luo. Mechanical twinning and texture evolution in severely deformed ti-6al-4v at high temperatures. *Acta materialia*, 54(14):3755–3771, 2006.

[75] KT Kim and HC Yang. Densification behavior of titanium alloy powder during hot pressing. *Materials Science and Engineering: A*, 313(1):46–52, 2001.

[76] KT Kim, HC Yang, and ST Hong. Densification behaviour of titanium alloy powder compacts at high temperature. *Powder metallurgy*, 44(1):34–40, 2001.

[77] YT Lee, M. Peters, and G. Wirth. Effects of thermomechanical treatment on microstructure and mechanical properties of blended elemental ti-6al-4v compacts. *Materials Science and Engineering: A*, 102(1):105–114, 1988.

[78] Standard test methods for metal powders and powder metallurgy products 2010 edition.

[79] R. Filip, K. Kubiak, W. Ziaja, and J. Sieniawski. The effect of microstructure on the mechanical properties of two-phase titanium alloys. *Journal of Materials Processing Technology*, 133(1):84–89, 2003.

Appendix

The MPIF standards used during this research are given here in the appendix. Standard 41 for measuring the transverse rupture strength of PM products is presented first followed by standard 54 for determining the density of impermeable PM material.

METAL POWDER INDUSTRIES FEDERATION

Method for

Determination of Transverse Rupture Strength of Powder Metallurgy (PM) Materials

MPIF Standard 41
Issued 1951, Revised 1962, 1973, 1991, 1998, 2000, 2008
(Formerly included in Standard 13)

STANDARD 41

1. SCOPE

1.1 This standard covers the apparatus, test specimen and procedures for determining the bending strength or transverse rupture strength of powder metallurgy materials.

1.2 The test as described and specified herein is applicable only to materials of negligible ductility. If applied to materials showing noticeable plastic deformation (exceeds 0.02 inch [0.5 mm] permanent deflection, the maximum load may not be equal to the break load, which could lead to misinterpretation of results. For such materials the tensile strength test should be used.

1.3 *This standard may involve hazardous materials, operations and equipment. This standard does not purport to address all of the potential safety problems associated with its use. It is the responsibility of the user of this standard to establish appropriate safety and health practices and to determine the applicability of regulatory limitations prior to use.*

2. APPARATUS

2.1 Gauges capable of measuring from 0 to 1.000 inch (0 to 25 mm) to the nearest 0.001 inch (0.025 mm).

2.2 A transverse strength fixture as shown in Figure 2.

2.3 A universal testing maching readable to within 0.1% of full scale reading. Use the lowest testing range that can provide a measurable result.

NOTE 1—Names of manufacturers of this apparatus are listed in General Information IV.

3. TEST SPECIMEN

3.1 The specimens may be pressed in the die shown in Fig. 1 and shall be free from visible laminations and other flaws.

3.2 The die may be prepared as a solid die with dimensions as shown in Fig. 1. The uniformity of the "green" specimens ejected from the die may be determined by measuring the thickness with a gauge and by weighing. The mass of any specimen in a given lot shall not vary more than ± 1.5 % from the mean.

3.3 The test specimen shall have the configuration as shown in Fig. 3. Parallelism shall not exceed 0.003 inch (0.076 mm).

4. PROCEDURE

4.1 The specimen shall be prepared in accordance with MPIF Standard 60.

4.2 Transverse rupture strength

4.2.1 Measure the width and thickness of the specimen to the nearest 0.001 inch (0.025 mm). After measuring, break the specimens in the testing fixture as shown in Fig. 2. In this fixture the specimen is supported by, and perpendicular to, two hardened steel (or carbide) rods 0.125 inch (3.10 mm) in diameter whose centers are 1.000 inch (25.40 mm) apart. Another hardened steel (or carbide) rod 0.125 inch (3.1 mm) in diameter presses upon the upper face of the test piece, central to the span. Test the specimen in the fixture in a universal testing maching. Apply the load at the rate of not more than 0.2 inch per minute (5 mm/min) travel of the bed of the testing machine, and note the load at which the specimen breaks.

5. CALCULATIONS

5.1 Calculate the transverse rupture strength as follows:

$$TRS = \frac{3\,P\,L}{2\,t^2 w}$$

where:

TRS = transverse rupture strength in 10^3 psi or MPa
P = break load lbf (N) (as determined)
L = the distance between the supporting rods 1.000 inch (25.40 mm)
t = the thickness of the piece in inches (mm)
w = the width of the piece in inches (mm)

6. REPORT

6.1 Report the transverse rupture strength as the average of a minimum of 3 tests to the nearest 10^3 psi or 10 MPa.

6.2 The following supplementary information may also be reported for clarification:
6.2.1 Identification of powder, brand, grade, lot number.
6.2.2 Chemical composition of powder mix used if other than elemental powders being tested.
6.2.3 Type, brand and percent of lubricant.
6.2.4 Density, green and sintered.
6.2.5 Sintering temperature.
6.2.6 Sintering time.
6.2.7 Furnace atmosphere.
6.2.8 Final total carbon content where applicable.
6.2.9 Other processing information as required.

7. PRECISION

7.1 The repeatability (r) and reproducibility (R) measurements were determined (1995) according to ASTM E 691, Practice for Conducting an Interlaboratory Test Program to Determine the Precision of Test Methods and are listed below for six materials and a range of transverse rupture strength values. On the basis of test error alone, the difference in absolute value of two test results obtained in the same laboratory will be expected to exceed (r) only 5% of the time. If such a difference is found to be larger than (r), there is reason to question one or both results. Similarly, the difference in two test results obtained in different laboratories will be expected to exceed (R) only 5% of the time. If the difference is found to be larger than (R), there is reason to question one or both measurements.

APPENDIX

A1. COMPARABLE STANDARDS.
ASTM B 528
ISO 3325

Table 1. Precision of Transverse Rupture Strength

MATERIAL	DENSITY g/cm³	APPARENT HARDNESS	TRS psi	# LABS	(r) psi	(R) psi
F-0005-15	6.22	37 HRB	63,000	19	4,800	7,900
FC-0205-30	6.21	43 HRB	66,500	16	5,600	11,500
F-0005-25	6.91	40 HRB	71,000	12	5,500	14,000
FN-0208-35	6.95	77 HRB	123,500	19	6,900	11,600
FL-4405-40	7.04	75 HRB	129,500	16	7,000	13,800
FC-0208-50	6.69	81 HRB	144,000	12	12,500	21,000
FC-0208-65HT	6.43	31 HRC	138,500	22	15,400	28,000
F-0008-65HT	6.68	35 HRC	148,500	16	22,000	31,700
FLC-4608-70HT	6.69	31 HRC	174,000	14	28,800	41,500
FN-0205-105HT	6.93	31 HRC	191,500	14	23,700	40,500
FC-0205-90HT	7.03	41 HRC	236,000	16	28,100	42,400
FLN-4205-140HT	7.12	41 HRC	251,500	22	32,700	46,900
FLN2-4405-160HT	7.04	38 HRC	246,000	35	21,500	31,200

The (r) and (R) values were determined from the testing of three (3) transverse rupture test specimens by each participating laboratory.

The metric system conversion factors used in this standard are in accordance with IEEE/ASTM SI 10; "Standard for Use of the International System of Units (SI): The Modern Metric System". Recognized as an American National Standard (ANSI), the standard is published by the following organizations: ASTM International, 100 Barr Harbor Drive, West Conshohocken, PA 19428-2959, USA; and Institute of Electrical and Electronics Engineers, Inc., 345 East 47th Street, New York, NY 10017, USA.

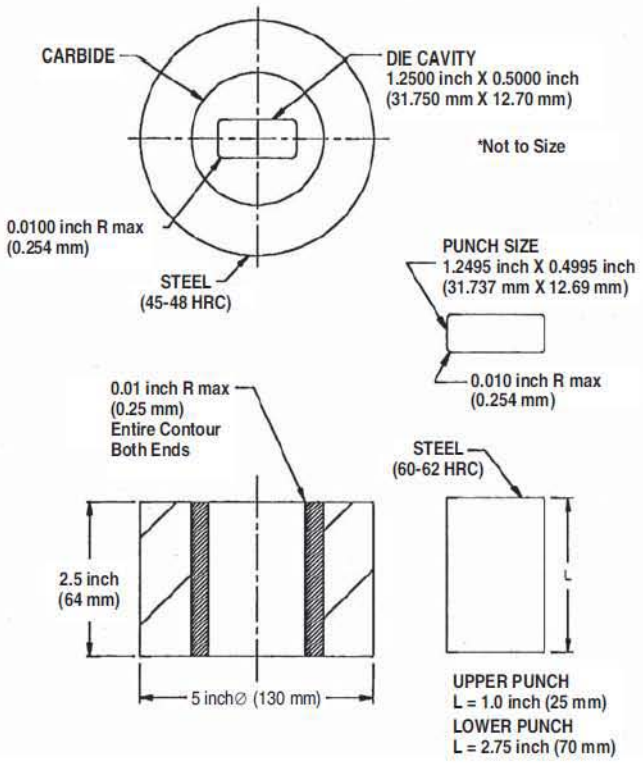

FIGURE 1: Example of Tooling to Produce a Rectangular Test Specimen.

Note: The dimensions for the cavity shall be 0.500 ± 0.004 inch wide (12.70 ± 0.10 mm) by 1.250 ± 0.004 inch long (31.75 ± 0.10 mm). The mating parts should be fitted and lapped to a 4 micro inch (N3) finish or better, to dimensions of 0.0005 inch (0.0130 mm) to 0.0010 inch (0.0250 mm) smaller than the die cavity in each dimension. The dimensions given in the drawing typify the die cavity and punch within the stated tolerance at the normal width and length. The outer ring may be AISI H-11 hardened to 45-48 HRC. The punches may be AISI A-2 or A-7 hardened to 60-62 HRC. The die insert should be die grade tungsten carbide. The shrinkage between the carbide insert and the die case typically is 0.0015-0.0025 inches per inch (0.0380-0.0635 mm per 25 mm).

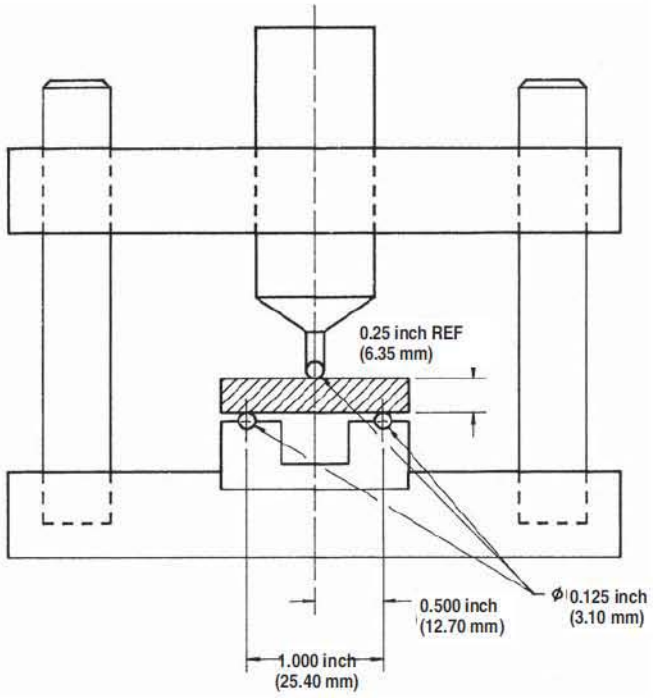

FIGURE 2: Transverse Rupture Test Fixture

Tolerance on all dimensions to be + 0.001 inch (0.0250 mm).
Hardness on 0.125 inch Ø (3.10 mm) pins to be 60 HRC minimum.

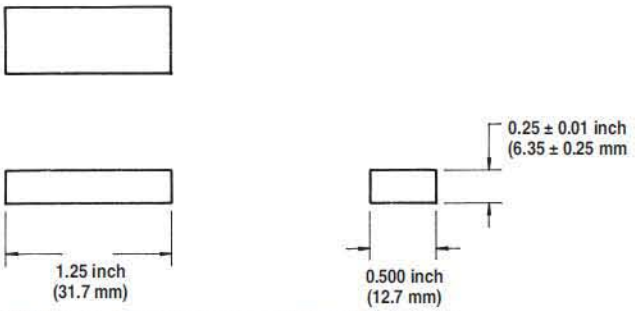

FIGURE 3: Transverse Rupture Test Specimen

METAL POWDER INDUSTRIES FEDERATION

Method for

Determination of Density of Impermeable Powder Metallurgy (PM) Materials

MPIF Standard 54
Issued 2006

STANDARD 54

1. SCOPE

1.1 This standard describes a procedure for determining the density of powder metallurgy (PM) materials and cemented carbides containing less than two percent porosity. The method is based on the principle of water displacement.

NOTE 1—A test specimen that gains mass when immersed in water indicates the specimen contains surface-connected porosity. Unsealed surface porosity will absorb water and cause density values higher than the true value. If this problem occurs, this method is not applicable and Standard 42 should be used instead.

1.2 The values stated in SI units are to be regarded as standard. Values in parentheses are for information only.

1.3 *This standard does not purport to address all of the safety problems, if any, associated with its use. It is the responsibility of the user of this standard to establish appropriate safety and health practices and determine the applicability of regulatory limitations prior to use.*

2. APPARATUS

2.1 Balance - A precision single pan balance that will permit readings within 0.01% of the test specimen mass. The balance shall be supported in a manner to eliminate mechanical vibrations and be shielded from air drafts.

2.2 Weighing Liquid - Distilled or deionized water to which 0.05 to 0.1 volume percent of a wetting agent has been added to reduce the effects of surface tension.

NOTE 2—Degassing the water by evacuation, boiling or ultrasonic agitation helps to prevent air bubbles from collecting on the test specimen and specimen support when immersed in water.

2.3 Water Container - A glass beaker or other suitable transparent container should be used to contain the water.

NOTE 3—A transparent container makes it easier to see air bubbles adhering to the test specimen and specimen support when immersed in water.

NOTE 4—For the most precise density determination, the water container should be of a size such that the level of the water does not rise more than 2.5 mm (0.10 inch) when the test specimen is lowered into the water.

2.4 Test Specimen Support for Weighing in Water - Two typical arrangements are shown in Figure 1. The suspension wire may be twisted around the test specimen or the test specimen may be supported in a wire basket that is attached to the suspension wire. For either arrangement, a single corrosion resistant wire, e.g. austenitic stainless steel, copper, or nichrome shall be used for the basket and suspension wire. The maximum recommended diameter of suspension wire to be used for various mass ranges is :

Mass, g	Wire Diameter, mm (inch)
less than 50	0.12 (0.005)
50 to less than 200	0.25 (0.010)
200 to less than 600	0.40 (0.015)
600 and greater	0.50 (0.020)

NOTE 5—For the most precise density determinations it is important that the mass and volume of all supporting wires immersed in water be minimized.

2.5 Thermometer - A thermometer with an accuracy of 0.2 °C (0.5 °F) to measure the temperature of the water.

3. TEST SPECIMEN

3.1 A complete part or a section of a part may be used for the test specimen. For the highest precision, the test specimen shall have a minimum mass of 5.0 g. If less precision can be tolerated, several test specimens may be used to reach the minimum mass, provided each test specimen has a mass of not less than 1.0 g.

NOTE 6—For metal injection molded (MIM) parts of less than 1.0 g several parts may be used to reach the minimum mass.

3.2 All test specimen surfaces shall be thoroughly cleaned of all adhering foreign materials such as dirt, grease, oil, oxide scale, metal powders or assembly materials. For cut specimens, avoid rough surfaces to which an air bubble can adhere. A 100-grit sanding or abrasive grinding is recommended to remove all rough surfaces.

4. PROCEDURE

4.1 Weigh the test specimen in air. This is mass A. This and all subsequent weighings shall be to 0.01% of the test specimen mass, for example :

Mass, g	Balance Sensitivity, g
less than 10	0.0001
10 to less than 100	0.001
100 to less than 1,000	0.01
1,000 to less than 10,000	0.1

It is important that the test specimen, balance, water and surrounding air be at a uniform temperature when the weighing is performed.

NOTE 7—For the most precise density determination, duplicate weighings should be made for all mass determinations. The balance should be adjusted to zero prior to each weighing. Duplicate mass determinations should be averaged before calculating the density.

NOTE 8—For improved reproducibility, the balance should be calibrated periodically with a standard mass that is approximately equal to the test specimen mass.

4.2 Support the container of water over the pan of the balance using a suitable bridge as shown in Figure 2a. The container of water may also be supported below the balance for weighing larger specimens if the balance has a lower beam hook for this purpose. See Figure 2b. If this arrangement is used, it is important to shield the suspension wire between the container of water and the bottom of the balance from air drafts. Ensure that the bridge does not touch the balance pan.

4.3 Suspend the test specimen support with the test specimen from the beam hook of the balance. The water should cover any wire twists and the specimen support basket by at least 6 mm (0.25 inch) to minimize the effect of surface tension forces on the weighing. Care should be taken to ensure that the test specimen and specimen support hang freely from the balance beam hook, are free of air bubbles when immersed in the water and are at the same temperature as the water and balance. Ensure that the surface of the water is free of dust particles.

4.4 Weigh the test specimen and the specimen support immersed in water. This is mass B.

4.5 Remove the test specimen. Weigh the test specimen support immersed in water at the same depth as before. This is mass C. Ensure that the suspension support is free of air bubbles and that the suspension wire is not immersed below its normal hanging depth as a change in depth will change the measured mass.

NOTE 9—Some balances are capable of being tared. This automatically removes the necessity of reweighing the specimen support every time. In this case, tare the specimen support alone, immersed in water to the same depth as with the specimen, before weighing the specimen support and specimen immersed in water. The mass of the specimen support and specimen immersed in water is mass F, which replaces mass B minus mass C.

4.6 Measure the temperature of the water to the nearest 0.5 °C (1 °F) and record its density ρ_w, at that temperature, from Table 1.

5. CALCULATION

5.1 Calculate the density as follows :

Density = D = Mass/Volume

$$= \frac{A / [A - (B - C)]}{\rho_w}$$

$$= (A\rho_w)/(A - B + C) = (A\rho_w)/(A - F)$$

where :

D = density of test specimen, g/cm^3

A = mass of test specimen in air, g

B = apparent mass of test specimen and specimen support in water, g

C = mass of specimen support immersed in water, g

F = mass of test specimen in water with mass of specimen support tared, g,

and

ρ_w = density of water, g/cm^3

6. REPORT

6.1 Report the density rounded to the nearest 0.01 g/cm^3.

7. PRECISION

The following precision data were developed using the procedures contained in ASTM B 311-86. A new interlaboratory study is planned using the procedures in a revised version of B 311. The interlaboratory study will evaluate the effect of the influence of air buoyancy on the measured density values. Calculations indicate that higher density materials such as carbides and tungsten heavy alloys may require air buoyancy to be taken into account in order to report a density value to the nearest 0.01 g/cm^3.

Material Density (g/cm^3)	Specimen Mass (g)	Repeatability (r)	Reproducibility (R)
4 to 8	< 5	0.04	0.05
	> 5 < 50	0.01	0.02
	> 200	0.02	0.03
> 14	> 5 < 50	0.06	0.07

7.2 The repeatability, r, and reproducibility, R, were determined at the 95% confidence level.

7.3 Duplicate results from the same laboratory should not

be considered suspect at the 95% confidence level unless they differ by more than r.

7.4 Test results from two different laboratories should not be considered suspect at the 95% confidence level unless they differ by more than R.

Table 1. Effect of Temperature on Water Density

Temperature	ρ_w	Temperature	ρ_w
°C	g/cm³	°F	g/cm³*
15	0.9991	60	0.9990
15.5	0.9990	61	0.9989
16	0.9989	62	0.9988
16.5	0.9988	63	0.9987
17	0.9988	64	0.9986
17.5	0.9987	65	0.9985
18	0.9986	66	0.9984
18.5	0.9985	67	0.9983
19	0.9984	68	0.9982
19.5	0.9983	69	0.9981
20	0.9982	70	0.9980
20.5	0.9981	71	0.9978
21	0.9980	72	0.9977
21.5	0.9979	73	0.9975
22	0.9978	74	0.9974
22.5	0.9976	75	0.9973
23	0.9975	76	0.9972
23.5	0.9974	77	0.9970
24	0.9973	78	0.9969
24.5	0.9972	79	0.9967
25	0.9970	80	0.9966
25.5	0.9969	81	0.9964
26	0.9968	82	0.9963
26.5	0.9966	83	0.9961
27	0.9965	84	0.9959
27.5	0.9964	85	0.9958
28	0.9962	86	0.9956
28.5	0.9961		
29	0.9959	*Interpolated from °C data	
29.5	0.9958		
30	0.9956		

The values of ρ_w shown are taken from, "Metrological Handbook 145, Quality Assurance for Measurements", 1990, NIST, pp. 9.10., and represent the values in air at one atmosphere pressure.

APPENDIX

A.1 COMPARABLE STANDARDS
ASTM B 311
ISO 3369

NOTE A1—The water density table in ISO 3369 differs from the table contained in this standard.

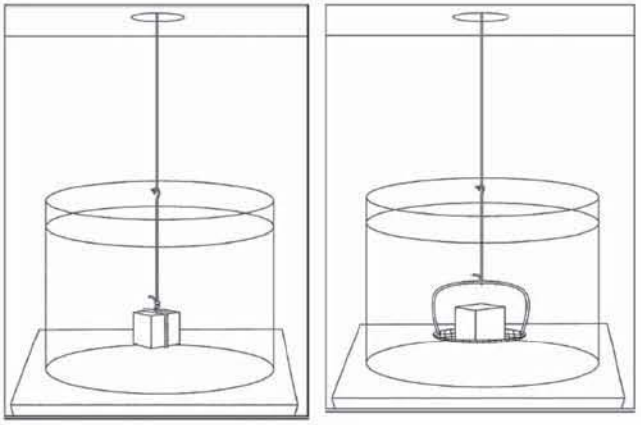

a. Twisted wire arrangement b. Basket support arrangement

FIGURE 1: Methods for Holding the Test Specimen When Weighing in Water.

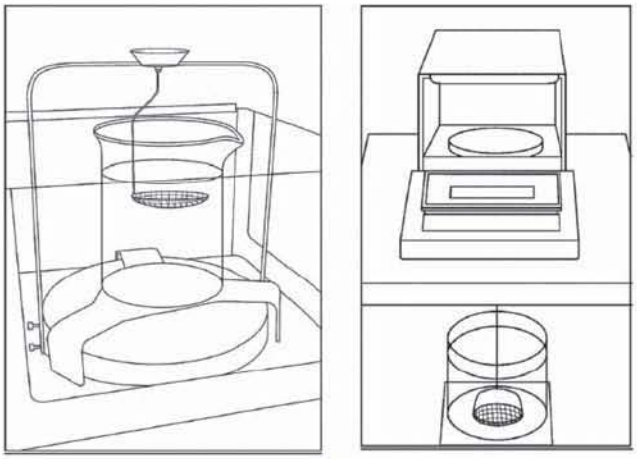

a. Beaker support above balance plan b. Weighing arrangement below the balance plan

FIGURE 2: Methods for Weighing in Water

"Figures reprinted, with permission, from *ASTM B 963 - 08 Standard Test Methods for Oil Content, Oil-Impregnation Efficiency, and Interconnected Porosity of Sintered Powder Metallurgy (PM) Products Using Archimedes' Principle*, copyright ASTM International, 100 Barr Harbor Drive, West Conshohocken, PA 19428."

The metric system conversion factors used in this standard are in accordance with IEEE/ASTM SI 10; "Standard for Use of the International System of Units (SI): The Modern Metric System". Recognized as an American National Standard (ANSI), the standard is published by the following organizations: ASTM International, 100 Barr Harbor Drive, West Conshohocken, PA 19428-2959, USA; and Institute of Electrical and Electronics Engineers, Inc., 345 East 47th Street, New York, NY 10017, USA.